IMPROVEMENTS ON DIELECTRIC BARRIER DISCHARGE APPLICATIONS: PLASMA PHOTONIC CRYSTAL TUNING BY INDIVIDUALLY CONTROLLED FILAMENTS AND SURFACE DBD WATER TREATMENT

BY

MATTHEW CRAWFORD PALIWODA

DISSERTATION

Submitted in partial fulfillment of the requirements
for the degree of Doctor of Philosophy in Aerospace Engineering
in the Graduate College of the
University of Illinois Urbana-Champaign, 2022

Urbana, Illinois

Doctoral Committee:

Professor Joshua L. Rovey
Professor Deborah Levin
Associate Professor Davide Curreli
Associate Professor Minkwan Kim, University of Southampton

Abstract

Dielectric barrier discharge is a form of atmospheric plasma that has found interest for applications in a growing variety of industries. Its benefits include: no vacuum facility, atmospheric air as the working gas, low temperature, low current, and significant production of free radicals. Improving upon current methods of DBD microwave control and water treatment is the focus of this dissertation.

The microwave control portion of this work demonstrates a method for improving the tunability of plasma photonic crystals (PPC). PPCs are structures with periodic plasma elements that reflect electromagnetic waves at wavelengths on the order of twice the plasma periodicity and can be used to construct a wide variety of microwave components. A 2D PPC is formed by an organized array of DBD plasma filaments. Simulations of this structure identifies the background permittivity and column radius as key parameters for manipulating the bandgap width and frequency. A method for effectively changing the lattice constant, radius, and background permittivity is devised by individually controlling each periodic plasma column. This method expands the tunable frequency range by an order of magnitude. To physically implement this individually controlled PPC, the discharge electrodes are resistively biased to change the dielectric surface charge and reduces the plasma density along the filament. A DBD PPC is constructed from a 10x10 array of individually addressable electrode pins. A digital control circuit is constructed to accomplish this task with input from a microcontroller and simultaneously control multiple pins.

The water treatment portion of this work demonstrates a new water treatment setup that uses a DBD to produce ozone and pass the reactive molecules into water. The degrading effect of the reactive species on contaminants is measured by the deceased concentration of Methylene Blue (MB) within the water. Different discharge parameters are examined to gauge their effect on the degradation efficiency and optimize the setup. The gas-liquid surface area per liquid volume is identified as a key parameter for improving degradation efficiency as it increases the quantity of ozone to water without increasing the required power input.

Table of Contents

List of Figures

List of Tables

1 Photonic Crystal Background Material

Plasma photonic crystals (PPC) are a plasma form of photonic crystals, subwavelength periodic structures used as a reflective engineered bulk material to construct a wide range of microwave components. The tunability of both the plasma structure and plasma permittivity promise a photonic crystal that is fully tunable, creating microwave components with a wide tunable bandwidth. However, so far PPCs have primarily been tuned using a uniform plasma density in simulation and experiments. This work, for the first time, demonstrates a tuning method that changes bandgap frequencies over an order of magnitude and a physical control mechanism to implement this tuning method in a dielectric barrier discharge (DBD) plasma filament array. The tuning method uses individually controlled plasma columns as pixels to form a 2D PPC and manipulate the defining parameters: lattice constant, plasma density, background dielectric, and column radius. Individually controlled plasma columns are physically implemented by biasing the individual pin electrodes of a DBD filament array.

Tunable solid state microwave photonic crystals are limited by the incident wave power, which can damage the millimeter scale components when the electric field is large enough to form plasma discharge. The already excited plasma state of PPCs is expected to not be permanently damaged by large electric fields in high power microwave (HPM) components and be able to adapt to the additional electric fields. HPMs are used for Directed Energy Weapons (DEW) to overload the electric components of targets at a distance. The broadband tunability provided by PPCs would allow DEWs to tune to the susceptible frequency of a target, concentrating the microwave power into the most effective frequency and extending the range of the DEW.

This work demonstrates: 1) the most effective parameters for controlling the bandgap bandwidth and center frequency as the column radius and background dielectric, respectfully 2) the method for controlling these parameters using individually controlled plasma columns, expanding the tunable frequency by at least an order on magnitude, 3) a physical method for implementing the individual

column control in a DBD, using individually addressable electrodes, and 4) digitally implementing the physical control mechanism for multiple plasma columns.

1.1 Dielectric Barrier Discharge Plasma

Atmospheric dielectric barrier discharge is a plasma formation method that creates a plasma at atmospheric pressure using an AC or pulsed discharge. Two electrodes form an electric field greater than the dielectric strength of the gas between them. Accelerated electrons within the field strip electrons off gas molecules, producing ions and more electrons. This avalanche of electrons continues along the electric field lines, eventually creating a conductive path of plasma between the two sides of the gas gap. The dielectric barriers isolate one or both electrodes from the gas, only allowing a displacement current to pass across the DBD circuit. The plasma bridges the gas gap for a conduction current, but the charge is blocked by the dielectric and builds up on its surface. This isolation prevents a runaway conductive path where the increased current would decrease the plasma resistance, driving more current. Eventually enough charge builds up on the dielectric to displace the applied field and eliminate the discharge. The plasma is formed again when the AC polarity reverses and the charge moves in the opposite direction.

For an atmospheric DBD in air with a gap width at 1 mm or greater, the plasma path across the discharge gap takes the shape of a column (diameter ~ 0.1 mm),[1–3] called a "plasma filament." The filament develops by the following process:[4–7] 1) The electric field accelerates free electrons toward the anode electrode and creates an ionization avalanche. 2) Once the avalanche reaches the electrode, the space charge of the avalanche has formed a densely packed grouping of ions. If they satisfy the Meek criterion, then the radius of the avalanche tip forms an electric field that enhances the applied field. 3) An increased number of avalanches occur behind the avalanche tip and follow the ionized path towards the anode. 4) The enhanced ionization behind the avalanche progresses the filament in the opposite direction towards the cathode. 5) The increased ionization forms photons that causes photoionization, further accelerating the filaments progression towards the cathode. 6) Once the column reaches the cathode, the

plasma forms a conductive path and charge is transferred between the two dielectric surfaces until the applied electric field is displaced by surface charge.

Surface charge from previous discharges build upon the dielectric barrier and influence the location of filaments.[8,9] A buildup of charge forms a reservoir for subsequent discharges and an enhanced electric field when the polarity of the electric field flips. Filament discharges preferentially form where a previous discharge occurred due to this surface charge build up. The base of the filaments, where charge collects, called the "filament footprint." Multiple footprints from multiple filaments compete for space over the dielectric, interacting with electrostatic fields. When the dielectric surface is over saturated with filaments, a packing pattern begins to form that forces the filaments into lattice structures.[1] The charge dynamics govern the location of filaments over the surface of the dielectric.

There are two primary types of dielectric barrier discharge with respect to the gas gap: volume and surface.[8,10] These discharges also have different regimes in which they operate from diffuse to filamentary depending upon the discharge conditions.[1,11,12] The volume discharge has a gas gap where the two electrodes are separated completely by the dielectric material and gas. The discharge occurs across the gap and forms standing filaments normal to the dielectric surface. In surface discharge, the electrodes are only separated by the dielectric with no gas gap but the electrode are off-set to the sides. This allows the electric field to form through the gas adjacent to the dielectric surface before it turns into the dielectric towards the second electrode. The plasma then forms on the surface of the dielectric with the filaments extending along the surface.

The atmospheric air DBDs produces highly reactive free radicals in a non-equilibrium plasma. The 100 ns time for current transfer across the filament does not allow enough time for the ions to come into thermal equilibrium with the electrons.[13] This means that the gas can achieve an ionization fraction of 0.001% ($n_e \sim 10^{21}$ m^{-3}) with a low temperature gas (~500 K).[14] This ionization in air produces free radicals of oxygen, nitrogen, and their associated compounds.[15] These radicals are produced over the first 100 ns and then begin to decay after the current has finished its transfer. After 20 milliseconds, N_2, O_2,

and O_3 are the only molecules remaining at a significant quantity.[15] The low-temperature, atmospheric pressure, and working gas of air makes this a very attractive plasma source for industrial processing and manufacturing. Investigation into new technology areas include material processing, airfoil flow control, medical disinfection, combustion efficiency, water treatment, and microwave control.[13]

1.2 Plasma Permittivity

The permittivity is a material property that characterizes the response of charge within a material to an applied electric field.[16] The charged particles within a plasma will counteract the applied field to create a displacement field. The charged particles respond to the field by accelerating along the field until the respective positive and negative charge displacement forms a field equal to the applied electric field or until an oscillating field reverses direction. Since the charged particles have finite mass, their inertial response to the applied field requires a certain amount of time to accelerate. For an oscillating field, this time dependence creates a frequency dependence. A high frequency, that does not give the charged particles time to move, will not be displaced and extend into the plasma. A low frequency, that gives the charged particles plenty of time to move across the applied field, with completely offset the applied field and prevent the electric field from penetrating deeper into the plasma. Since the ion to electron mass ratio is 1836 or greater, the inertial response of the electrons dominates the permittivity. The plasma permittivity (Eq. 1) and the plasma frequency (Eq. 2) are derived in Appendix A by relating the charge motion to an applied oscillating field and equating the resulting electric field coefficient as the relative permittivity.

$$\varepsilon_p = 1 - \frac{{\omega_p}^2}{\omega(\omega + j\nu_c)} \quad \text{Eq. 1}$$

$$\omega_p = \frac{q^2 n_e}{m_e \varepsilon_o} \quad \text{Eq. 2}$$

The electron charge (e) and mass (m_e) respond to an incident wave as an oscillating system with the particle collision frequency (ν_c) damping the response. The relative plasma permittivity modifies the free space permittivity (ε_o) to values less than one, including negative values. This equation is simplified by substituting the characteristic plasma frequency (ω_p), the maximum frequency at which electrons can

fully counteract an oscillating electric field. The collision frequency, defined by Eq. 3,[17] is dependent on the composition of the gas through the gas density (n_g), collisional cross-section (σ_{en}),[18] and drift velocity (u_e),[19] and gradually varies with the electron temperature.

$$\nu_c = n_g \sigma_{en} u_e \qquad \text{Eq. 3}$$

For a propagating wave with a fixed plasma frequency and no collisions ($\nu_c = 0$) there are three different frequency regimes that the incident wave will experience:

1) For $\omega < \omega_p$, the electrons have time to fully react to the incident wave, cancelling out the incident field with the displaced electrons. The incident wave is reflected from this medium and only a decaying imaginary evanescent wave extends into the plasma.

2) At $\omega = \omega_p$, the electrons can only exactly match up with the oscillation of the incident wave The incident wave is reflected from this medium but no evanescent wave extends into the plasma.

3) At $\omega > \omega_p$, the electrons do not have time to fully react to the incident wave. They stay relatively in the same position acting more like fixed charge in a solid dielectric, but still opposing the wave. A portion of the incident wave propagates into the plasma as the electrons can only partially cancel and reflect the incident field.

1.3 Photonic Crystal

Photonic crystals (PC) are artificial periodic structures that form forbidden frequency bands.[16] Periodic structures are of interest to electromagnetic wave propagation when the periodicity is on the order of a half wavelength. At this dimension, bandgaps (a forbidden range of frequencies) are formed that prevent propagation of the wave through the periodic structure. The forbidden bands are reflected rather than absorbed by the PC. The physical mechanism for these bandgaps is Bragg Scattering: an incident wave's signal is cancelled by the collective destructive interference from the reflections at each periodic element. The reflection at each element only occurs if there is a difference between the dielectric of the periodic elements and the surrounding dielectric to produce these reflections.

Another physical perspective for the formation of these bandgaps is based on the location of Bloch waves (waves of the same periodicity as the structure) in the photonic crystal and their frequency dependent upon the wavelength and the permittivity where those Bloch wave resonate.[20] From the two different dielectrics, two separate waves occur for the wavelength that is twice the periodicity of the structure. One concentrated in the background dielectric and one concentrated in the periodic elements. The different dielectrics have different phase velocities (v_p) – the product of the frequency (f) and wavelength (λ), Eq. 4. Since the two waves have the same wavelength but different velocities, they then must have different frequencies. This difference in frequency creates a range of forbidden frequencies which form the bandgap. The size of the bandgap is dependent upon the periodicity, the background dielectric, the periodic element dielectric, and the size of the periodic elements.

$$v_p = \frac{c}{\sqrt{\mu_r \varepsilon_r}} = \lambda f \qquad \text{Eq. 4}$$

An example of the normalized electric field distribution for the two bands within a PC is plotted in FIG. 1. This is for a Transverse Electric Field (TE), where the electric field is out of the page and the magnetic field is in the plane of the page. From the colored concentration, FIG. 1 shows that the lower frequency (Mode #1) is concentrated in the background dielectric ($\varepsilon_{bd} \geq 1$) and higher frequency (Mode #2) is concentrated along the plasma columns ($\varepsilon_p \leq 1$). The mode concentrated along the plasma columns will have a higher frequency than the mode resonating in the background dielectric due to the inverse relationship between permittivity and frequency of Eq. 4.

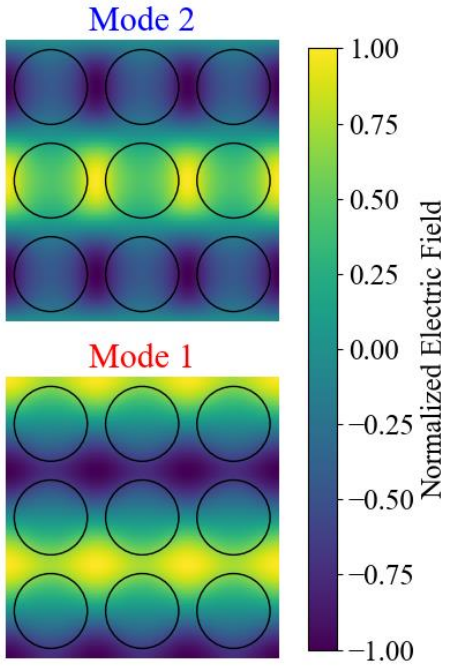

FIG. 1. Normalized electric field distributions of the first two frequency bands. Band #1 is concentrated in the background dielectric ($\varepsilon_{bd} \geq 1$) and Band #2 is concentrated in the plasma dielectric ($\varepsilon_p \leq 1$). This solution does not contain bandgaps for clarity. Band #1 represents the lower frequency band and Band #2 represents the high frequency band.

As a bandgap material, a PC can have paths cut through the material which an incident wave will travel along without being absorbed by the surrounding material. Effectively, PCs form a non-absorbing material to construct different electromagnetic wave components. PCs also have modified dispersion relationships: the phase velocities dependence upon the wavelength. The presence of the bandgap shifts frequencies away from a constant phase velocity, making it dependent upon the wavelength. In this form, the PC can be used to create desired phase velocities and their resulting index of refractions across different frequencies.

PCs are used as either waveguiding material from paths through their structure or index of refraction engineered bulk material. PCs are applied as waveguides, beam splitters, polarizers, photonic circuits, laser resonant cavities, absorbers, attenuator, and antenna substrates.[20–25] More generally, solid-

state photonic bandgaps have been demonstrated or predicted to improve antenna directivity,[26–29] microwave sources,[30,31] and mode converters.[32] Due to the frequency dependence of these bandgaps, applications are frequency specific. To make these components tunable, variable photonic crystals have been developed to change the bandgap width or move the bandgap across frequency space.[33,34] This is accomplished by electrically changing the periodicity or permittivity of the structure; however, it is frequently only viable to control a single physical parameter at one time.

1.4 Plasma Photonic Crystals - A Review

Plasma photonic crystals (PPC), periodic arrangements of plasma columns, have been investigated as a purely plasma-based approach to forming photonic crystals. The benefit to using plasma to construct photonic crystals is its electrically tunable structure, distributed permittivity, and negative permittivity that is necessary for producing left-handed negative index of refraction. MHz - GHz plasma cut-off frequencies and their millimeter scale structures when discharged at atmosphere make them well suited for microwave frequencies.

Compared to conventional photonic crystals, the structures and permittivity of a PPC are inherently electrically variable. The location of the discharge electric field determines the location of the plasma while the strength of the field, which controls the electron density, determines the relative permittivity of the plasma, as defined by Eq. 1 and Eq. 2.[17,35,36] The malleable microstructure is the other attractive aspect for PPCs. A group of organized filaments, in a DBD PPC, act as a photonic crystals creating bandgaps for transverse magnetic or transverse electric waves based on the size, position, and permittivity of individual filaments.[35,37,38] The DBD microstructure can be controlled by the voltage and frequency,[36] enabling a malleable or tunable microstructure.

PPC could provide a frequency variable form of solid-state photonic crystal components. PPCs could be applied to microwave sources,[30,31] antenna directivity,[26,27 28] and mode converters[39] where solid-state photonic crystals have already been demonstrated to provide improved performance. The range of

possible applications is expanded with the range of control over the structure to produce the desirable material wave interactions and properties.

Both experimental and numerical studies have demonstrated PPC potential as a variable microwave device.[35] PPCs have been experimentally demonstrated as microwave filters,[40] waveguides,[41] attenuators,[42] and absorbers.[43] Initial research into PPCs started with Faith and Kuo[44,45] examining the interaction of electromagnetic waves with a periodic plasma array discharged in air. Sakai and Tachibana[35,42,46–48] matched bandgap predictions to experimental measurements of capillary launched dielectric barrier discharge (DBD) PPCs in a square lattice. They also demonstrated the application of a plasma column row as a variable filter, attenuator, and waveguide. Wang and Cappelli[40,41] showed similar filter and waveguide capabilities in plasma capillaries. Dong et al. [49–52] demonstrated an elaborate variety of self-organized DBD structures and their simulated bandgaps, controlled by the driving voltage and frequency. Hojo et al. simulated how a PPC would operate as a beaming antenna structure.[53] Matlis et al.[54] demonstrated the negative refraction of a self-organized DBD PPC and controlled the hexagonal lattice constant and uniform plasma frequency with the gas pressure and driving frequency. Eden et al.[55] demonstrated a PPC square lattice formed from inductive plasma jets and a PPC formed from inductively powered capillaries, where the plasma was controlled by the gas flow rate. These demonstrations of PPC have focused on 2D column structures. These column arrays have been formed by DBD filaments [35,42,56,45–52] or capillary discharge.[40,41,43,57] Some of the capillary PPCs have also been developed into 3D arrays using a wood stack arrangement by both Eden et al.[57] and Cappelli et al.,[58] independently. These 3D PPC are constructed by stacking rows of capillary plasma columns, where the column axis is rotated ninety degrees at each layer. PPC bandgaps have been numerically predicted by the Plane Wave Expansion (PWE) method[46,59,60] and experimentally validated.[40,41,47,54,55,57,61]

The different physical controls, such as the driving voltage, frequency, capillary location, or neutral gas pressure, are all intended to affect the six primary controlling parameters of the PPC bandgap: lattice structure, lattice constant, plasma frequency, plasma column radius, background dielectric, and

plasma collision frequency. In these different cases, the PPC formation method limits or fixes some of the controlling variables. This limits the potential frequency range and the variability over that frequency range.

In order to demonstrate more exotic PPCs numerically predicted by Zhang et al.[62–64] that are capable of negative refraction while remaining tunable, individual column position must be uncoupled from the plasma column permittivity. Another major restriction when tuning PPCs is the plasma column diameter, ~0.1-1 mm, which limits the lattice constant. The plasma column must occupy a significant portion of space within the lattice structure, proportionate to the lattice constant, to create the photonic crystal bandgap effect. In addition, the permittivity of the surrounding background gas or solid capillary structure is fixed. This work will try to address this issue by controlling each individual filament (position and permittivity) to allow for control over the entire shape of the PPC structure.

1.5 Tunable High Power Microwave Applications

High Power Microwave (HPM) applications include: directed energy weapons (DEW), plasma heating, radar, and high energy particle research.[65–67] Space industry applications are focused around beaming power to spacecraft for both fueled and unfueled propulsion schemes.[68] Aerospace military applications use HPM to disrupt circuitry in both aerospace weapons and ground targets.[69–71] Future national defense will require DEW that can defeat hypersonic vehicles and satellites that are too fast to effectively counter with contemporary missiles or ballistic weapons. Drones on the battlefield have already driven the development of an anti-drone HPM DEW. [72] The Tactical High Power Operational Responder (THOR) system has been successfully tested as a counter drone system and is going through the process of being delivered into the military services.[73] Its successor Mjölnir has been contracted by the Air Force Research Laboratory for delivery in 2023.[74] In addition, the proliferation of electronic hardware on the battlefield provides a target that does not require a weapon lethal to humans. This is an attractive option in an increasingly urban battlefield with a high potential for human collateral damage. The Counter-electronics High Power Microwave Missile Project (CHAMP), a HPM DEW system mounted on

a cruise missile was successfully tested in 2012.[75] Its follow-up project, High Power Joint Electromagnetic Non-Kinetic Strike (HIJENKS), is currently under testing.[74] HPM will play an integral part in future US Air Force operations and has been a focus of research at the Air Force Research Laboratory since the 1980s.

HPM DEW infiltrate the circuitry of a target directly through antennas or indirectly through apertures in the external casing.[76] Depending on the beam power when the microwaves reach the target, the microwaves will jam the circuit, flip digital memory, or overload the circuit. Current HPM DEWs are not frequency variable, but pulsed wideband signals, to address the frequency resonance for any potential target. This reduces the delivered power per resonant frequency and so the effective range of the DEW. The frequencies at which a target absorbs microwaves and is vulnerable, is dependent upon the target resonance. The most effective frequencies can be detected by measuring those that are absorbed and not reflected by a probing signal. However, the DEW would then need to have variable components to tune the HPM to one of these vulnerable frequencies.

PPCs are of particular interest for High Power Microwave applications, as plasma provides a durable structure to withstand high power electric fields. Solid-state variable periodic structures on the millimeter scale otherwise fail under HPM due to gas breakdown,[77] material combustion,[78] and losses from failed components due to large electric fields between centimeter scale parts.[79] For plasma periodic structures, gas breakdown defines the microstructure which makes ionization a design consideration rather than a limitation. At most the large electric fields of the propagating wave would modify the already large electric fields forming the plasma structure but would not permanently damage the PPC. These variations could be accounted for by adjusting the PPC control parameters. The PPC could serve as a HPM variable generator to efficiently produce narrow band microwaves over a large tuning range.

HPM are produced by extracting electromagnetic energy from an electron beam at a wave frequency that resonates with a surrounding structure. The different devices that operated based off this mechanism including: magnetrons, klystrons, traveling wave tubes, and gyrotrons.[65,80] If the electrons

experience an electromagnetic field or spatial confinement in one location that compresses them radially, they will bunch together and accelerate electrons ahead and behind the collective bunch. The electrons forced ahead and behind will form their own bunches that again create an interacting restorative space charge force. This space charge oscillation forms an electromagnetic wave that is the desired microwave generation. If the surrounding material limits wave propagation within the material due to its dispersion relationship, the electrons will resonant where there is an intersection between the dispersion relationships of the electron beam and surrounding material. An example of this intersection, where microwaves are produced at the intersection frequency, is presented in the dispersion diagram of FIG. 2. Electrons flowing along the beam have a set velocity (v_b) that defines the dispersion relation of the electron beam ($\omega = k\, v_b$). A surrounding material formed by a photonic crystal will have an engineered non-linear dispersion relationships ($\omega = \omega\,(k)$). The

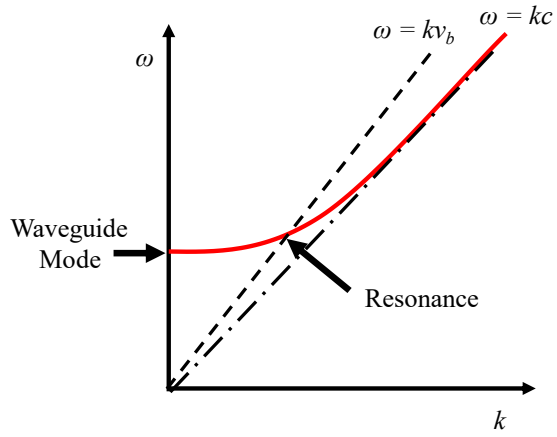

FIG. 2: Waveguide and electron beam dispersion diagram. Microwave generation occurs at the intersection of the electron beam (dashed line) and the photonic crystal (red line). Free space dispersion plotted for reference (dot-dashed line).

Periodic structures used as the dispersive material along the electron beam have been demonstrated in high power microwave generators.[30,31,81–86] The benefit of these generators has been the size reduction and material property dependent frequency which could theoretically be tunable. This dispersion structure can be a PPC with the plasma filaments oriented perpendicular to the electron beam, as presented in FIG. 3. This configuration has been proposed and simulated by Shifler et al for metal

rings.[81] To tune the generating frequency, the spacing and size of the PPC would be changed to shift the dispersion relation of the PPC and change the intercept point, of FIG. 2.

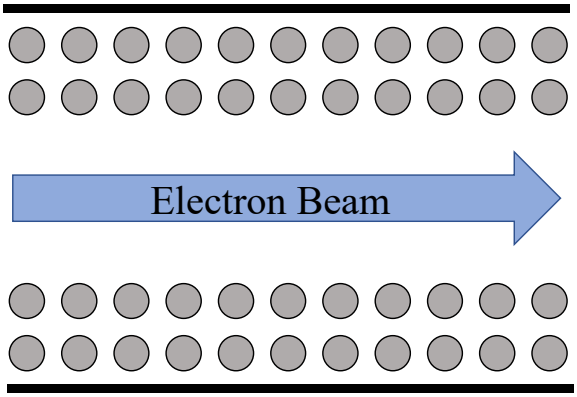

FIG. 3: Schematic of electron beam surrounded by a periodic structure: Microwaves are generated at a resonance between the electron beam and the surrounding photonic crystal.

1.6 Bandgap Simulation Method: Plane Wave Expansion

The Plane Wave Expansion (PWE) method determines a photonic crystal's band diagram, which is a 2D graphical representation of the crystal's dispersion relationship: the frequency (ω) dependence upon the wavevector (**k**), $\omega = \omega(\mathbf{k})$. A plasma-based PWE method is used to model the propagating transverse electric field mode (TE mode - electric field perpendicular to the direction of propagation) of different PPC arrangements. The method incorporates the non-linear effective dielectric of plasma expressed in Eq. 1. The PWE is a numerical approach to solving the Maxwell-Helmholtz equation (Eq. 5) that uses Bloch waves (Eq. 6) in a periodic material to determine the different harmonic bands that can propagate within that material. Bloch waves are a summation of plane waves in Fourier space to represent the electric field (***E***) of a more complex propagating electromagnetic wave as a function of the wavevector (***k***). The conditional periodic dielectric function of the PPC (Eq. 7) is similarly transformed to a sum of all periodic unit cells in Fourier space. The effective permittivity (ε_{eff}), depending on the location (***x***) within the periodic unit cell is either the dielectric constant of the background material (ε_{bg}) or the relative dielectric of the plasma as a function of the propagating wave frequency (ω), the plasma frequency (ω_{pe}), and the collision frequency (ν_c). This definition of the electric field and effective

permittivity are applied to the governing electromagnetic wave equation (Eq. 5) in Fourier space. The expression is reduced to a linearized eigenvalue problem to numerically solve for the possible frequencies, given an assumed wave vector.

$$\nabla \times \left(\nabla \times \boldsymbol{E}(\boldsymbol{x},\boldsymbol{k})\right) = \left(\frac{\omega}{c}\right)^2 \varepsilon_{eff}(\boldsymbol{x})\boldsymbol{E}(\boldsymbol{x},\boldsymbol{k}) \quad \text{Eq. 5}$$

$$\boldsymbol{E} = \sum_n E_n e^{-j\boldsymbol{k}\cdot\boldsymbol{r}} \quad \text{Eq. 6}$$

$$\varepsilon_{eff}(\boldsymbol{x}) = \left\{ \begin{matrix} \varepsilon_{\mathrm{bg}} & ,\ in\ the\ dielectric \\ 1 - \dfrac{\omega_{pe}^2}{(\omega^2 - i\omega\nu_c)}, & in\ the\ plasma \end{matrix} \right\} \quad \text{Eq. 7}$$

The solution to these equations are graphically depicted by the example band diagram of FIG. 4 showing the propagating frequency modes as a function of wavevectors, for a 2D PPC crystal. Each line represents a different propagating mode harmonic and is a frequency solution to the Maxwell-Helmholtz wave equation, Eq. 5. Each increasing frequency band represents a higher order harmonic mode of the lattice structure. The square at the lower left of FIG. 4 represents the Brillouin zone: the smallest unit cell of the PPC that is repeated to form the entire lattice structure. The plasma occupies the area within the circle and the background dielectric occupies the area outside the circle. The inscribed ΓXM triangle defines a locus of points, each associated with a wave vector from the center of the circle to a point around the triangle. The wavevectors in FIG. 4 are those traced clockwise around the perimeter of the triangle with the corners of the triangle labeled on the tick markers to note the progression. The triangle represents all possible wavevectors within the Brillouin zone since they surround an area that can be used to reconstruct the remainder of the Brillouin zone when reoriented.

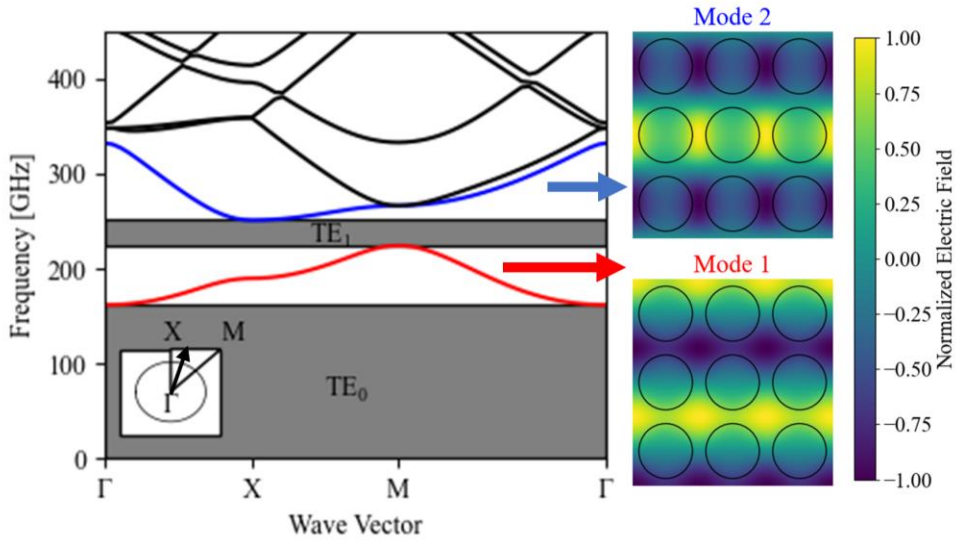

FIG. 4: Example band diagram with field distributions of Mode 1 and Mode 2 field distributions for a wavevector at X. The square in the lower left corner represents the periodic unit cell. The inscribed triangle is the Irreducible Brillouin Zone: the locus of wavevector endpoints emanating from the center (black arrow: example wavevector), which define the limits of possible wavevectors within the unit cell. The dependent variable is the wavevectors associated with the unwrapped ΓXM triangle perimeter.

The relationships between physical parameters of the PPC, defined by Eq. 5, govern the structure of the band diagram. The frequency, normalized by the speed of light in a vacuum, is proportional to the double curl of the electric field and inversely proportional to relative permittivity. The electric fields of different modes will have different spatial distributions within the permittivity, as shown in the first and second modes to the right of FIG. 4. The modes experience different permittivities and spatial gradients due these different electric field distributions. The modes must then propagate at different frequencies for the same wavevector, according to Eq. 5.

If the difference in permittivity and spatial gradients are large enough between modes, a frequency bandgap will form. A bandgap, represented as the grey regions for the first (TE_0) and second (TE_1) bandgaps in FIG. 4, is defined by the range of frequencies over which there are no frequency solutions to Eq. 5. In other words, an incident wave with frequency within the bandgap cannot propagate through the photonic crystal and is reflected. The set of wavevectors surrounding the ΓXM triangle represents the limits of all wavevectors within the PPC so that the bandgaps that exist within the band

diagram identify bandgaps for all TE polarization waves. The limits to the TE_0 and TE_1 bandgaps are determined by the different physical parameters of the PPC: plasma frequency, column radius, lattice constant, and background permittivity.

The TE_0 bandgap is characterized by the area-averaged plasma cut-off frequency. The negative permittivity of the plasma, below the cut-off plasma frequency, prevents waves from propagating through the PPC. The larger wavelengths, at the lower frequencies of the TE_0 bandgap, are several times larger than the periodicity of the PPC and experience the plasma distribution as an area-averaged bulk plasma.

The TE_1 bandgap is bounded by wavelengths that are half the lattice constant, Mode 1 and Mode 2, as shown in FIG. 4. Mode 1 and Mode 2 correspond to two different modes resonating in different areas of the PPC, as shown by the contour plots of FIG. 4: Mode 1 peaks along the background permittivity between the circular plasma columns, while Mode 2 peaks along the row of plasma columns. The inverse-square relation of frequency and permittivity, Eq. 5, describes why the higher frequency Mode 2 resides in the $\varepsilon < 1$ region of the plasma and the lower frequency Mode 1 resides in the $\varepsilon \geq 1$ region of the background dielectric. A decrease of the plasma permittivity, created by an increase of the plasma frequency in Eq. 1, raises Mode 2 away from Mode 1, increasing the bandgap. An increase in the background permittivity will decrease the frequencies of both Mode 1 and Mode 2 proportionately, since both bands have most of their electric field concentrated in the background permittivity. An increase to the column radius will force Mode 2 to concentrate in smaller areas of the background dielectric, increasing the electric field double curl from Eq. 5. The resulting increase of the Mode 2 frequency also widens the TE_1 bandgap. In summary: the bandgap center frequency is controlled by the lattice constant and background permittivity, while the bandgap width is controlled by the column radius and plasma frequency.[87] (This summary is the conclusion to the following Section 2).

2 Simulated Bandgap Parameter Trends

There has already been significant investigation into the trends of PPC bandgaps using a modified Plane Wave Expansion method (PWE) adapted for the non-linear permittivity of plasma. A derivation is presented in Appendix B. Kuzmiak and Maradudin[59] first developed the technique and showed the effects of the plasma filling fraction on the bandgaps. Sakai and Tachibanaz[38,88] used this technique to compare with their experimental results of a square lattice PPC. Qi et. al.[89] performed a normalized trend analysis of the square lattice PPC, varying the background dielectric, plasma frequency, filling fraction. Zhang, et. al. greatly expanded the variety of trend analyses for PPCs: anisotropic dielectric,[90] magnetized plasma,[91,92] Archimedean lattice structures,[93] three dimensional PPCs,[94] omnidirectional incident waves upon 2D crystals,[95] and generalized the model to any plasma shape.[63]

These bodies of work have shown general trends by varying a single variable while holding the rest fixed. The plasma frequency and radius are normalized by the lattice constant so they can be applied over a generic parameter range. Unfortunately, the fixed dielectric constant is held well above atmospheric air and the collision frequency to plasma frequency ratio is two orders of magnitude less than the effective condition in atmospheric discharge. Since the majority of experimental PPCs are formed in atmospheric pressure gas, these analyses can only be related as general variable trends and do not make predictions for what has become the dominant experimental approach. This work presents results with conditions tailored to experimental atmospheric PPCs. From the results, trend proportionalities are presented, a multi-variable polynomial fit of the data is produced for bandgap predictions over a wide variable space, and the PPC frequency and bandwidth dependence upon each variable is compared to identify the optimal controlling variables.

2.1 Simulation Method

The range of variables that define a square lattice PPC are plasma column radius, lattice constant, background dielectric constant, plasma frequency, and collision frequency. The range of variables used for this study is based on plasma discharges in atmospheric air. Independent variation of these variables

enables different discharge arrangements. The plasma frequency depends upon the electron density[16] with a possible range in atmospheric discharge of $10^{15} – 10^{22}$ m^{-3}.[96] We limit this range to $10^{18} – 10^{22}$ m^{-3} for this analysis, producing a plasma frequency range of $0.056 – 5.6 \times 10^{12}$ rad/s. The upper limit of 10^{22} m^{-3} can be obtained by capillary plasma discharge, although at much smaller column radii than used in this simulation.[97] The collision frequency for atmospheric air discharge is $1 – 6 \times 10^{12}$ rad/s based off empirical data.[98] The independent variation of the collision frequency is included to account for the different dependences of the collision frequency and plasma frequency upon the neutral gas pressure and the electric field strength.[98] Although the collision frequency is normally considered invariant for these simulations, using the full range of collision frequency values will quantify the PPC bandgaps lack of dependence on the collision frequency.[63] The radius covers the range from a plasma filament radius of 50 um up to 400 um to allow for spacing between the columns for all lattice constant values.[99] The lattice constant range of 1 – 2 mm forms wavelengths at the lowest end of the microwave range and is characteristic of both capillary[88] and self-organized DBD[54] PPCs. For the structure to effect dispersion on the propagating waves, the plasma columns must have spacing on the order of the wavelength with plasma columns large enough to sufficiently influence the wave. Initial runs of the simulation supported the choice of range for the lattice constant.

2.2 Effect of PPC Variables on Bandgap

2.2.1 Effect of a Single Variable

The simulations produce multiple data points across the investigated multivariable space, which were catalogued along with the two bandgaps (TE_0 and TE_1). The calculated bandgaps over the five-dimensional variable space were analyzed to determine trends associated with each variable and compare their effectiveness at controlling the bandgaps. FIG. 5 shows the effect of changing a single variable while all other variables are held constant at a common baseline case. The solid and dashed curves in FIG. 5 are polynomial curve fits to the data (markers) that will be described in a subsequent section. The baseline case values are: background dielectric of 1.0006, collision frequency of 1×10^{12} rad/s, lattice constant of

1.0 mm, radius of 0.4 mm, and plasma frequency of $5.6x10^{12}$ rad/s. There are two sets of data in FIG. 5a corresponding to the solid and dashed curve fits. These are the data of the upper and lower limits, respectively, that define the TE_1 bandgap. FIG. 5b shows the upper limit for the TE_0 bandgap. The FIG. 5b plot only has a single curve because the bandgap extends down to zero frequency. In other words, the lower limit of the TE_0 bandgap is zero. Note that in FIG. 5 the data and curve fits emanate from a common data point at the top left corner of the plot. This is the baseline case bandgap, and it has an upper limit of 410 GHz and lower limit of 270 GHz for the TE_1 bandgap, and an upper limit of 265 GHz and lower limit of 0 GHz for the TE_0 bandgap. Finally, note that in FIG. 5 and all following figures, the radius and plasma frequency x-axes are flipped (descending to the right) because of the inverse dependence of frequency on those variables. This dependence is explained in the following section.

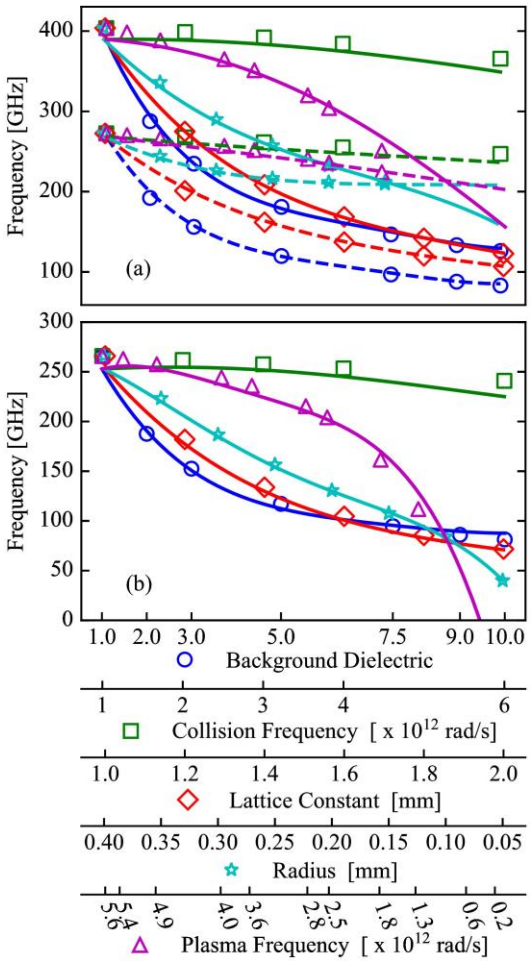

FIG. 5. Example modeled values (symbol) and multi-variable curve fits (lines, curve fits) of bandgap limits as functions of different variables with all other variables held constant. a) TE_1, upper limit (solid) and lower limit (dashed) b) TE_0. Note: The radius and plasma frequency axes are descending.

The data points in FIG. 5 show the effect of a single variable on the bandgap limits when all other variables are fixed with the baseline values. However, the trends shown in FIG. 5 are consistent throughout all variable space. That is, the trends are the same even when the other variables have values different than the baseline. We explore and explain those trends here.

The distribution of electromagnetic energy within static photonic crystals, as described by Joannopoulos,[20] helps to explain the bandgap trends observed in this PPC. The bandgap is formed by the concentration of the upper and lower propagating bands within the Brillouin zone. The lower band concentrates in the higher permittivity material (air) and the higher band concentrates in the lower

permittivity material (plasma). Since the permittivity is inversely related to the phase velocity of a wave, the permittivity of air versus plasma serves to raise the higher band frequency relative to the lower band frequency. An increase in the plasma frequency (reduced permittivity) or radius (reduced area averaged permittivity) increases frequency and the dielectric disparity between the two bands. The plasma frequency, collision frequency, and background dielectric directly affect the average effective permittivity, while the radius and lattice constant affect the relative areas of the two materials. The lattice constant and background dielectric affect the band diagram that would exist for a periodicity of the lattice constant without the inserted plasma columns. The inserted plasma column then modifies this band diagram to form the bandgaps.

The results from FIG. 5 can be compared with the proportionalities in the governing equation, Eq. 5, to further explain the trends. The following approximate expressions are intended to illustrate a simplified analytic proportionality, validate the trends in FIG. 5, and provide an intuitive explanation for those trends. The different variables are roughly approximated by directly substituting them into Equation Eq. 5. The process is conducted separately for each variable with all other variables as constant. The result is a proportionality solely between the frequency and variable of interest produced by the governing equation.

For the background dielectric, the variable is substituted for the effective permittivity (ε_{eff}) term. The plasma frequency and collision frequency – the variables of the plasma dielectric function – are ignored since they remain constant. The equation is rearranged and simplified by eliminating constant terms to produce the proportionality of Eq. 8 between the frequency and background dielectric. This expression reflects the common change in frequency of a propagating wave within a medium of a different permittivity. The inverse square relation agrees with the trends observed in FIG. 5 for the TE_0 as well as the upper and lower TE_1 limits. Since the variable is not dependent upon the frequency, it remains consistent across all three band limits producing an almost constant bandwidth for the TE_1. The

background dielectric affects the background wave propagation that would produce the initial band diagram that is shifted by the addition of the plasma column.

$$\omega(\varepsilon_{\mathrm{bg}}) \propto \frac{1}{\sqrt{\varepsilon_{bg}}} \qquad \text{Eq. 8}$$

For the plasma frequency, the plasma dielectric function in Eq. 7 is substituted for the effective dielectric of Eq. 5. The frequency term (ω^2) in Eq. 5 is isolated, while the frequency term from Eq. 7 is kept in the dielectric function and considered constant as its variation is small compared to the plasma frequency variation. The dielectric function is rearranged and both sides of the equation are square rooted to relate the frequency to the plasma frequency, Eq. 9. The dielectric function and electric field terms are separated to isolate the variational and constant terms, respectively. The dielectric term, inside the square root, is positive as long as the plasma frequency and collision frequency are larger than the propagating frequency, which is the case where the bandgaps exist in FIG. 5.

$$\omega = \pm \sqrt{\frac{1}{\frac{\omega_{pe}^2}{\omega^2\left(\frac{i\nu_c}{\omega} - 1\right)} + 1}} \sqrt{c^2 \frac{\nabla \times \left(\nabla \times E(\boldsymbol{x}, k)\right)}{E(\boldsymbol{x}, k)}} \qquad \text{Eq. 9}$$

Assuming a constant collision frequency and a frequency smaller than the plasma frequency, the plasma frequency is inversely proportional to frequency, Eq. 10. Since there is a sign ambiguity from the square root, a negative value is chosen to reflect the same negative inverse trend observed in the data of FIG. 5. This trend relationship requires an addition term to shift the frequency positive. The PWE data is the eigenvalue for the linear sum of the Eq. 7 in Eq. 5, so the vertical shift can be interpreted as the addition of a background dielectric term. The frequency with respect to plasma frequency, in FIG. 5, increases towards the upper limit of the next bandgaps lower limit. This is most apparent for the lower band, which forms the upper bound of the TE_0 bandgap (FIG. 5b) and the lower bound of the TE_1 bandgap (FIG. 5a). Both boundaries approach each other at the maximum plasma frequency of 5.6 $x10^{12}$ [rad/s], when the upper boundary of the TE_0 bandgap is 265 GHz and the lower boundary of the TE_1 bandgap is 272 GHz. The increase in plasma frequency drives the band towards a flat band, a single

frequency for all wavevectors. Physically, the negative plasma permittivity forces the waves to propagate outside of the plasma column region, narrowing the possible wavelengths and frequencies for the harmonics to exist in. The plasma frequency primarily affects the bandgap by narrowing the propagating frequency band and only weakly increases the frequency magnitude once the band narrows.

$$\omega(\omega_p) \propto -1/\omega_p \qquad \text{Eq. 10}$$

For the collision frequency, the plasma frequency is held constant in Eq. 9 and the dielectric function rearranged to produce Eq. 11. Since the collision frequency and plasma frequency are 3-15 times larger than the frequency, the ($1i$) terms in the numerator and denominator are ignored, and the dielectric term is rearranged to the trend proportionality in Eq. 12. The plot of the resulting relationship takes on a negative root relation that depends upon the ratio of the (ω_p^2 / ω) to the collision frequency. Since the square of the plasma frequency is one to two orders of magnitude larger than the propagating frequency, Eq. 12 produces a proportional change to the frequency one to two orders of magnitude smaller than the change in collision frequency. The negative sign is chosen to agree with the plasma frequency trend sign. Both a gradual downward slope with a change two orders of magnitude smaller than the collision frequency are observed in all three of the bandgap limits of FIG. 5. With the minimal change, the curvature from the root is not observable the PWE data of FIG. 5.

$$\omega = \pm \sqrt{\frac{\frac{\nu_c}{\omega} + 1i}{\frac{\nu_c}{\omega} - i\frac{\omega_{pe}^2}{\omega^2} + 1\text{i}}} \sqrt{c^2 \frac{\nabla \times \left(\nabla \times E(\boldsymbol{x}, k)\right)}{E(\boldsymbol{x}, k)}} \qquad \text{Eq. 11}$$

$$\omega(\nu_c) \propto -\sqrt{\frac{1}{1 - i\frac{\omega_{pe}^2}{\nu_c \omega}}} \qquad \text{Eq. 12}$$

For the dimensional variables, a more approximate relationship must be established since exact substitution components, like the plasma dielectric function for the effective permittivity, do not exist. From dimensional analysis, the inverse lattice constant (a) is substituted for the del operator (∇) with units [mm^{-1}] ($1/a \propto \nabla$). The double curl applies a square term to the lattice constant. Now all parameters except for the lattice constant and frequency are held constant and disregarded. The rearranged equation and

elimination of exponents on both terms produce an inverse proportionality between frequency and the lattice constant. In comparison with FIG. 5, this agrees with the inverse relationship of all bandgap limits. Physically, the lattice constant changes the wavelength of the initial band diagram that the plasma column modifies.

$$\omega(a) \propto \frac{1}{a} \qquad \text{Eq. 13}$$

The radius of the plasma column effects the frequency by increasing the area where the bands reside in the lower and upper dielectric medium. Eq. 5 does not have a constant component accounting for this effect for which the radius can then be substituted. However, this physical description suggests a proportionality to the area of the plasma column. The frequency then forms a squared proportionality with the radius, Equation Eq. 14. With increased radius, an increased portion of the unit cell is composed of the low permittivity plasma, and the total average effective permittivity is reduced, increasing the frequency. The high band experiences a larger effect from the change since it primarily resides in the low permittivity area of the plasma. In FIG. 5a, the upper limit of the TE_1 bandgap has a greater parabolic trend curvature than the lower limit. In FIG. 5b, the upper limit of the TE_0 bandgap is slightly parabolic approaching a linear relationship. Since the upper limit is formed by the propagating band that resides in the background dielectric material, a reduced curve may be expected. In FIG. 5a, the lower limit of the TE_1 bandgap approaches a constant value at the low-radius values, showing that the radius primarily affects the bandwidth of the bandgap and is limited on its ability to change the magnitude of the frequency.

$$\omega(r) \propto r^2 \qquad \text{Eq. 14}$$

Although the widths of both bandgaps can vary due to a bias towards higher frequencies, normalized bandwidths – the difference between the upper and lower limit normalized by the center frequency of the bandgap – mitigates the frequency bias by reducing the relationship to the relative difference between the limits. Example trends of the normalized bandwidths of the TE_1 bandgap are presented in FIG. 6 for the same conditions shown in FIG. 5. The TE_0 bandwidths are not presented since

the normalized bandwidth between an upper limit and zero will have a constant value of 2. The trends are related to the frequency variations previously discussed and the physical effects on the two bands located in different areas of the unit cell to form the limits of the bandgaps.

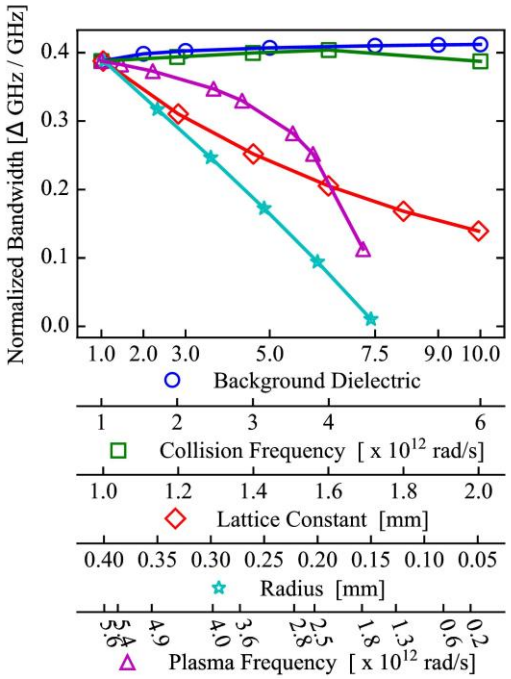

FIG. 6. Bandgap normalized bandwidth as a function of different PPC parameters for TE_1. Each line represents the variation of a parameter over its range with all other parameters held constant. Each line is referenced back to the same set of parameter values that produce the 375 GHz center frequency point. Note: The radius and plasma frequency axes are descending.

Increasing the plasma frequency decreases the dielectric constant within the plasma. Since the higher band primarily resides within the plasma, the plasma frequency has a larger effect on the upper band limit raising it away from the lower band. Within each band, the plasma permittivity is also larger for lower frequency wavevectors, Eq. 7, disproportionately raising the lower frequencies of the band relative to the higher frequencies. This translates to a divergence of the upper bandgap limit from the lower bandgap limit. The size of this bandgap is limited by the lower limit of the next higher bandgap and approaches the previously discussed frequency trend. The collision frequency is relatively constant compared with the other trends due to the minimal change with collision frequency defined by the

frequency trend, Eq. 12. The background dielectric trend is nearly constant, since the background dielectric trends remain constant between the two bandgap limits.

Spatial variation to the structure changes the proportions of the two different dielectric mediums through which the two bands propagate. The change in the radius creates a larger area of plasma where the higher band concentrates. The larger low-permittivity area increases the frequency of both bands as explained with the frequency trend. However, the high band experiences a larger effect from the radius since it primarily resides in this low-permittivity area. The frequency normalized difference between the two radius-dependent, proportionally squared, bandgap limits (the upper limit of the TE_0 bandgap and the lower limit of the TE_1 bandgap) produce a linear proportionality. A linear proportionality of the normalized bandwidth as column radius increases is observed in FIG. 6. The decreasing bandwidth with respect to the lattice constant, in FIG. 6, is due to a fixed radius. As the lattice constant increases, the fixed radius reduces the fill fraction of the unit cell, reducing the upper bands deviation from the lower band. This produces the opposite trend of the radius: a decreasing linear relationship. The slight curve is explained by the inverse relationship of the lattice constant with frequency. The lattice constant affects the frequency magnitude by the inverse relationship and the bandwidth through the constant radius.

2.2.2 Multi-variable Polynomial Fit

The data for the different bandgap limits exist over a five-dimensional variable space, difficult to fully represent in figures. To highlight this difficulty, three carpet plots are presented in FIG. 7. that present two independent variables and the two dependent variables of the bandgap bandwidth and center frequency. The other three independent variables of the PPC are held constant in each plot. The ranges of each variable are reduced to exclude variable space where the bandgaps do not exist. These plots demonstrate that even in the case where four axes are used the available information is significantly limited from the full variable and frequency space. However, the proportionalities of the data make polynomial fitting a viable option for representing each frequency limit of the bandgaps as functions of all five variables.

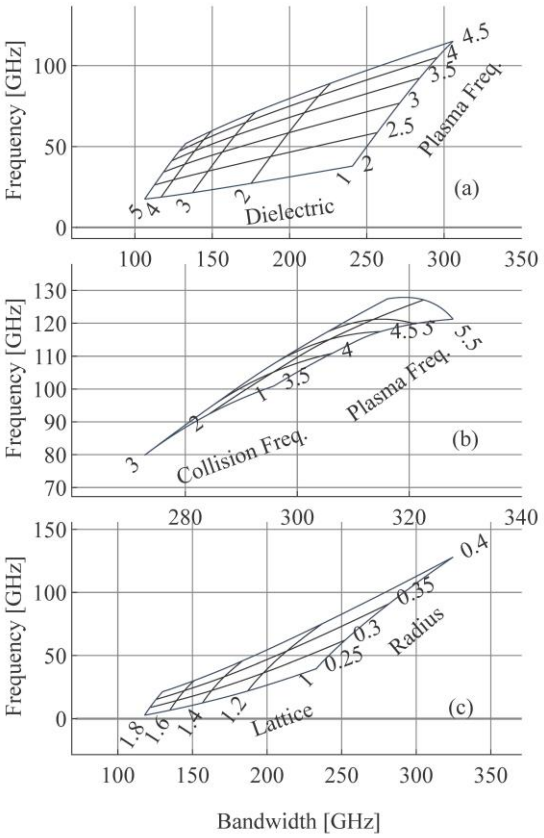

FIG. 7. Bandgap characteristics (Center Frequency and Bandwidth) as functions of two control variables (a) Plasma Frequency [10^{12} rads / s] and Dielectric Constant, (b) Plasma Frequency [10^{12} rads / s] and Collision Frequency [10^{12} rads / s], and (c) Column Radius [mm] and Lattice Constant [mm]. For each plot, the other three respective variables are held constant at the same constant values for FIG. 2.

We create a numerical fit to the data using a 5 dimensional 4th order polynomial with R^2 and average error values presented in Table 1. The polynomial coefficients for each curve are reported in Appendix C, where the sum of all variable terms and their respective coefficients return the bandgap frequency limit specific to each column. These curve fits are intended to provide easy bandgap predictions for PPCs of atmospheric discharge and square lattice structures. The polynomial fits have also been used in this work to determine the gradient of the frequency with respect to the entire variable space.

Table 1. Curve fit agreement with PWE data values.

Limits	% error	R^2
Upper - TE_0	8.44	0.991
Lower - TE_1	1.84	0.998
Upper - TE_1	2.19	0.998

Examples of the three polynomial curve fits are shown as curves in FIG. 5 for comparison with the calculated PWE data shown as symbol markers. Comparison of the data points (individual model simulation points) with the smooth curves (polynomial fit) shows close agreement and validates the average error calculated and presented in Table 1. An issue with the continuous polynomials is their inability to capture the non-continuous nature of the bandgaps that disappear as the bandwidth decreases to zero. This is dealt with by only accepting TE_1 bandgaps returned by the polynomial curve fit that have a positive difference between the upper and lower limiting line pairs such that the bandgap disappears when they cross. The TE_0 bandgaps are similarly dealt with by only accepting polynomial curves greater than zero. Since the polynomials are 4^{th} order, some limiting line pairs cross multiple times within the chosen variable ranges forming false positive bandgaps. For this reason, a plot like FIG. 5 is necessary to determine if a bandgap formed from a single set of variables correctly returns a bandgap predicted by the PWE method. To evaluate the existence of a single bandgap, the set of variables which defined that bandgap are used as the baseline in FIG. 5. If the limits plotted along each variable of this new FIG. 5 decrease and do not cross between the y-axis and the location of the baseline values, then the bandgap does not form a false positive and the bandgap exists.

2.3 Parameter Metrics

The center frequency and bandwidth of the bandgap are the two characteristic parameters of this PPC. Each variable (radius, background dielectric, plasma frequency, collision frequency, and lattice constant) changes these parameters. PPC performance can be reconfigured or controlled by adjusting one or more of these variables. However, each variable affects the center frequency and bandwidth with a

different degree of sensitivity and provides a different operational parameter range. These two metrics – sensitivity and operational range – are evaluated in the following sections.

2.3.1 Operational Frequency Range

The variation of bandgap size and frequency over all variable space makes determining the operational frequency range per variable difficult. Here, we define the operational range of the PPC based on the maximum and minimum frequencies when a single variable is held fixed and all other variables are allowed to vary over their respective ranges. This is shown in FIG. 8 for the TE_1 bandgap. In FIG. 5a, we plotted the maximum and minimum frequencies when all other variables were held constant at the baseline bandgap configuration. Here, in FIG. 8, all other variables can change across their respective ranges. FIG. 8 therefore shows the maximum and minimum possible frequency when all variables are able to change across their entire ranges. The upper and lower frequency limits are defined by the solid and dashed lines, respectively. The other non-fixed variables along the line limits are allowed to be any value within their respective ranges, however, these parameters fix on a constant sets of parameter values that maximize or minimize each frequency limit. The frequencies between these lines are continuous since there are four other independent variables to vary. For the TE_0 bandgap, the operational frequency range is represented by FIG. 5b. This is because the baseline variable set of FIG. 5b is always the largest possible TE_0 bandgap for the variable space. So variable variation away from this point defines the upper limit of possible bandgaps over each variable range. Since the TE_0 bandgap has no lower limit, the data in FIG. 5b defines the upper limit of the operational frequency and zero defines its lower limit.

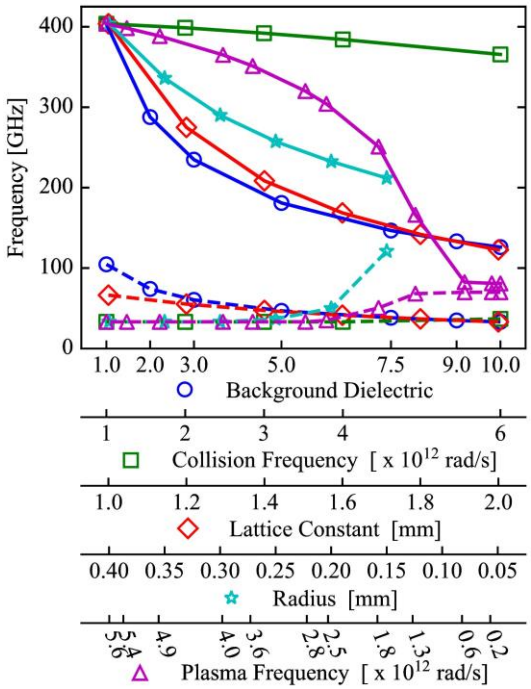

FIG. 8. The range of frequency space available to a fixed variable value for the TE_1 bandgaps, upper limit (solid) and lower limit (dashed). All combinations of the dependent variable value and all other parameter values produce a range of bandgaps over frequency space, to define the maximum frequency range. The same type of plot for TE_0 is represented by FIG 5b. Note: The radius and plasma frequency axes are descending.

Larger frequency ranges identify variable values that produce more bandgaps to populate the frequency range or wider bandgaps to spread across the frequency range. Significant changes to the frequency range over each axis identifies necessary variable values beyond which the control from the other variables is severely limited. For example, a plasma frequency less than 0.6 $x10^{12}$ [rad/s] along the plasma frequency curves in FIG. 8 produces only a very narrow frequency range of bandgaps. Over this variable space, the maximum frequency range appears independent of the plasma frequency. Examination of the other variable values reveals that any existence of a bandgap below the 0.6 $x10^{12}$ [rad/s] plasma frequency cutoff is due to a background dielectric greater than 7.5. For the TE_0 operational frequency range in FIG. 5b, bandgaps do not form without a plasma frequency above 0.6 $x10^{12}$ [rad/s]. Unlike the TE_1, TE_0 will not form bandgaps from a difference between the dielectric background and the column of air over this range of values. The plasma frequency is essential in forming a lower cutoff frequency. The

column radius also plays a significant role in the existence of the bandgap. TE_1 bandgaps are completely eliminated below a radius of 0.15 mm and the operational frequency is halved to 90 GHz from 0.20 to 0.15 mm. At 0.05 mm (the radius of an atmospheric plasma filament), the TE_0 bandgap still exists but the operational frequency range has been greatly reduced to 40 GHz.

The variables that cover the least amount of frequency space are the most limiting to the operational frequency ranges since they produce the largest change to the operational frequency range. For example, the lattice constant and background dielectric in FIG. 8 bound the smallest areas and cannot operate above 200 GHz for half of their variable range, which makes access to the higher frequencies significantly dependent upon these two variables. The values at the extreme left end of all variable ranges, where the intersection of the upper limits (solid lines) meet, are needed to produce a bandgap reaching to 400 GHz. The frequency ranges with the largest areas and little change identify variables that have the least influence on the operational frequency range. For the collision frequency, the near constant boundary lines show that the frequency range is primarily dependent upon the other parameters.

2.3.2 Parameter Sensitivity

Parameter sensitivity to a variable is determined by the gradient of the parameter function (bandwidth and center frequency). The gradient applied to a parameter provides the degree of change with respect to each variable, and this is what we call the sensitivity. The gradient averaged over all variable space, Eq. 15, returns a measure of how much each variable affects the parameter – how sensitive the parameter is to each variable. To eliminate bias towards higher frequencies, the gradient is normalized by the frequency at which the gradient is evaluated. This ensures that the metric is focused on the sensitivity rather than the magnitude of change, which would be greater at higher frequencies. The averaged gradient is further normalized by the total range of each variable. This scales the sensitivity to the available variable range rather than the variable units. Without this normalization, sensitivities of different variables that have different units or different ranges would not be comparable.

$$\langle \Delta r\ \overline{\frac{1}{f}\frac{\partial f}{\partial r}}, \Delta\varepsilon \overline{\frac{1}{f}\frac{\partial f}{\partial \varepsilon}}, \Delta\omega \overline{\frac{1}{f}\frac{\partial f}{\partial \omega}}, \Delta\nu \overline{\frac{1}{f}\frac{\partial f}{\partial \nu}}, \Delta a \overline{\frac{1}{f}\frac{\partial f}{\partial a}} \rangle = \frac{\int\int\int\int\int \frac{\nabla f(r,\varepsilon,\omega,\nu,a)}{f(r,\varepsilon,\omega,\nu,a)}\, dr\, d\varepsilon\, d\omega\, d\nu\, da}{\int\int\int\int\int\ dr\, d\varepsilon\, d\omega\, d\nu\, da} \cdot \langle \Delta r, \Delta\varepsilon, \Delta\omega, \Delta\nu, \Delta a \rangle \quad \text{Eq. 15}$$

The sensitivity of each parameter (bandwidth and center frequency) to each variable is presented in Table 2. The bolded values identify the variables that parameters are most sensitive to. If it were desirable to have a variable with the largest effect on bandwidth, but a minimal effect on center frequency, one would view the bolded values in the bandwidth column of Table 2, and select a variable that is not bolded in the center frequency column, such as the column radius. Similarly, the variable with the largest effect on center frequency with minimal effect on bandwidth is the background dielectric. Although the lattice constant has a significant effect on both the bandwidth and center frequency, it does not uniquely affect only one. Ideally, one variable would control one parameter without affecting the other parameter. Collision frequency is the least effective at producing a significant change in either parameter relative to the other variables. Although this also implies that changes to the collision frequency, which occur while tuning another controlling variable (such as increasing the electric field to tune the plasma frequency), could be disregarded. In this way, optimal sensitivity variables for controlling the two different parameters can be identified. The parameter sensitivities in Table 2 correspond to the trends found in Section 2.2. 2.2.1. The radius and plasma frequency primarily affect the bandwidth, the background dielectric primarily affects the center frequency, the lattice constant affects both, and the collision frequency significantly affects neither.

Table 2. Parameter sensitivities. Bolded regions identify the largest sensitivities.

Variables	Bandwidth	Center Frequency
Background Dielectric	-0.030	-0.172
Collision Frequency	-0.022	-0.015
Lattice Constant	-0.043	-0.113
Column Radius	0.059	0.041
Plasma Frequency	0.035	0.024

As with the operational frequency range analysis (FIG. 8 above), the effective variable range can be evaluated by plotting the gradient over the respective variable range, FIG. 9. To define the gradient as a function of each variable, the gradient is averaged over all other variables except for the variable with respect to which the gradient is taken. The largest gradient values in FIG. 9, where the variables are most effective, are at one end of the variables range (i.e., the left side of FIG. 9). This preference for a higher or lower value is due to the exponential trends demonstrated in FIG. 5 and FIG. 6.

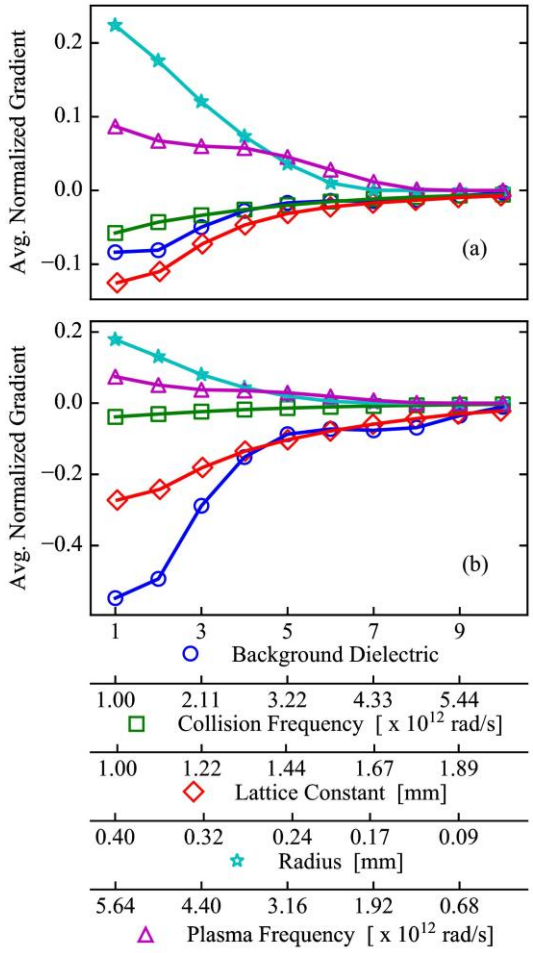

FIG. 9. Averaged normalized gradient of the (a) bandwidth and (b) center frequency. Note: The radius and plasma frequency axes are descending.

Specific effective ranges can be determined by setting a desired level of sensitivity. Using the bandwidth gradient in FIG. 9a as an example, if ±0.05 is chosen as a cut-off for an effective normalized average rate of change, then only 5% of the collision frequency range is effective while 32% of the lattice

constant range and 40% of the column radius range (0.4 - 0.26 mm) is effective. However, 39% of the plasma frequency range remains effective even though it is a less sensitive variable. FIG. 8 can help identify a variable that remains consistently effective, as defined by the cut-off value, even though the total sensitivity metric (Table 2) does not significantly identify it as a sensitive variable. Since the values in FIG. 8 are still averages across all other variables, these trends can be accepted to describe the effective variable ranges over all other variable space. The cut-off level can be chosen based on the less sensitive variables. For example, a cut-off level of ±0.056 can be used for the center frequency sensitivity since all the less sensitive variables fall below this value. Below this value, the preferred variables (bolded in Table 2) would no longer have a distinctive advantage over the other variables. With this criterion the background dielectric has an effective range of 1.006 to 3.8 (31% of total range) and the lattice constant an effective range of 1.00 mm to 1.23 mm (23% of total range).

2.4 Conclusion: Bandgap Parameter Trends

A PWE model was used to calculate the bandgaps of an atmospheric PPC over a five-dimensional variable space: plasma frequency, collision frequency, plasma column radius, background dielectric constant, and lattice constant. Frequency trends were related to the governing equations to identify proportionalities. The bandwidth trends were related to the location within the Brillouin zone of the upper and lower bands that bound the bandgap. The changes to the physical structure and material properties of the PPC produced trends consistent with the general proportionalities of the governing equation and physical understanding of band distribution within the PPC. Polynomial fits of the upper and lower frequency limits provide equations with an average of 8% error for the TE_0 bandgap and 2% error for the TE_1 bandgap. The polynomials were then used to characterize the different variables with their normalized average gradients. The sensitivity and operational range of the PPC bandgap bandwidth and center frequency were assessed.

Column radius and dielectric background are the most effective variables for controlling the bandwidth and center frequency, respectively. The lattice constant is similarly effective but would simultaneously change both parameters.

The maximum frequency range provided by the variable ranges investigated here is 25 – 400 GHz for the TE_1 bandgap and 0 – 250 GHz for TE_0 bandgap. Doing the same but while holding one variable value constant demonstrated how each variable affected the total possible frequency range. The collision frequency had the smallest effect on the range, decreasing it by only 50 GHz. A plasma frequency less than 0.6×10^{12} [rad/s] reduced the total range to only 70 – 80 GHz for the TE_1 bandgap and eliminated all TE_0 bandgaps. Below this value, only the background dielectric produces a TE_1 bandgap. Both the TE_0 and TE_1 band gaps are eliminated with a radius less than 0.15 mm.

It is found that in many cases only a fraction of the total available variable range is effective at controlling the PPC. The variables and ranges to affect the greatest bandwidth and center frequency change respectively are column radius (0.4 – 0.26 mm) and background dielectric (1 – 3.8). However, from the frequency range metric, the high end of the background dielectric range is necessary for accessing TE_1 bandgaps below 100 GHz.

3 Simulated Effective Parameters for Expanded Tuning

The major restriction of these PPCs tunability is the fixed plasma column radius and background permittivity set by the surrounding gas or solid capillary structure. Our previous work has shown that the column radius and background permittivity are the primary variables for setting the bandgap width and frequency,[87] and these physical limitations of the PPCs greatly limit their frequency variability. Our previous work showed that multiple PPC parameters are needed to independently control both the bandgap width and average frequency.[87] This increases both the range of frequencies over which a single lattice arrangement can operate and their tunability over that range.

This work focuses on increasing the PPC variability with locally controlled electron density with in each plasma column to provide macroscopic changes in the plasma-wave interaction. Our previous experimental work has shown control of an individual DBD plasma filament within an array of filaments by biasing the electrode on the rear of the dielectric.[100] The dielectric surface charge was determined to be the controlling mechanism.[101] This process provides a way forward for controlling an array of individually controlled plasma columns at the scale investigated in this paper. The plasma column distributions of these effective parameters are illustrated for a 2D PPC in FIG. 10. The lattice constant is increased by turning off every other column. The effective plasma radius is increased by forming clusters of columns, separated by areas of turned-off columns. The background permittivity can be decreased for this new lattice constant by adjusting the plasma density of surrounding columns. This added parameter control increases the degree of control and allows for lower bandgap frequencies. This work investigates the advantage of individual localized column control through simulation predictions from the PWE method. The specific PWE method used in this study was developed by Kuzmiak and Maradudin[59] for the frequency dependent plasma permittivity of Eq. 1, and adapted for an arbitrary plasma distribution by Zhang,[47,59,60]

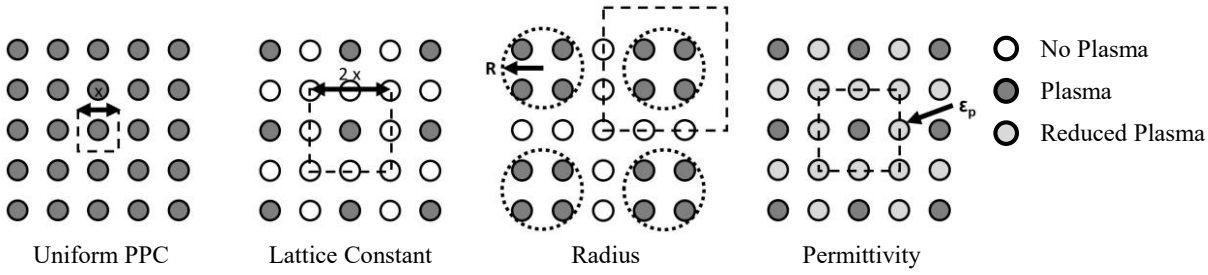

FIG. 10: Effective parameters formed from a PPC with individually locally controlled plasma columns. The effective parameters are evolved from the conventional Uniform PPC. The dashed boxes identify the periodic unit cell for each PPC.

3.1 Adapted PWE Method: Supercell

In order to simulate the individually adjustable plasma frequencies, the "unit cell" representing the periodic element of the PPC structure is expanded to include multiple plasma columns. The result is defined as a "supercell"[102] and is presented in the lower right corner of FIG. 11 with the unit cell in the upper right for comparison. The supercell contains four individual columns of the PPC but is still periodic with this pattern of four columns. The Brillouin zone, of the unit cell and supercell, are the triangular outline in reciprocal space (the inverted space of the Fourier transform used to simplify Eq. 5) which defines the limits of wavevectors in the 2D space. The Brillouin Zone is constructed from the locus of points that define these wavevectors as they emanate from the center of the unit cell and supercell, as shown in the left of FIG. 4. The change in periodic length means that the wavenumbers ($k = 2\pi/\lambda$) used in the PWE simulation are proportionately reduced, due to the inverse relation between wavenumber and wavelength (λ). This causes the irreducible Brillouin zone triangle of the unit cell and supercell to overlap as shown in FIG. 11. Understanding the relationship between the Brillouin Zones of the unit cell and supercell is necessary for validating the supercell band diagram.

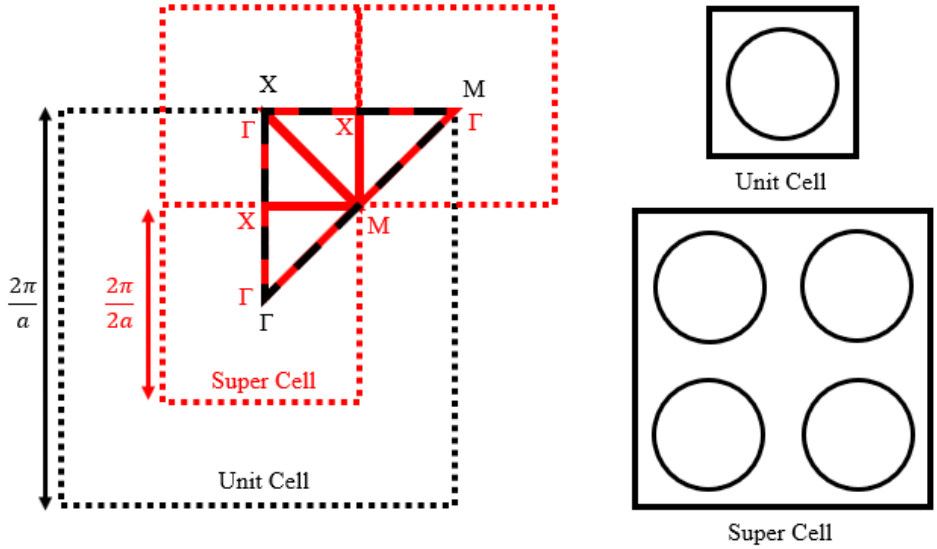

FIG. 11: The Unit Cell and Supercell in reciprocal space with their respective overlapping Brillouin Zones.

In FIG. 11, the path along the unit cell triangle (black-dotted lines) from Γ to X is replicated in the supercell by the path (red-solid lines) from Γ to X to Γ. The bandgap of the supercell and unit cell are plotted together in FIG. 12 for two independent variables: their respective Brillouin zone paths (right) and scaled to the same unit cell Brillouin zone path (left). The Brillouin zone of the x-axis in FIG. 12 are associated by color to the paths in FIG. 11.

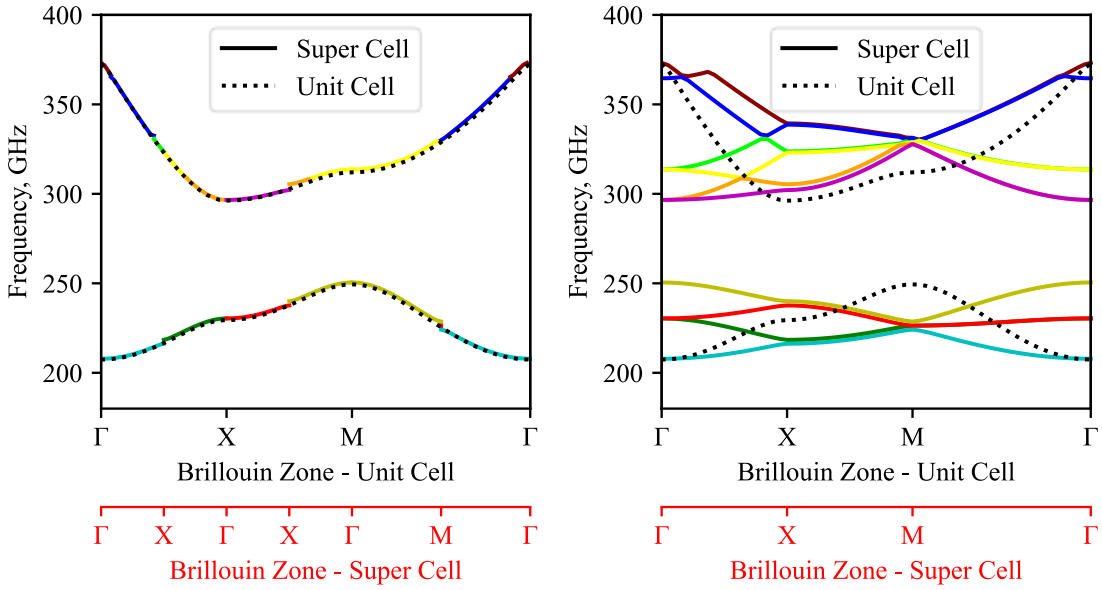

FIG. 12: Example of Unit Cell and Supercell simulations for the same PPC parameters (radius: 0.45mm, plasma frequency: 300 GHz, lattice constant: 1 mm, background relative permittivity: 1). The Supercell solution along the Unit Cell Brillouin Zone (left), following the path defined in FIG. 11. The Supercell and Unit Cell solutions along their respective Brillouin Zones (right).

Discontinuities between the supercell's extra mode lines create one source of numerical error. This is addressed by using a simulation mesh area of 203 nodes per side of the unit cell for a total 41,209 nodes and limited the difference between mode lines that should overlap to <1% of the mode bandwidth. This value is significantly less than the calculated bandgaps in the following results. Another source of error is dependent upon increasing the number of plane waves so that the simulation converges on consistent frequency results. 81 plane waves were used in these simulations. Above this number, additional plane waves only decreased the difference between frequency solutions by < 0.15%.

The effective parameters are studied by varying a single parameter and keeping the other PPC parameters constant at a lattice constant of 1 mm, a plasma column radius of 0.45 mm, a plasma frequency of 300 GHz (corresponding to a plasma density of 10^{21} m^{-3}),[103] and a relative background permittivity of one. These values roughly correspond to the upper limit of experimental values for PPCs

formed by dielectric barrier discharge[35,42,56,103,45–52] and capillary discharge.[40,41,43,57] For simplicity, the collision frequency is assumed to be zero when calculating the plasma permittivity with Eq. 1.

3.2 Results

In most PPCs, uniform control of the plasma frequency is the conventional method for controlling the bandgaps. Manipulating a single discharge electric field, which addresses all plasma columns, is far simpler than individually controlling each plasma column. However, the range of frequencies and widths of the bandgap can be expanded using individually controlled plasma columns. As a baseline for comparison, the column plasma frequency of a PPC, with a fixed 1 mm lattice constant and a column radius of 0.45 mm, is varied from 0 to 300 GHz in FIG. 13. This demonstrates the range of bandgaps produced by a PPC with uniformly varied plasma columns. In the following subsections we explore the enhanced bandgap capabilities provided by locally individually controlled plasma columns and compare with the bandgap range of the baseline configuration of FIG. 13.

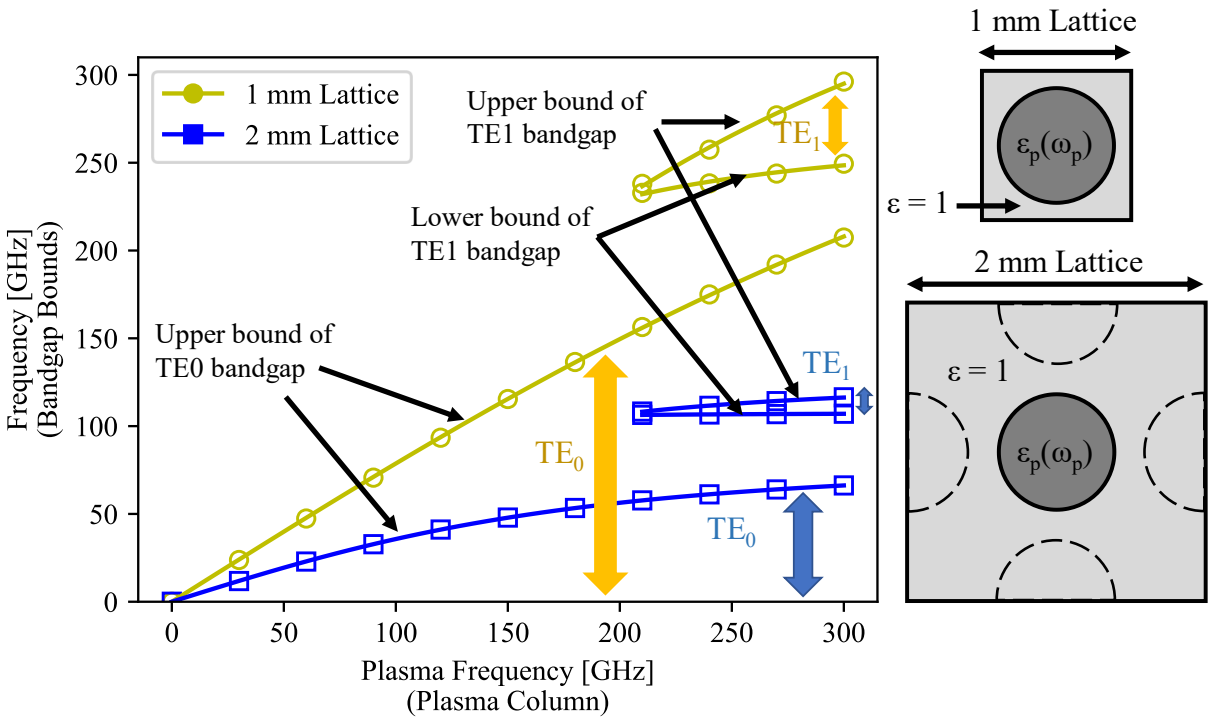

FIG. 13: Comparison between 1 mm lattice and 2 mm lattice constant with the column plasma frequency varied. The distributions with their respective dependent variables are presented to the right.

The curves of FIG. 13 define the limits to the TE_1 and TE_0 bandgaps as a function of plasma frequency. The lowest line of each data set defines the upper limit of the TE_0 bandgap, which extends from this limit down to zero. The upper two lines define the upper and lower limits of the TE_1 bandgap. The TE_1 bandgap does not extend the full range of the plasma, eventually cutting off at 210 GHz. As the plasma frequency decreases the plasma no longer blocks enough of the propagating wave and allows it to propagate within the plasma columns. To better compare trends, the PWE simulation results (markers) are curve fit (lines) with an inverse square root relation, characteristic of the relationship between the wave frequency and the plasma frequency from Eq. 1.[87]

3.2.1 Lattice Constant

The lattice constant is controlled by varying multiple plasma columns within a PPC. By turning off every other column in the PPC, as shown by FIG. 10, an initial lattice constant of 1 mm is converted to a lattice constant of 2 mm. This change is also shown in the permittivity distributions to the right of

FIG. 13, where the semi-circles of the 2 mm distribution depict where the individually controlled plasma columns of the PPC are turned off.

The bandgaps of the 1 mm and 2 mm lattice constant, presented in FIG. 13, show the improved range of the TE_1 bandgap when the lattice constant is adjustable. The TE_1 bandgap is adjustable in frequency from around 275 GHz (1 mm lattice constant) to 100 GHz (2 mm lattice constant). By changing the lattice constant with individual column control, the TE_1 bandgap is reduced in frequency, far below what is allowed by equally changing all the columns of the 1 mm PPC. The TE_0 range of the 2 mm lattice constant is four times smaller than the 1 mm lattice constant, and this is because the plasma distribution is more sparsely populated by plasma columns. There is a frequency region (125 GHz – 225 GHz) where neither the 1 mm nor 2 mm lattice constant configurations produce a TE_1 bandgap. The step sizes of the lattice constant are limited by the PPC's smallest lattice constant. For this PPC, the minimum step size is 1 mm and does not allow bandgaps in the 125 GHz – 225 GHz region using the lattice constant control method.

3.2.2 Super Radius

A super radius is formed by grouping plasma columns at the center of a supercell, as presented in FIG. 10. To implement this in a 1 mm lattice constant PPC, a 10x10 array of plasma columns have the center columns activated to form the super radius and the surrounding columns deactivated to form the spacing between the periodic clusters, as shown in FIG. 14. The super radius is defined by the circumscribed circle (red-dashed) around the cluster. The super radius is increased in FIG. 14 by activating more plasma columns to grow the cluster. The distance between the center of each cluster is a 10 mm lattice constant, an order of magnitude increase from the 1 mm baseline.

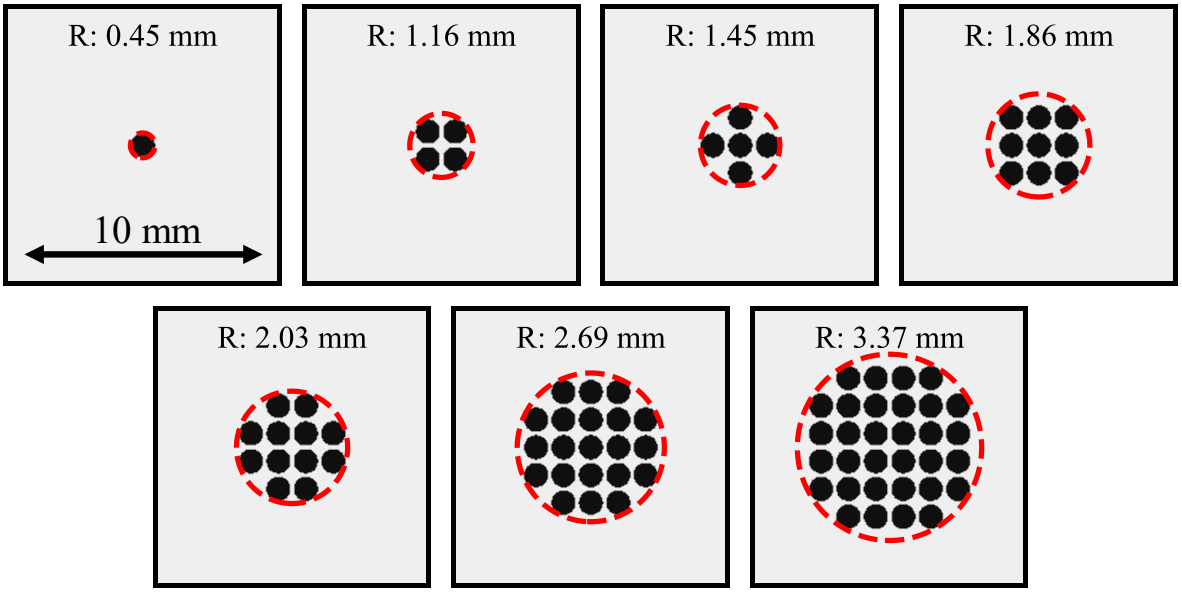

FIG. 14: Plasma columns can be grouped within a supercell to create a super radius. The lattice constant is the width of the supercell, 10 mm. Each distribution is labelled with its super radius (R), the outline of which is superscribed around the plasma column cluster.

The bandgaps formed by the super radius distributions of FIG. 14 are plotted in FIG. 15. The individual plasma columns have the baseline radius of 0.45 mm, lattice constant of 1 mm, and plasma frequency of 300 GHz. The super radius structure acts as a photonic crystal for wavelengths that are twice the 10 mm lattice constant. With wavelengths far larger than the 1 mm individual column separation, the incident wave sees the cluster as a uniform plasma. However, with this condition, the wave perceives the cluster plasma frequency as an area average of the individual plasma columns and surrounding free space, resulting in a 190 GHz effective plasma frequency for the super radius circle. For comparison, simulation results for a uniform plasma column with radius on the scale of the super radius and with the same effective plasma frequency (190 GHz) is also plotted in FIG. 15 (red curve). These results show that the super radius structure of clustered plasma columns provides bandgaps that are the same as a uniform plasma column with the same size and area-averaged plasma frequency. In other words, a super radius structure consisting of 300 GHz individual plasma columns appears analogous to a similarly-sized single uniform plasma column at 190 GHz.

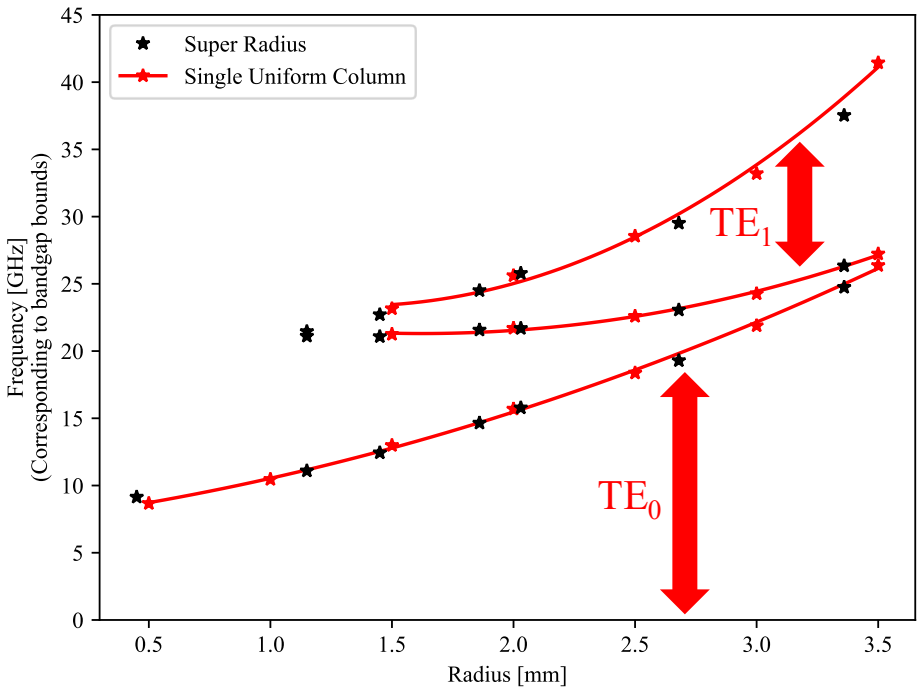

FIG. 15: Comparison of the super radius and uniform radius, simulations and curve fit of uniform column. The Super Radius is not curve fit since the construction of its radius is discreet.

The super radius structure enabled by individual localized plasma column control enables the TE_1 bandgap to form when the lattice constant is increased. With a fixed plasma structure this is not possible. The transition from a 1 mm to a 10 mm lattice constant decreases the frequency and increases the wavelength at which the PPC bandgaps form. With a fixed plasma structure, increasing the lattice constant to 10 mm means the individual plasma columns with a radius of only 0.45 mm occupy a much smaller portion of the unit cell area. This case of a 0.45 mm plasma column within a 10 mm lattice is represented by the 0.45 mm radius data point of FIG. 15. At this point there are no TE_1 bandgaps and only the TE_0 bandgap is present. With individually locally controlled plasma columns, a larger super radius structure can be created within the large 10 mm lattice structure and TE_1 bandgaps can be created. Specifically, when the super radius is created at or above 1.16 mm, the TE_1 bandgap appears and widens with increasing super radius. Using individual column control to form the super radius structure allows the baseline 1 mm lattice PPC to emulate a PPC ten times its size. Consequently, the TE_1 bandgap center

frequency is lowered by an order of magnitude: 275 GHz (FIG. 13) to 33 GHz (FIG. 15). The individual column control provides the capability to reduce the bandgap center frequency by an order of magnitude.

3.2.3 Effective Background Permittivity

The individual plasma column control enables change to the background permittivity by changing the plasma frequency of columns that would otherwise be turned off, as presented in FIG. 10. The resulting "effective background permittivity" is simulated with four plasma columns in a supercell, arranged in a square lattice structure, as shown in FIG. 16. The plasma column in the upper right corner of the supercell has a fixed plasma frequency of 300 GHz, while the plasma frequency of the other three columns varies in unison from 0 - 300 GHz. The extremes of this range are PPCs with 2 mm and 1 mm lattice constants and uniform background permittivity, respectively. Increasing the plasma frequency of the three surrounding columns makes a continuous transition between the two lattice constants.

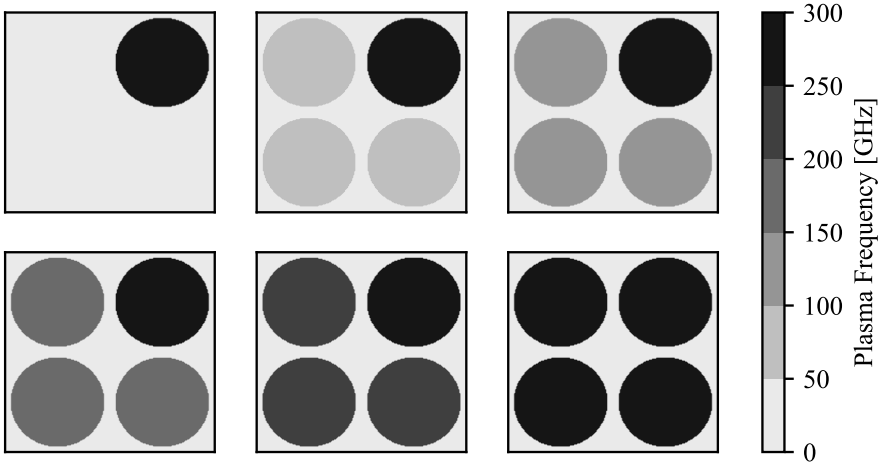

FIG. 16: Distribution of plasma frequency that creates an effective permittivity in the background of the 2 mm lattice structure. The surrounding columns at 0 GHz represent a 2 mm unit cell distribution, and the surrounding columns at 300 GHz represent a 1 mm unit cell distribution.

The transition between the bandgaps of the 2 mm and 1 mm lattice constants is presented in FIG. 17. For comparison, the 2 mm and 1 mm lattice constant data from FIG. 13 are also included in FIG. 17. In FIG. 13, the independent variable is the column plasma frequency, however this does not account for

the different cell and supercell areas of the 1 mm and 2 mm lattice constants. For FIG. 17, the "area-averaged plasma frequency" ($\omega_{p\ avg}$), defined by Eq. 16, is used to account for the change in plasma distribution across the unit cell. The sum of the column plasma frequency (ω_p) and column area (A_p) products are normalized by the total unit cell area ($A_{unit\ cell}$).

$$\omega_{p_{avg}} = \frac{\sum \omega_p A_p}{A_{unit\ cell}} \qquad \text{Eq. 16}$$

The TE_0 bandgap of all three data sets follow the same general trend near the unit line where the area-averaged plasma frequency equals the bandgap limit frequency. The agreement justifies using the area-averaged plasma frequency as the independent variable, since the TE_0 bandgap is a function of the bulk plasma frequency, as discussed in Section 3**Error! Reference source not found.**. The effective p ermittivity case matches identically to the 1 mm and 2 mm cases, at 190 GHz and 48 GHz plasma frequency, respectively, because this is where the effective permittivity plasma distribution from FIG. 16 matches the plasma distributions of FIG. 13.

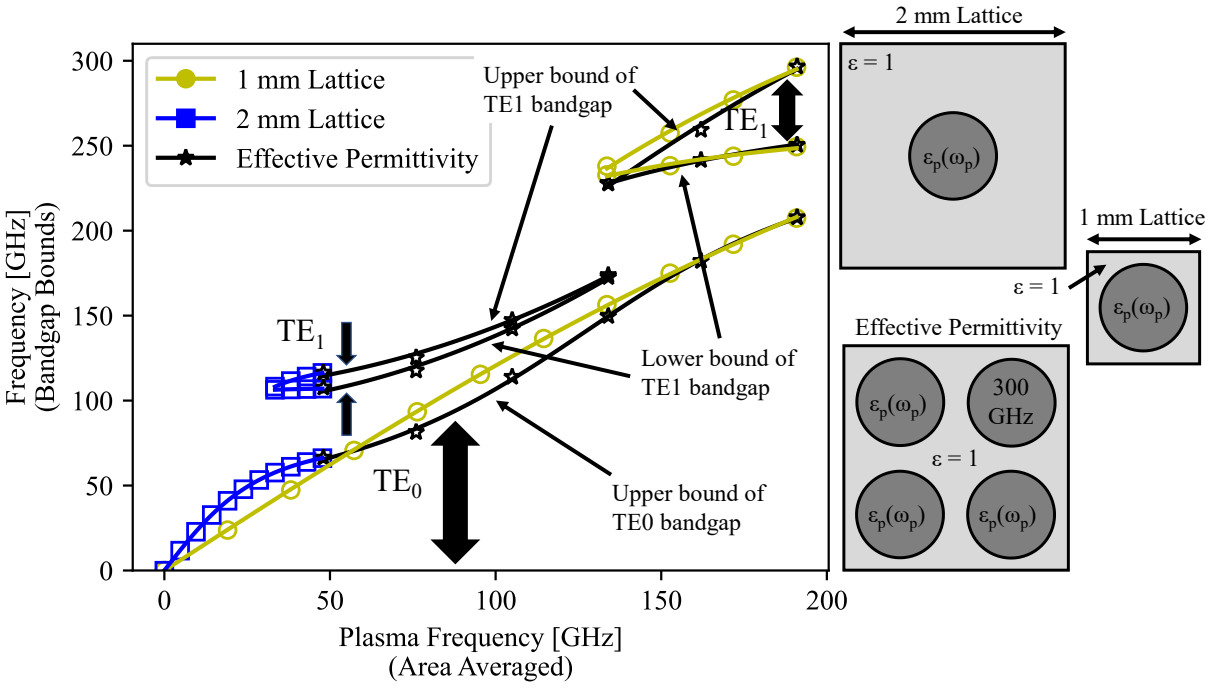

FIG. 17: Comparison between effective permittivity plasma variation, 1 mm lattice constant plasma variation, and 2 mm lattice constant plasma variation. The distributions with their respective dependent variables are presented to the right.

The effective permittivity approach partially bridges the frequency range between the 1 mm and 2 mm lattice constant TE_1 bandgaps. There is a discontinuity in the effective permittivity TE_1 bandgap data at 133 GHz. Above this point, the bandgap acts like the TE_1 bandgap of the 1 mm lattice constant, widening in width with increasing plasma frequency. Below this point, the bandgap acts like the TE_1 bandgap of a 2 mm lattice constant. However, this TE_1 bandgap increases in frequency with an increasing plasma frequency. This occurs because the increased plasma frequency decreases the permittivity of the three surrounding plasma columns, as defined by Eq. 1. The bandgap frequency then increases due to its inverse relationship to the permittivity, as defined by Eq. 5. In this way, individual column control provides the capability to form bandgaps between quantized step sizes of the lattice constants.

The bandgaps enabled by the effective permittivity approach can be compared to the bandgaps with a uniform background plasma approach. This comparison is shown in FIG. 18. The uniform background plasma distribution has a single plasma column of 300 GHz surrounded by a uniform background plasma with a plasma frequency varied from 0 - 300 GHz.

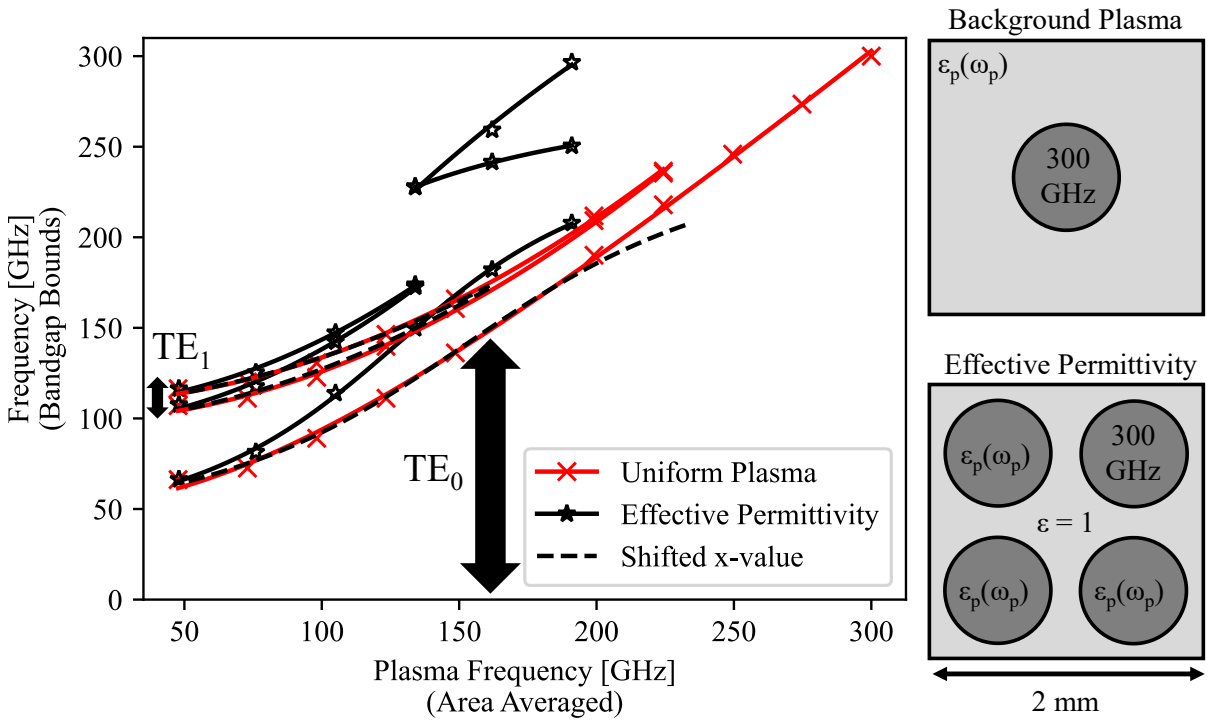

FIG. 18: Variation of the background plasma frequency as a uniform plasma compared with three plasma columns (effective permittivity). The dielectric distributions with their respective dependent variables are presented to the right.

FIG. 18 shows that the effective permittivity approach has similar trends to the uniform plasma, except the effective permittivity approach has a greater slope. The difference between the results can be quantified as a constant proportional shift of the bandgap data. The effective permittivity data are curve fit to the uniform plasma data by adjusting the dependent variable. The fit is a linear transformation, Eq. 17, of the effective permittivity plasma frequency (ω_p) to a shifted plasma frequency ($\omega_{p\ shifted}$). This is equivalent to adjusting the area-averaging multiplying factor. Eq. 17 is also applied to the TE_1 bandgap lower limit and the TE_0 bandgap upper limit, of the three-column data. Both show strong agreement up until the effective permittivity transitions from emulating a 2 mm lattice constant with background plasma, to emulating a 1 mm lattice constant, at 133 GHz plasma frequency. So, the difference in slope between the two approaches is associated with this transition. The individual column control increases the

bandgap center frequency by emulating a background of uniform plasma, which reduces the surrounding permittivity.

$$\omega_{p_{shifted}} = 1.27(\omega_p - 7.52) \quad \text{Eq. 17}$$

3.3 Discussion

The presented results demonstrate the increased tunability of PPC bandgaps with individually controlled plasma columns compared to a conventional spatially-fixed uniformly varied plasma PPC. The individually controlled plasma columns can be used to change the lattice constant, create an adjustable super radius, and an effective background permittivity, as presented in FIG. 10. A lattice constant increase lowers the bandgap frequency. The transition from a 1 mm to a 2 mm lattice constant more than halves the TE_1 bandgap frequency, as shown in FIG. 13. However, this leaves a range of ~200 GHz where no TE_1 bandgaps exist, and a uniformly varied PPC cannot be adjusted to provide a TE_1 bandgap. The effective permittivity approach enabled by individually controlled plasma columns can increase the bandgap frequency across half of the ~200 GHz range, as shown in FIG. 17. A further increase of the lattice constant to 10 mm will proportionately reduce the bandgap center frequency, as shown in FIG. 15. However, the bandgap is only maintained at the lower frequencies by using a super radius structure composed of a cluster of plasma columns. The bandgap bandwidth is then adjustable by changing the super radius size. These approaches work because the wave perceives the structures as an area average over the wavelength so that the pixelated structure appears uniform to the wave.

Each additional effective parameter improves the range of the bandgap's frequency and bandwidth from that of the baseline fixed PPC (1 mm lattice constant). FIG. 19 shows the capability space (bandgap center frequency and associated bandwidths) of the simulated bandgaps for the effective parameters. The TE_0 bandgaps all lie along the same line since the center frequency is half of the upper TE_0 limit when the lower limit is zero. The maximum and minimum TE_0 bandgaps are achieved with the maximum and minimum plasma density distributions. These are both produced by the baseline. So, the effective parameters do not increase the range of possible TE_0 bandgaps. However, the additional

parameters do improve the control over the TE_0 bandgap so that the TE_0 can be reduced without eliminating the TE_1 bandgap, as demonstrated in FIG. 13 and FIG. 15.

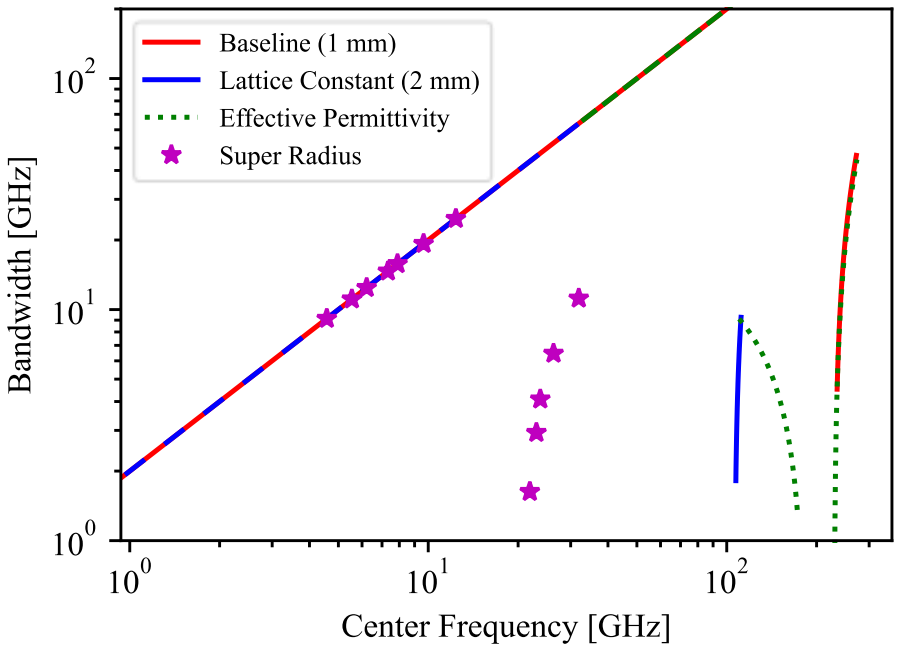

FIG. 19: Bandgap capability frequency space with each additional effective parameter. All TE0 bandgaps fall along the same diagonal line. All other data points are TE1 bandgaps.

The set of TE_1 bandgaps, in FIG. 19, show how the different effective parameters can control the bandgap center frequency. The effective parameters eliminate any lower frequency limit on the TE_1 bandgap. The purely plasma controlled PPC of the 1 mm lattice constant cannot be formed below 2 GHz, but doubling the lattice constant (lattice constant - 2 mm data) reduces the center frequency by a half. Increasing lattice constant by a factor of 10 (super radius data) reduces the center frequency by an order of magnitude. The permittivity and lattice constant primarily control the center frequency, while the plasma frequency and radius primarily control the bandwidth.

These effective parameters do not each require separate physical control mechanisms, but rather rely on the same individual column control to manipulate all aspects of the PPC. With this control method, each additional effective parameter adds another level of control over the bandgap without removing the other parameter controls. Since only a single parameter was varied at a time with the

simulated bandgaps, the bandgaps presented in FIG. 19 only represent a fraction of the possible tuning range.

Although this work focused on producing large columns from smaller columns, the ability to apply plasma as pixels in a larger structure opens up the possibility of more interesting structures.[60,104,105] The design can go beyond photonic crystals to create metamaterial, such as split ring resonators[106] and thin wire structures.[37] In a 2D plasma column structure, the split rings could be formed by rings of columns[105] and the wires formed by rows of plasma columns. Metamaterials have periodicities less than 1/5 the intended wavelength, ensuring the area averaging effect will make the pixilated plasma structures appear continuous to the incident wavelength. A metamaterial with a fully variable 2D structure could be formed to allow for both tuning of the magnetic and electric elements. Control over the permeability and permittivity then leads to frequency control of a fixed negative index of refraction, or control of negative index of refraction for a fixed frequency.

3.4 Conclusion

An individually controllable plasma column PPC with a changeable lattice constant, super radius, and effective permittivity are simulated to demonstrate their effect on the range of bandgap widths and frequencies. The bandgap simulations, using a PWE method, demonstrate increased frequency variability compared with a baseline uniformly varied plasma column PPC. The lattice constant produces lower frequency bandgaps. The super radius widens the bandgap and maintains the presence of the bandgap at lattice constants 10 times the baseline PPC lattice constant. The effective background permittivity replicates a background of uniform plasma and tunes the bandgaps between integer step sizes of the lattice constant. The primary reason for the performance of these effective parameters is the area-averaging effect of the pixelated plasma columns by a wavelength larger than the PPC structure.

The individual plasma column control provides a single physical tuning parameter that addresses all the parameters which define a PPC. The effective parameters allow more flexibility in the choice of plasma discharge when engineering a tunable PPC. A filamentary plasma PPC can produce periodic

elements with effective radius far larger than the radius of the individual filaments, allowing them to produce bandgaps at lower frequencies. The area-average effect also suggests a path forward for making more complex photonic crystals and metamaterials out of pixelated structures.

4 Experimental Single Filament Control

This work demonstrates an approach for achieving filament control by influencing the dynamics of the filament formation. Once a streamer is established across the gas gap, plasma acts as a highly conductive path for the electrons to transfer charge between the two dielectrics.[107,108] Surface charge then builds up on the dielectric in a Gaussian distribution until the applied electric field falls below the breakdown limit and extinguishes the filament.[109] Residual space and surface charge enhance the electric field during the reversed polarity of the driving voltage, causing a repeat discharge at the same location.[110] This work demonstrates the control of a single filament's light intensity, which is proportional to the electron density,[111] by influencing the charge distribution in the DBD, using a single electrode in an effective array of electrodes.

The intended application of filament control through charge distribution by individual electrodes is to form an array of electrodes behind a dielectric that controls each filament position and permittivity by manipulating the charge distribution over the entire dielectric. The relative voltage differences between individual needle electrodes would govern the position while the overall driving voltage would determine the permittivity of the filaments. This approach would uncouple the two main metamaterial parameters: filament permittivity and filament distribution. By only manipulating voltage differences at magnitudes necessary to induce charge distribution, rather than at magnitudes necessary for breakdown voltage, the electrode arrays could be more manageable for control circuits. The control method would remain purely electrical and tunable, extend the range of parameter variation, and allow the direct implementation of simulated PPC structures.

To demonstrate charge distribution control of a filament, Section 4 **Error! Reference source not found.** and 4.2 describe the experimental setup and results from light intensity variation of a single filament within an array of filaments. A resistively biased needle controls the change in light intensity from the filament up until the filament no longer discharges. The surrounding array of filaments is formed by a mesh electrode to allow alternate current paths. Current, voltage, and light intensity data are

presented as evidence that the voltage variations are magnitudes less than what would be necessary to reduce the cross gap voltage below the electric strength of air. Charge redistribution rather than the cross gap voltage difference is concluded as the mechanism through which the needle controls the filament light intensity and eventually extinguishes the filament.

4.1 Experimental Setup

The DBD investigated in this work consists of two parallel copper mesh electrodes, both covered with microscope slide glass. The driving signal mesh electrode allows for end-on photos of the filament position across the surface of the dielectric. The mesh and dielectric barrier that make up the driving electrode are of dimensions that create a uniform charge distribution over the discharging surface: 0.15 mm opening (#100 mesh size), 0.056 mm wire diameter, and 1.0 mm thick dielectric.[112,113] The grounded mesh electrode has an opening of 0.85 mm (#20 mesh size), a 0.40 mm diameter wire, and a dielectric barrier thickness of 0.12 mm. The larger mesh size and thinner dielectric barrier are sufficient to create an electric field on the surface of the grounded dielectric barrier, causing filaments to preferentially discharge at the mesh nodes. The vertical and horizontal weaves of the grounded electrode have an amplitude difference in their sinusoidal paths that keep the vertical weave 0.12 mm away from the glass surface at the mesh nodes where the wires cross. The peak-to-peak sinusoidal amplitude of the horizontal wire weave is 0.92 mm and that of the vertical wire weave is 0.68 mm.

The DBD mount, an acrylonitrile butadiene styrene (ABS) plastic stand, has acme screws on the side to permit fine tuning of the gap width. The effective discharging sur-face area of the DBD is 22 mm 22 mm. Adhesive gel on the edge of the mesh prevents charge from making a direct path to the mesh electrodes around the edge of the dielectric. This ensures that the current travels through the dielectric. When the DBD operates at 6.5 kV and 7.5 kV, the air gap is 1.0 mm wide, and when it operates at 9.0 kV, the air gap is 1.5 mm wide. For all conditions, the frequency is 3.2 kHz.

An independently biased needle controls the light intensity of a plasma filament within the DBD. A magnetic wire with flattened tip mounted flush to the back surface of the grounded dielectric barrier

forms the needle. The wire (diameter 0.57 mm) with an added Kapton insulation layer (0.14 mm thickness, $\varepsilon = 3.5$) fits through the mesh, so that the only electrical connections between the two are through the dielectric or their respective biasing connections to ground. Resistors connect the needle to ground, causing the needle to have a non-zero, or self-biasing, voltage. Changing resistance adjusts the self-biasing voltage of the needle.

FIG. 20 shows the electrical and instrumental schematic of the experimental setup. The driving voltage signal is created by a Rigol DG-1022 Function Generator. The power for the discharge is supplied by a Crown Macro-Tech 1202 Audio Amplifier. A Corona Magnetics 5525–2 Transformer with a turn ratio of 1:357 increases the signal to the driving voltage. A North Star PVM-5 High Voltage Probe, with a 1:1000 ratio, monitors the voltage supplied to the DBD. A 1:1 Pearson Current Probe, Model 114, monitors the total current through the system. A 1:10 Tektronix P2221 passive voltage probe reads the voltage across a 200 kΩ resistor in series with the larger biasing resistor that controls the voltage at the needle. An Agilent Infinium 500 MHz 1GSa/s Model #54815A oscilloscope records both the Pearson and the North Star probe signals. A Canon EOS Rebel XL records the time-averaged discharge of the filament position and light intensity at an exposure time of 125 ms.

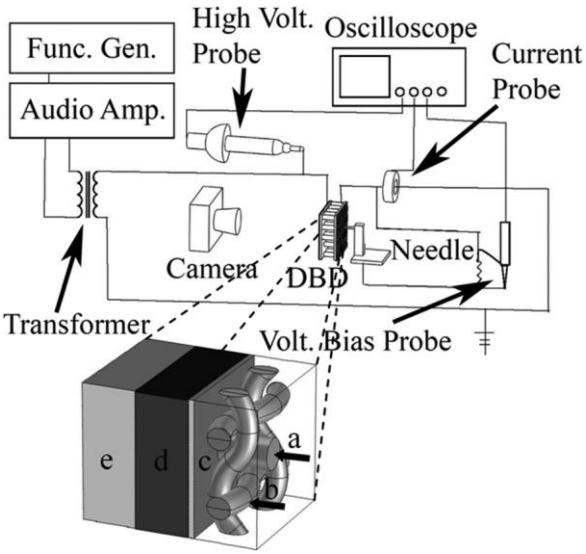

FIG. 20. Diagram of the experimental setup with the solid model inset showing the needle location with respect to mesh nodes. The solid model shows the DBD layers consisting of (a) needle electrode, (b) grounded wire mesh and mesh node (where weaves cross), (c) 0.12 mm thick glass dielectric, (d) 1.0 mm air gap, and (e) 1.0 mm thick glass dielectric.

4.2 Experimental Results

4.2.1 Filament Photographs

Photographs of the DBD filaments for different self-biasing needle resistances are shown in FIG. 21. These data are for the 6.5 kV driving voltage. The light from each discharge cycle was collected over the total camera exposure time of 125 ms creating a time integration of 875 filament discharges per data point. Only the lowest quarter of the digital photos' histograms were populated, signifying that none of the photocells in the camera were over saturated. The regular pattern of dots is made up of individual DBD plasma filaments forming where the grounded wire mesh electrode contacts the dielectric. The filaments form at alternating mesh nodes due to the height difference between the vertical and horizontal weaves. For resistances below 10 MΩ, a filament clearly forms in between the wire mesh nodes at the needle location. As the self-biasing resistance of the needle increases, the filament light intensity decreases. It is clear from these photographs that the independent needle can control both the presence and intensity of the new filament. Resistance below 200 kΩ was investigated with a 1 kΩ resistor; however, prominent current spikes reduced the reliability of the measurements. Resistances above 30 MΩ

were not investigated because the data showed that further increases had no effect on the discharge of the filament.

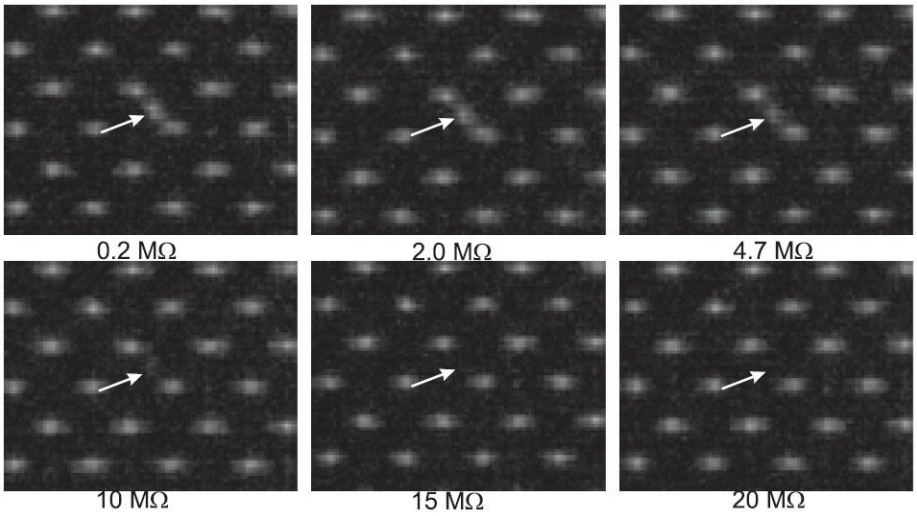

FIG. 21. Photographs of the filament at the needle within the mesh filament array. End on view of the dielectric surface with the DBD driving voltage operating at 6.5 kV. The resistances between the needle and ground are given. The arrow indicates the needle filament position.

The needle filament position is always in the same location, to within ~3%. The needle filament position is calculated based on the light intensity from the photos and compared with the diagonal line between the two adjacent wire mesh filaments. Along the diagonal, the needle filament position varies by 3% (~0.05 mm) from the midpoint between the adjacent filaments. Perpendicular to the diagonal, the needle filament position varies by less than 1% (~0.018 mm). These measures provide a level of confidence to this method.

A photographic analysis is presented in order to obtain a better measure of the light intensity change at the needle-controlled filament. The average numerical value of the photograph pixels at the needle-controlled filament location is compared with the average pixel value at a reference mesh filament located three filaments away from the needle. An 8 × 8 pixel square section of the photograph, fitting the size of the filament, was selected using Photoshop software. The average background pixel value, taken from the mid-point between two mesh filaments, was subtracted from the filament pixel value. A 15 × 15 pixel square section was used to select the region without any discharge. In this way, the intensity of the

needle-controlled filament is compared with a mesh filament. FIG. 22 shows the results as the ratio of the needle filament to the mesh filament for 6.5 kV, 7.5 kV, and 9.0 kV. The error bars were created by measuring the light intensity of the same ten mesh filaments surrounding the needle location and its immediately adjacent mesh filaments, taking the standard deviation between photos, averaging that value, and creating a ratio with respect to the reference filament intensity.

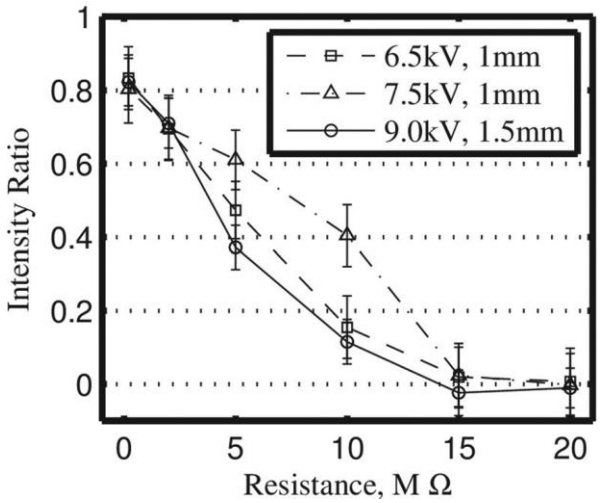

FIG. 22. Light intensity as a function of resistance at 6.5 kV, 7.5 kV, and 9.0 kV. Light intensity at the needle position as a ratio to a mesh node filament. (Lines are used for clarity.)

The needle-controlled filament has a distinct on and off state. For resistances at 15 MΩ and above, the ratio of the needle-filament to the mesh-filament goes to zero, signifying that the light intensity is the same as a non-discharging region. At this point, the ratio of the needle filament to the mesh is zero since the background is subtracted from the needle value. Assuming that there is no discharge in the mesh gap, this ratio signifies that no discharge occurs at the needle's position. The measured luminosity in the regions without filaments is due to ambient light and the inherent noise level of the camera.

As the resistance decreases, the needle-filament turns on and becomes more intense. At the lowest resistance tested (200 kΩ), the needle-filament has an intensity that remains at 80% of the mesh-filament intensity for 6.5 kV, 7.5 kV, and 9.0 kV, which is still less than the surrounding node filaments. Since the needle filament has two immediately adjacent mesh-filaments that are half the average filament separation distance away, the needle-filament competes for surface charge with these adjacent filaments.

A comparison between the needle filament and the adjacent filaments shows that they have a 1:1 ratio at 200 kΩ. If the needle filament was equally separated from the surrounding filaments, its expected ratio would be 1:1 at 200 kΩ.

Although the intensity values of all three driving voltages are within the significant error limits for 200 kΩ, 2 MΩ, and most significantly the turn off resistance 15 MΩ, the 7.5 kV condition deviates by 160% at 10 MΩ and 30% at 4.7 MΩ, from the 6.5 kV condition. The wire of the mesh that curves away from the back of the dielectric can support additional charge on the dielectric surface within the gas gap contributing to the filament characteristic surface charge.[114] Visually, discharge activity in the photos of the 7.5 kV condition covers an increased surface area along the wire mesh in comparison to the 6.5 kV and 9.0 kV photos. The additional charge, for 4.7 MΩ and 10 MΩ, could offset the charge siphoned from the needle filament to the adjacent filaments. The gas gap for the 9.0 kV condition is 1.5 mm instead of 1.0 mm, which prevents over saturation on the dielectric sur-face along the wire. However, there is a dynamic that overcomes this additional charge at 15 MΩ, since all filaments have significantly the same intensity for this resistance.

4.2.2 Needle Voltage and Current

Finally, FIG. 22 shows that the intensity ratio is almost the same for all applied voltages, within the error bars except for the 10 MΩ case. This is to be expected when one considers that filament light intensity is correlated with the needle and driving voltages (electric fields), and that the needle voltage changes correspondingly with the driving voltage. The needle voltage is shown in FIG. 23. For the same needle bias resistance, the needle voltage increases corresponding with the increase in driving voltage. For example when the driving voltage increases 15% from 6.5 to 7.5 kV, at 5 MΩ the needle voltage increases 15% from 209 to 238 V, at 2 MΩ the increase is 15% from 97 to 113 V. Light intensity of plasma filament formation and propagation in air is proportional to the ionization activity, which is related to the bias voltage and corresponding electric field.[115–117] As driving voltage increases, needle voltage increases proportionally, and filament intensity increases by about the same amount at both the

needle and wire mesh locations such that the ratio of filament intensity is only weakly dependent on the driving voltage, as shown in FIG. 22.

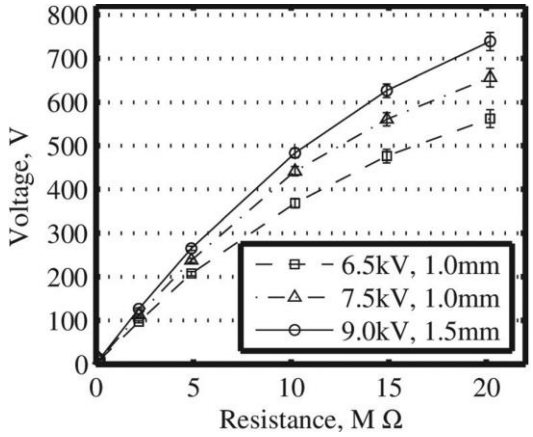

FIG. 23. Voltage as a function of resistance at 6.5, 7.5, and 9.5 kV. Changes to the needle's voltage due to changing resistors between the needle and ground.

Adjusting the needle self-biasing resistance affects the needle voltage and current. The voltage at the needle does not rise linearly, as it curves with increased resistance, as shown in FIG. 23. Although the voltage looks like it might approach a limit, the point of interest where the needle filament ceases to discharge is met before any definitive evidence of a limit develops from increased resistance. The voltage for the turn off of the filament at the needle is 476 V, 560 V, and 626 V respective to the driving voltages 6.5 kV, 7.5 kV, and 9.0 kV. All of these values correspond to 7% of the driving voltage. The difference between the observed on and off state, 10 MΩ to 15 MΩ, is 108 V, 119 V, and 143 V respective to the driving voltages 6.5 kV, 7.5 kV, and 9.0 kV.

The external voltage suppression caused by the biasing resistor at the 7.5 kV driving voltage is not large enough to bring the voltage difference across the air gap to the voltage difference of the 6.5 kV driving discharge. This implies that the intensity variation is not purely a result of reducing the voltage difference across the air gap, but rather preferential discharge at peak charge locations on the dielectric. In other words, more complex surface charge dynamics are responsible for these results rather than just the magnitude of the voltage difference across the air gap located at the needle.

The current through the needle is shown in FIG. 24. The current decreases linearly with the resistance. Although light intensity shows that there is no longer a filament forming at the needle, current continues to pass through the needle. The current drop between 200 kΩ and 15 MΩ remains the same for all driving voltages. The amperage offset suggests a uniform current that passes through all fully formed filaments. Since the current drop is only about a 27% decrease, the amount of charge forming over the needle on the dielectric must also remain of the same magnitude. With the voltage difference across the gap changing by only 7% and a current drop of only 27%, the electric field across the DBD must be displaced by an alternate charge movement mechanism in order to prevent breakdown of the air and formation of a plasma filament.

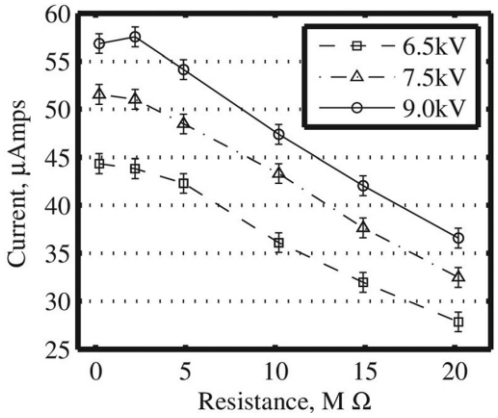

FIG. 24. Current as a function of resistance at 6.5, 7.5, and 9.5 kV. Changes to needle's current due to changing resistors between the needle and ground.

4.3 Conclusion: Single Needle Bias Voltage Control

The data presented above demonstrate the capability of a non-driving voltage bias applied to an individual electrode to vary the intensity of, and to turn off, a single filament, while adjacent to other discharging filaments in a DBD. The light intensity of the filament ranges between 80% and 0% of the surrounding filaments' intensities, and is representative of the plasma density. Peak voltages of 476 V and 560 V respective to the 6.5 kV and 7.5 kV driving voltages are required to transition the filament from full-on to full-off; however, lesser voltage changes of 100 V can cause the observed transition between a discharging filament and no filament. This small voltage change, relative to the driving voltage, keeps the

voltage difference applied across the gas gap above the breakdown voltage for air. The presence of the needle filament is then dependent on charge distribution caused by voltage differences between low voltage electrodes, rather than the total voltage difference across the gas gap. Voltage variations that control the presence of a single filament in a PPC are reduced to less than 7% of the independent driving voltage.

5 Simulation of Single Filament Electric

In the following Section, electromagnetic field simulations are presented within a DBD illustrating the effect of the biased voltage electrode on changes in the longitudinal and transverse electric field structure, as well as the change in free surface charge. Simulations show that indeed redistribution of surface charge controls the presence and intensity of the plasma filament, and the results suggest a design methodology for achieving continuously tunable filament permittivity and position control.

5.1 Simulation Setup

The simulations presented below were designed to replicate the experimental conditions of our previous work.[100,118] The experimental setup of the previous work was a DBD operated at 6.5 kV and 7.5 kV with 1.0 mm air gap and operated at 9.0 kV with 1.5 mm air gap. For all conditions, the frequency was 3.2 kHz. The driving voltage waveform was applied between two parallel electrodes covered with glass dielectric. The high-voltage electrode was uniform and covered with 1.0 mm thick dielectric, while the grounded electrode was wire mesh and covered with a 0.1 mm thick dielectric. Additionally, a needle electrode was inserted through the grounded wire mesh. A resistive bias was applied between the needle electrode and ground to adjust its electric potential. The resistive bias was varied to be 0.2, 2, 5, 10, and 15 MΩ. End-on photographs were captured of the filamentary DBD discharge revealing filaments where the grounded mesh made contact with the dielectric and at the needle electrode location. Results also indicated that the light intensity of the needle electrode plasma filament could be controlled by the resistive bias. As the resistance increased, the electric potential of the needle increased, and the corresponding plasma filament light intensity decreased until a measurable light intensity could no longer be detected. We refer to this condition when a measurable light intensity from the needle electrode filament was no longer detected as the “turnoff” condition. The turnoff condition was determined to be the 15 MΩ resistor case for all driving voltages.

Our goal here is to study changes in the electric field within the DBD gap due to the varied needle potential, and correlate those changes with variations in the needle filament light intensity and the

corresponding turnoff condition. The commercial software Computer Simulations Technologies (CST) Electromagnetic Studios[119] was used to simulate the electric fields within the DBD. This finite element software solves a range of electromagnetic problems. The solver selected for this simulation was the Low Frequency (LF) Domain solver with the electroquasistatic equations (Eq. 18 – Eq. 20).[120] The peak voltage boundary conditions are substituted for the electric field using Eq. 21[121] and the spatially discretized equations are solved for the electric field and current densities. These equations ignore the magnetic induction and depend on the source at a single instant in time without regard to the fields at the previous instant in time. In this case, an electrostatic description of the field is obtained for the maximum field values. The solver selection is valid since the problem is dominated by the electric field if the frequency was brought to a static state and since the ratio of the characteristic size to the applied field wavelength is much less than one ($10^{8} << 1$).

$$\nabla \cdot E = \frac{\rho}{\varepsilon_o} \qquad \text{Eq. 18}$$

$$\nabla \times E = 0 \qquad \text{Eq. 19}$$

$$\nabla \cdot J + i\omega\rho = 0 \qquad \text{Eq. 20}$$

$$E = -\nabla\phi \qquad \text{Eq. 21}$$

Although the simulation assumes (1) no free charge movement within the air gap, and (2) that the filament formation process displaces the field during discharge, the electrostatic results provide an understanding of the initially applied field that must be displaced during discharge. In other words, the electrostatic results elucidate the vacuum fields that are present as the filament forms. These vacuum fields guide the electron motion and subsequent energy gain that leads to the gas breakdown and filament formation. Since the formation of the filament occurs over ~200 ns,[122] the applied electric field, with a 312.5 μs period (3.2 kHz), was considered constant during the filament formation process. Section 5.5.2. correlates changes in the simulated electric field (due to different needle bias) with changes in the

experimentally measured filament light intensity. In the context of charged particle movement, the field simulations can explain the observed filament intensity variation.

The 3D model was created using the CST in-house computer-aided design (CAD) software. The wire mesh of the model, shown in FIG. 25, replicates an inherent height difference between lateral and horizontal weaves. When placed against the surface of the dielectric, the wire closest to the surface creates the lowest potential drop so that only two of the four adjacent mesh nodes form filaments. The model contains a cylindrical electrode placed through the mesh to simulate the needle electrode. The end of the cylinder is flush with the dielectric replicating the physical assembly.

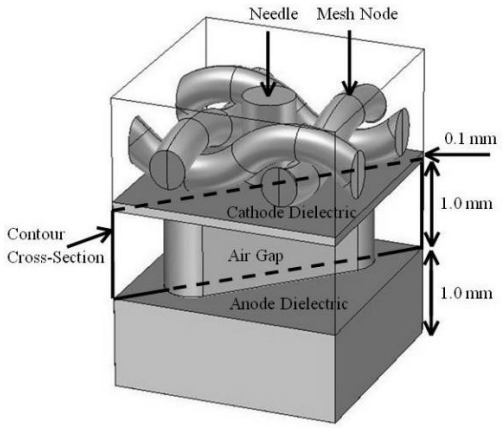

FIG. 25. Isometric view of the 3D CST model. The oval volume in the "air gap" defines a section of refined simulation mesh where the filaments form. The remaining air gap volume is not shown for clarity. The "contour cross-section" defines the plane over which the fields are analyzed.

The potential boundary conditions consisted of (1) a zero voltage applied to the mesh (cathode electrode), (2) the maximum driving voltage applied to the external surface of the 1.0 mm dielectric (anode electrode), and (3) the measured needle voltage applied to the cylindrical needle electrode. The boundary conditions perpendicular to the dielectric sur-face allowed only tangential electric fields. Behind the needle and mesh was an open boundary, located 0.5 mm away from the solid model. The materials chosen for the simulation came from the CST library: the dielectrics were lossy glass pyrex (ε =

4.87), the discharge gas gap was air ($\varepsilon = 1.00059$), and the conducting needle and mesh were perfect electrical conductors.

The voltage boundary conditions in the simulation correspond to the maximum measured value of the driving anode voltage and biased needle voltage. Specifically, simulations were completed for maximum driving voltages applied to the anode electrode of 6.5 and 7.5 kV. The 9.0 kV case was not simulated. The needle voltages were 9, 96, 207, 368, and 476 V for the 6.5 kV case and 10, 115, 230, 435, and 555 for the 7.5 kV case, corresponding with the resistive biases of 0.2, 2, 5, 10, and 15 MΩ, respectively. Results for the 6.5 and 7.5 kV cases show identical trends, with changes in the electric field directly proportional to the change in voltage. Therefore, only the 6.5 kV results are reported below. Since the magnitudes of the fields change proportionally with the driving voltage, a trend and analysis can still be performed to find the relevant field characteristics that affect the variation of the needle plasma filament light intensity.

5.2 Results

5.2.1 Longitudinal Electric Field

The contour map of the longitudinal electric field (normal to the dielectric), over the cross-section outlined in FIG. 25, is shown in FIG. 26. These contour plots display the general form of the electric field for the fully active needle filament (0.2 MΩ) and for no visible evidence of a filament (15 MΩ).

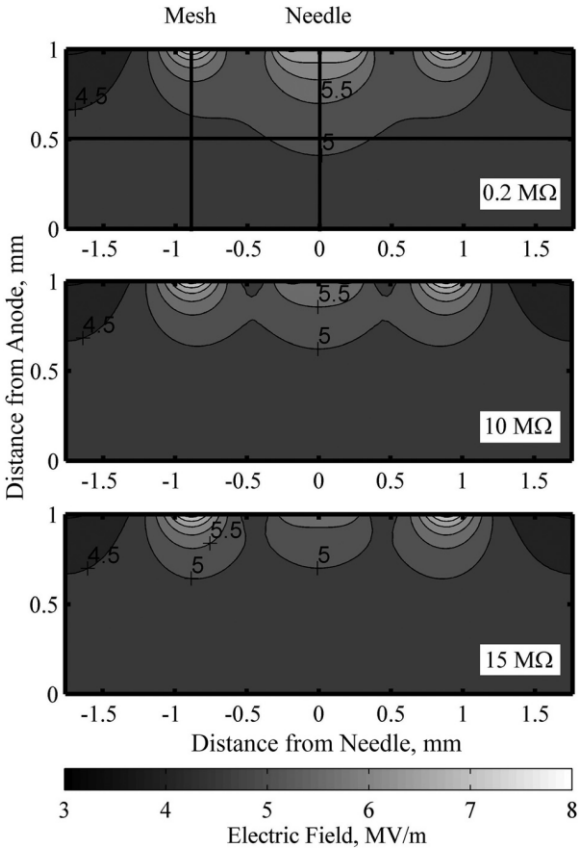

FIG. 26. Contour of longitudinal electric field. Three of the five needle bias conditions are presented: 0.2 MΩ, 10 MΩ, and 15 MΩ. The needle filament turn off occurs between 10 MΩ and 15 MΩ. The vertical lines in the 0.2 MΩ plot define the filament center axes along which the longitudinal fields in FIG. 27 are analyzed. The horizontal lines at 0 mm, 0.5 mm, and 1 mm from the anode (along the vertical axis) define the lines along which the transverse fields in FIG. 29 are analyzed.

The fields along the needle and mesh filament centerlines, defined by the vertical lines in FIG. 26, are shown in FIG. 27 at 0.2 MΩ and 15 MΩ. The mesh field near the cathode dielectric surface is at least 11% greater than the needle for all conditions due to the geometric difference between the needle and mesh. The curvature of the mesh wire creates a concentration of the electric field on the cathode dielectric surface, compared with the flat surface of the needle. However, the larger contact surface area of the needle maintains the concentration of the field at a further distance from the cathode. At 15 MΩ, the voltage bias offsets the electric field of the needle, lowering the field at the cathode, which reduces the field concentration at a distance.

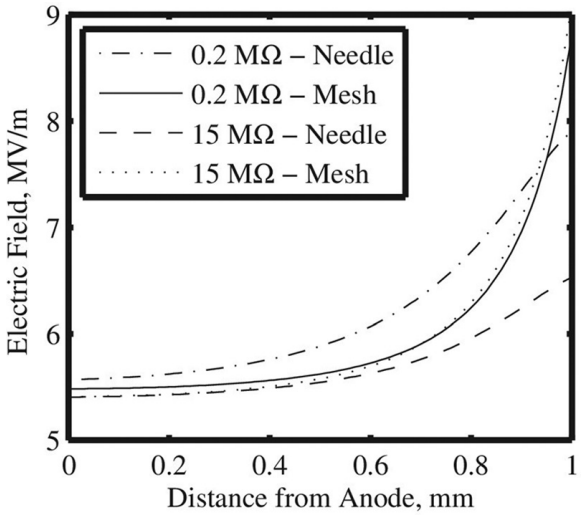

FIG. 27. Longitudinal electric field lines at the needle and mesh, for 0.2MΩ and 15MΩ. The longitudinal fields across the air gap show that the needle field is always less than the mesh for the 15 MΩ when the needle filament turns off.

The difference between the needle and mesh fields ($\Delta E(x)_{long} = \Delta E(x)_{long\ needle} - \Delta E(x)_{long\ mesh}$) is shown in FIG. 28, to illustrate this transition. All the bias conditions become positive at some position near the anode, except the 15 MΩ condition. They also all approach zero near the anode, with the 15 MΩ condition having a zero difference at the anode. The second derivative of the curve is negative for the 15 MΩ condition and is positive for the other conditions. For the filament turn off condition (15 MΩ), both the needle and mesh apply the same amount of longitudinal force on a unit of charge at the dielectric anode, but everywhere else the needle applies a lesser cross-gap force than the mesh.

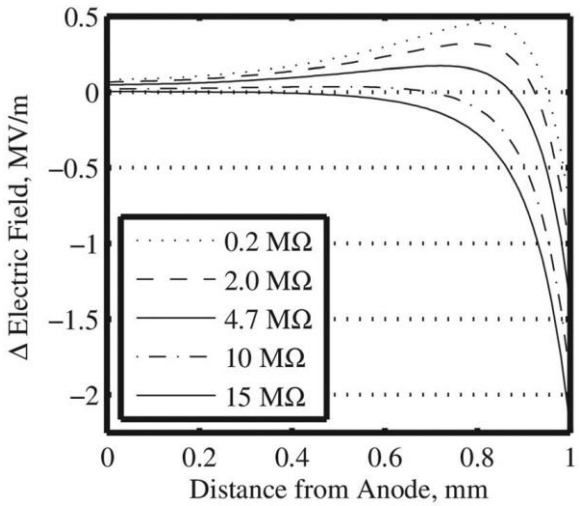

FIG. 28. Difference between needle and mesh longitudinal electric fields. The fields are plotted across the air gap from the anode dielectric (z = 0 mm) to the cathode dielectric (z = 1 mm).

5.2.2 Transverse Electric Field

The transverse field moves free charges toward or away from the filament locations. The transverse fields, along the horizontal lines shown in FIG. 26 at 0.0 mm, 0.5 mm, and 1.0 mm from the anode, are plotted in FIG. 29 for 0.2 MΩ–15 MΩ conditions. Transverse fields along the anode dielectric (0.0 mm), cathode dielectric (1.0 mm), and at the midplane (0.5 mm) are shown. The vertical lines in FIG. 29 correspond to the needle location at 0 mm and the mesh node at – 0.9 mm. Another mesh node is also present at +0.9 mm. These plots illustrate the electric force on a charge between the needle and mesh locations (parallel to the dielectric). It is clear that the transverse fields are strongest at the cathode dielectric, and decrease as one moves toward the anode. This is expected because the anode is biased uniformly (minimal transverse variation in potential), while the cathode has the mesh and needle electrodes which are biased differently (giving rise to strong transverse variation in potential). On the cathode dielectric, the transverse field between the needle and mesh has two peaks, one positive and one negative. The positive peak (near the needle) is the smallest at 15 MΩ due to the decreased voltage difference between the needle and the anode. The negative peak (near the mesh) increases in magnitude (becoming more negative) as needle resistance increases because the corresponding increase in needle voltage creates a stronger potential gradient along the transverse axis. Without the presence of the anode

potential, the trans-verse electric field would purely be directed from the needle towards the mesh with the largest value at 15 MΩ. But due to the presence of the high voltage anode, a transverse potential gradient forms (due to the needle and anode potential difference) creating transverse field directed towards the needle.

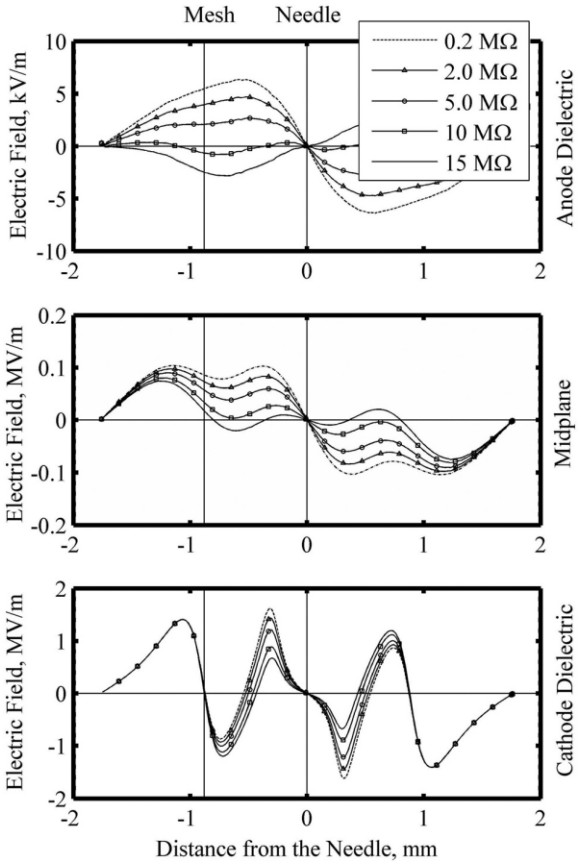

FIG. 29. Transverse electric field as a function of transverse position. The lines that define the transverse positions are parallel to the dielectric surface and intersect both mesh and needle filament locations, as shown in FIG. 26. The three figures represent different cross-sectional planes across the air gap (cathode dielectric surface, midplane across the air gap, and the anode dielectric surface).

At the anode dielectric, we see an interesting trend at the needle location. For 0.2 MΩ–10 MΩ, the transverse electric field profile has a negative slope that crosses zero at the needle location, but switches to a positive slope for the 15 MΩ condition (when the needle filament turns off). A negative slope prevents charge from building up at the needle location because an electron to the left (right) of the

needle will experience a force to the left (right), moving charge away from the needle location, preserving the longitudinal field, and enabling the filament to form. However, for the 15 MΩ case, the transverse field profile switches to a positive slope crossing zero and the opposite effect occurs. An electron to the left (right) of the needle will experience a force to the right (left), causing electrons to build-up at the needle location, reducing the applied field, and preventing a filament from forming.

5.2.3 Free Surface Charge Limitation

The charge density [C/m^2] on the dielectric surfaces can be estimated with the displacement field from the simulation. The displacement field and a simplified form of Gauss's law[123] (Eq. 22) were used to compare the dielectric surface charge density at the needle with the surface charge density at the mesh. At the interface of the two mediums (dielectric and air), only the normal component of the dis-placement field affects the surface charge. The difference between the normal components of the displacement field of the dielectric (D_d) and air (D_{air}) equals the surface charge density (σ). The surface charge density builds up on the dielectric during discharge until it reduces the electric field across the gas gap to below the dielectric strength of air (E_b = 3 MV/m), extinguishing the filament. The simulation data are used in the surface integral of Eq. 22 to deter-mine the total surface charge at the needle and mesh locations on both the cathode and anode dielectric. The results at the cathode dielectric are plotted as the ratio of the needle surface charge to the mesh surface charge, and are shown in FIG. 30 (right y-axis). These results are insensitive (vary < 5%) to the minimum field value used to define the mesh and needle surface areas over which the integral is computed, as long as the integration area does not eliminate or combine the needle and mesh areas. Results from the anode dielectric showed that the surface charge ratio is 1 ± 1% for the 0.2 MΩ condition and 1 ± 0.01% for the 15 MΩ condition. This is to be expected since the longitudinal electric field is uniform across the anode dielectric for all needle bias cases as shown in FIG. 26.

$$D_d - \varepsilon_o \varepsilon_{air} E_{air} = \sigma \qquad \text{Eq. 22}$$

FIG. 30 shows that the surface charge ratio at the cathode dielectric is a function of the needle bias resistance. This is to be expected since the longitudinal field at the cathode dielectric changes appreciably as the needle bias resistance is changed, as shown in FIG. 26. As needle bias resistance decreases the surface charge ratio increases. At the filament turn off condition (15 MΩ), the surface charge at the needle and mesh is equal.

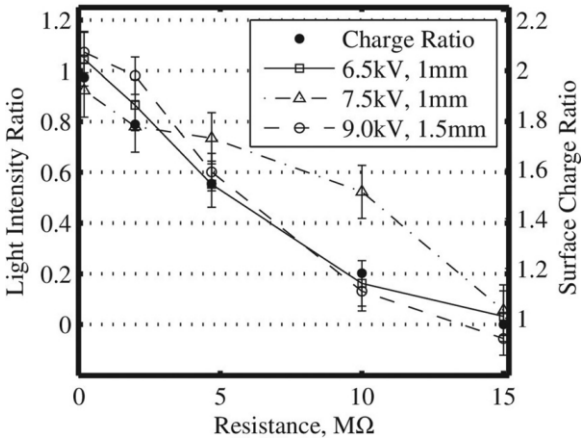

FIG. 30. Measured light intensity ratio between the needle and mesh filaments[100] and simulated total surface charge ratio between the needle and mesh locations as a function of needle bias resistance. The measured light intensity ratio is directly proportional to the simulated surface charge ratio

5.2.4 Light Intensity Relationship

Total surface charge, as described in Section 5.2.3, can be related to the expected light emission or light intensity from the plasma filaments. Here, we develop a control volume analysis of the process whereby surface charge is transferred between the dielectrics along a forming plasma filament,and relate the resulting current density to the light emission from the filament. We assume a static (no time dependence) 1-D model of the early time (first ~20 ns) when the filament is forming. This is the time period over which the majority of the current and light emission occurs, and the density of electrons remains constant.[115] Further, over this short time (much shorter than the AC DBD waveform), the gap voltage is approximately constant and equal to the full applied potential, i.e., the same conditions modeled in our aforementioned simulations. Through this analysis, we relate the ratio of the light emission

between the needle and mesh filaments to the ratio of the total surface charge at those locations. The analysis developed here is similar to previous models for streamer and filament formation in air.[115–117]

Consider a control volume that fully contains the plasma filament across the gas gap but does not envelope any adjacent filaments or the radially expanding surface charge. This volume is justified by the thin cylindrical form of the filament and the fact that filaments are spaced at a distance much larger than (about eight times) their diameter. Charge enters through the end of the control volume normal with the dielectric surface. All of the charge supplied to a filament from the dielectric moves along the filament to the opposite dielectric surface, parallel to the surrounding boundaries of the control volume. Electrons are the main charge carrier and their number density and drift velocity traversing the filament are given by the electron current density ($en_e u_e = J_e$). These electrons have ionization collisions with the back-ground gas as they traverse the gap. It is assumed that the emitted light intensity at any position ($\Psi(x,t)$, where x is location along the filament) is proportional to the ionization activity and can be written as the product of the Townsend coefficient (α), electron number density (n_e), and electron drift velocity (u_e) as shown in Equation Eq. 23.[115–117] This approach has been successful at describing filament formation and propagation in air.[115–117] If the light of the discharge is recorded along the axis of the filament, and over a time period (in our experiment 125 ms) far greater than the time period over which light emission occurs (~20 ns),[115] then the total measured light intensity (Ψ, per unit area) is the time and length integral of the filament, as shown in Equation Eq. 23

$$\frac{\Psi_{needle}}{\Psi_{\text{mesh}}} = \frac{\iint_{x,t} \Psi(\text{x,t})_{needle}\, dxdt}{\iint_{x,t} \Psi(\text{x,t})_{needle}\, dxdt} \propto \frac{\iint_{x,t} [\alpha(x,t) u_e(x,t) n_e(x,t)]_{needle}\, dxdt}{\iint_{x,t} [\alpha(x,t) u_e(x,t) n_e(x,t)]_{mesh}\, dxdt} \qquad \text{Eq. 23}$$

The density of electrons remains constant during the major charge transfer period over the first ~20 ns,[115] when the majority of the current and light emission occurs.[115] By charge conservation ($\nabla \cdot J_e = 0$; $J_{e,r} = J_{e,\theta} = 0$; $J_{e,x} \neq 0$), the current density along the length of the control volume is constant. Therefore, the space-time integral of the current density over the period of the filament discharge and the length of the plasma filament (L) yields the charge density (σ), as shown in Eq. 24. The constant cross-

sectional area of the control volume (A) and constant charge density due to charge conservation mean that the total charge is constant along the length of the filament. The resulting expression, in Eq. 24, relates the length and cross-sectional area of the filament, and the total charge (Q), to the space-time integral of the current density. This relationship shows that all the charge (Q) is transferred from the dielectric sur-face across the gap through the filament. This relationship enables Eq. 23 to be recast as Eq. 25.

$$\iint_{x,t} u_e n_e dxdt = \iint_{x,t} J_e dxdt = \sigma L = \frac{QL}{A} \qquad \text{Eq. 24}$$

$$\frac{\Psi_{needle}}{\Psi_{\text{mesh}}} = \frac{\iint_{x,t} \Psi(\text{x, t})_{needle} dxdt}{\iint_{x,t} \Psi(\text{x, t})_{needle} dxdt} \propto \frac{\left(\frac{QL}{A}\right)_{needle} \iint_{x,t} [\alpha(x,t)]_{needle} dxdt}{\left(\frac{QL}{A}\right)_{mesh} \iint_{x,t} [\alpha(x,t)]_{mesh} dxdt} \qquad \text{Eq. 25}$$

The Townsend coefficient (α) is given as Eq. 26 and is dependent on the pressure and electric field in the gap. In this model, the Townsend coefficient is constant with respect to time because the simulated field values (Efield) and pressure are constant on the filament formation time-scale. The pressure is 1 atm, and a collection of literature data from a Sandia National Laboratories Report[124] appropriate to these experimental conditions provides the curve-fits for the coefficients A = 8.805 and B = 258.45. The first Townsend coefficient is integrated over the length of the filament, using Eq. 26. However, due to the small variation between the electric field at the needle and mesh locations, the ratio of the integrated Townsend coefficient at the needle and mesh locations is 1 ± 0.002 for all voltage bias conditions. Finally, both the needle and mesh filament control volume have the same length (L) and are assigned the same area (A) so that the resulting light intensity ratio (Eq. 25) is directly proportional to the ratio of total surface charge (Q), as shown in Eq. 27

$$\alpha(x) = pAexp\left(\frac{-Bp}{E}\right) \qquad \text{Eq. 26}$$

$$\frac{\Psi_{needle}}{\Psi_{\text{mesh}}} \propto \frac{(Q)_{needle}}{(Q)_{mesh}} \qquad \text{Eq. 27}$$

A comparison of experimentally measured filament light intensity ratio $\frac{\Psi_{needle}}{\Psi_{mesh}}$ with simulation results of the total surface charge ratio $\frac{(Q)_{needle}}{(Q)_{mesh}}$ is shown in FIG. 30. Eq. 27 suggests that the ratio of filament light intensity between the needle and mesh locations should be proportional to the total surface charge ratio between those locations. FIG. 30 indeed shows this relationship. As FIG. 30 shows, the calculated surface charge ratio falls along the measured intensity ratio for 6.5 kV, 7.5 kV, and 9.0 kV driving voltages, albeit with an offset of 1. That is, the surface charge ratio values are off-set by the surface charge at the mesh location. This unity offset can be justified when one considers there will be a condition where charge exists at the surface of the dielectric but not enough to initiate a discharge. That condition appears to be the case when the charge ratio between mesh and needle position is 1:1. FIG. 30 also shows that the surface charge at the needle must be double that at the mesh (surface charge ratio of 2) when the needle light intensity is equal to that at the mesh (light intensity ratio of 1). Accounting for this unity offset, the calculated surface charge ratio is then within 4%, 11%, 12%, 26%, and 5% of the average measured light intensity ratio for bias values of 0.2, 2, 5, 10, and 15 MΩ, respectively. At 10 MΩ for 7.5 kV, the measured ratio is 160% larger than the calculated surface charge ratio. This trend may be due to additional surface charge built up across the dielectric surface, over areas of the mesh wire not in contact with the dielectric. Additional charge would allow for continued discharge at the filament before the turn off condition. The agreement of calculated and measured data suggests that the trend of light intensity can be correlated with the transferred charge when adjusted for the turn off condition.

5.3 Discussion

The mechanism which varies the light intensity is dependent on the charge distribution within the discharge gap rather than the total voltage drop across the gap. This is supported by the characteristics of the turn-off condition: (1) The minimum cross-gap voltage difference of one driving voltage condition does not drop below the maximum cross-gap voltage of a lower condition. (2) None of the conditions drop below the breakdown voltage of air (~3 MV m^{-1}).[16] (3) The turn off voltage remains at 7% of the

driving voltage for all three conditions representing a proportional distribution rather than a total field value. (4) The current drop necessary for filament turn off at the needle is the same for each driving voltage condition while the total current increases with the driving voltage. This indicates a relative charge buildup rather than a total charge build up. Redistribution of charge over the dielectric surfaces or within the discharge gap dis-places the field or limits the filament forming charge.

The variation of the light intensity demonstrates that both permittivity and presence of a filament can be controlled by a voltage bias at a locally selected electrode. The necessary voltage bias for filament turn-off is proportional to the driving voltage, at 7% for this setup. The bias voltage is an order of magnitude less than the necessary reduction to bring the cross-gap voltage below the breakdown voltage. This voltage reduction mechanism provides a more manageable method for electrically controlling an individual filament. The consistency of the light intensity variation between driving voltage conditions suggests that the permittivity of the entire array of filaments may be increased through the driving voltage while maintaining the relative permittivity difference between filaments. Since the discharge control is dependent on the proportionality and not a set voltage limit, further reduction of the controlling voltage value should be possible with a clearer understanding of how the voltage influences the charge distribution.

The movement of charge within the DBD due to the applied electric field displaces the filament-forming longitudinal field, and controls the formation and intensity of the needle filament. Cross-gap charge motion is dominated and controlled by the longitudinal field. The transverse electric field is less than 16% of the longitudinal field. Since the distance between the dielectrics (1.0 mm) is on the order of the distance between the needle and mesh position (0.88 mm), free charge movement between the dielectrics is dominated by longitudinal motion, and the transverse field does not significantly affect the charge distribution during the discharge period. The majority of transverse charge movement will then occur on the charged dielectric surfaces, where the longitudinal force is balanced by the normal force against the dielectric.

The transverse fields affect surface charges over microseconds of the driving voltage rise time, rather than nanoseconds of the discharge period. The transverse fields on the cathode dielectric isolate the needle and mesh charges. However, the transverse electric field on the anode dielectric surface transitions from positive to negative at the 15 MΩ condition, reversing the current direction of surface charge. Charge transfer between the two filaments can appreciably occur only on the anode dielectric surface, which is the dielectric furthest from the needle electrode.

For the reversed driving voltage polarity, the electric field direction reverses on the anode surface. Surface electrons move away from the needle towards the mesh to transfer across the gas gap through the adjacent mesh filaments. The charge movement still displaces the longitudinal field, by matching the lack of charge at the needle, and preventing discharge across the gap.

This work demonstrates that the on-off state of a filament can be caused by the difference between the electric fields of two adjacent low voltage electrodes placed behind a dielectric in a DBD. The voltage bias offsets the electric field profile of the needle, lowering the electric field profile of the needle below the mesh. These fields are a direct result of the electrode geometries. It is expected that by creating an array of electrodes that are geometrically similar to one another, the voltage bias difference required for filament turn off can be further reduced from the previously presented 476 V, 560 V, and 626 V for the driving voltages of 6.5 kV, 7.5 kV, and 9.0 kV. Reducing the necessary voltage difference would make a control circuit for an array of needle filaments a viable option for direct control of individual filament positions and permittivity.

5.4 Conclusion: Electric Field Simulation of Single Needle Experiment

This investigation into the applied electric fields within the DBD identified that surface charge interactions between a needle-generated filament and its adjacent filaments cause light intensity variations of the needle filament. Computer simulation of the geometry and measured boundary conditions show field trends that coincide with the 15 MΩ turn off condition. The filament turns off when: (1) the applied electric field profile along the needle filament lies below the mesh filament; (2) on the dielectric closest to

the needle and mesh electrodes, the charge over both electrodes is equal; and (3) the transverse field on the anode dielectric between the needle and the mesh reverses direction.

These trends are associated with the movement of electrons on the dielectric surface furthest from the needle and mesh electrodes (the anode in the simulation). Along the anode dielectric, electrons transferred from the mesh to the needle position displace the longitudinal field of the needle so that there is no filament formation at 15 MΩ. Effects of charge transfer in the air gap or on the dielectric surface closest to the needle and mesh electrodes (cathode in the simulation) were eliminated as significant transverse charge movement regions, due to inhibiting fields.

The variation of the experimental light intensity was related to the total charge transferred across the filament, and calculated using dielectric surface charge. The calculated light trend was shifted to zero at 15 MΩ, to match the observed lack of discharge. However, the experimental light intensity trend agrees with the calculated surface charge trend to within 8%. A charge decrease equal to the total charge at the mesh filament is the difference between the full light intensity and no light emission at the needle filament.

An explanation has been presented for a lack of plasma discharge where the local peak electric field is above the turn off dielectric strength of air. Field trends have been presented for identifying filament turn-off points, and making light intensity predictions using an electrostatic field simulation. The controlling voltage bias has been related to the electric field difference between adjacent electrodes, and can be reduced by increasing the geometric similarity of these adjacent electrodes.

6 Experimental Digital Control of Filaments

The study in Section 4, showed that it was possible to control the light intensity of a single DBD filament, and so the electron density. It also demonstrated that the control mechanism was an applied resistive voltage bias applied at the pin located behind the dielectric and under the controlled filament. The goal of this section is to create an array of multiple addressable pins with a digital control mechanism to control the array of pins. This task was complicated by integrating digital components with high voltage, stray capacitance at the millimeter scale, and material build up on the dielectric surface.

6.1 Individually Addressable Electrode

The individually addressable electrode array is constructed from a 10 x 10 pin array produced by Ironwood Electronics Inc. (Model: SF-BGA100B-B-41) with 0.2 mm diameter pins, rounded tips of the same diameter, and a lattice constant of 1 mm. As shown in FIG. 31, the pins are imbedded into a FR4 substrate with solder balls attached on the opposite side for soldering to an array PCB solder pads. The PCB disperses the connections from the 1 mm pitch solder pads to a 2.54 mm common pin header pitch to which wire leads are attached. The discharge conditions from Section 4. are replicated with this setup by also using a 1 mm discharge gap, a 0.1 mm low voltage dielectric, and a 1 mm high voltage dielectric. The components are kept in place by compressing the PCB to the “Upper Frame” with four bolts placed in the corners.

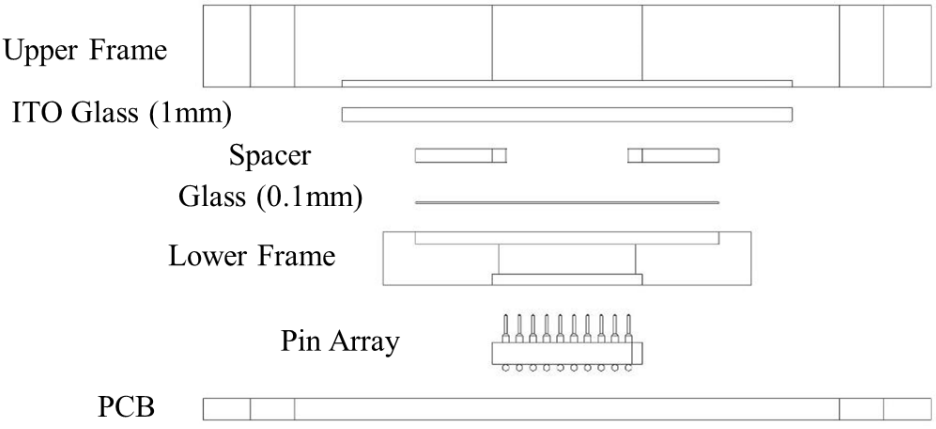

FIG. 31. Schematic of the DBD with individually addressable electrodes. Vertically exploded side view.

The driving voltage sine wave is kept at 7.5 kV and 3.2 kHz. The signal is produced by a Rigol DG-1022 Function Generator, powered by a Crown Macro-Tech 1202 Audio Amplifier, and raised to high voltage by a Corona Magnetics 5525–2 Transformer with a turn ratio of 1:357. This is the same driving voltage source used for the experiment in Section 4. The high voltage lead is connected to a layer of copper tape that is compression fit to the conductive transparent coating of the high voltage dielectric ("ITO Glass"), FIG. 32. The two dielectrics are separated by machined spacers that are also compression held in place by the acrylic frame.

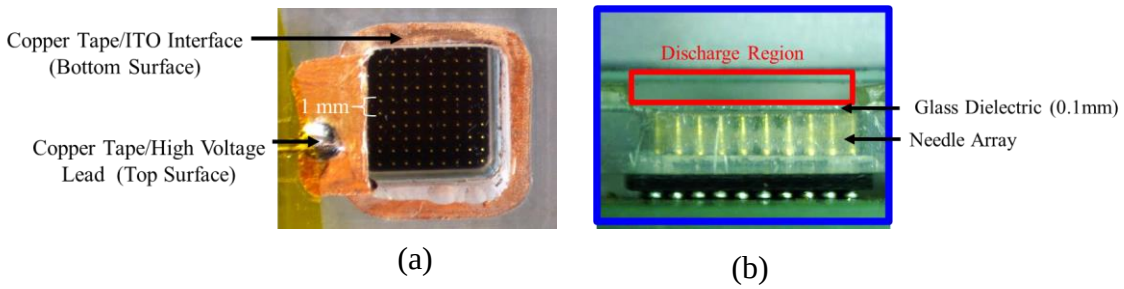

FIG. 32. Images of the pin assembly. (a) Top view down through the Upper Frame, ITO Glass, and 0.1 mm glass to the electrode pins. (b) Side view of the pin and discharge region.

6.2 Replicate Single Pin Light Intensity Control

The first test of this setup failed since the biasing voltage did not rise to the same level as previously measured in FIG. 23. Phase and voltage measurements at the pin for different biasing resistors exposed the presence of a capacitive coupling between the biased pin and the surrounding pins/PCB circuitry. The circuit diagram for this situation is shown in FIG. 33, without the "External Capacitor" on the upper right corner. The capacitive coupling allowed an alternative path for the current to travel to ground and made the biasing voltage less effective. The solution to this problem was to add an additional current source to the biased pin which raised the effectiveness of the resistive bias. A lower resistance could then elevate the voltage to the desired value. As long as, the necessary range of resistances was significantly less than the "Coupling" impedance (FIG. 33), the current would primarily pass through the resistor. This allowed the resistor to produce voltage values at the pin on the order of those in FIG. 23.

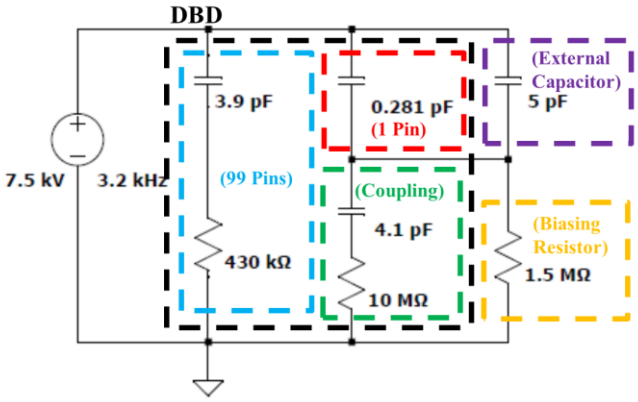

FIG. 33. DBD circuit diagram with external capacitor and capacitive leakage. The components are the capacitive drop across the gas gap for the biased pin (red), the biasing resistor (yellow), the capacitive coupling leak of current through surrounding circuitry (green), the impedance across the DBD of the other 99 pins (blue), and the external capacitor providing the extra current source to the biased pin (purple).

The circuit model, depicted in FIG. 33, was validated with voltage measurements made at the pin for a 2kV driving voltage. A comparison between data and the model is shown in FIG. 34. The model shows that voltage produced by a given biasing resistor is inversely dependent upon the external capacitor's impedance. The extreme of which is at zero impedance and would be a direct connection to the driving voltage. With this understanding of the capacitive leak and a predictive model for the solution, the individually addressable array circuit was modified to produce the necessary voltage at the pin.

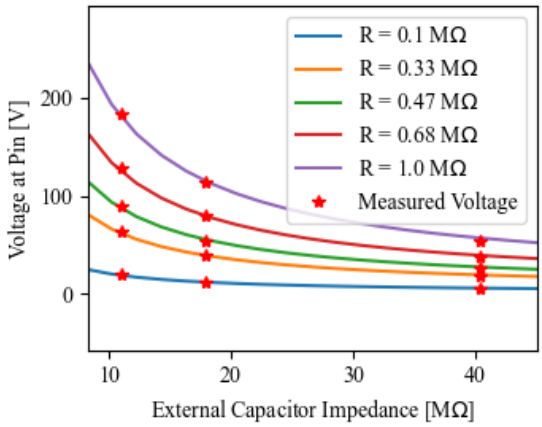

FIG. 34. Measured and modeled pin voltage as a function of external capacitor. Measured values associated with nearest resistor line. Driving voltage set at 2kV to collect non-discharging data.

With an external capacitor impedance of 11MΩ at 3.2kHz, the light intensity for different resistances produces the data in FIG. 35, for three different tests. A linear relationship between the normalized light intensity and biasing resistance follows the same trend shown in FIG. 23. This evidence validates the individually addressable pin array as a structure for controlling plasma discharge intensities.

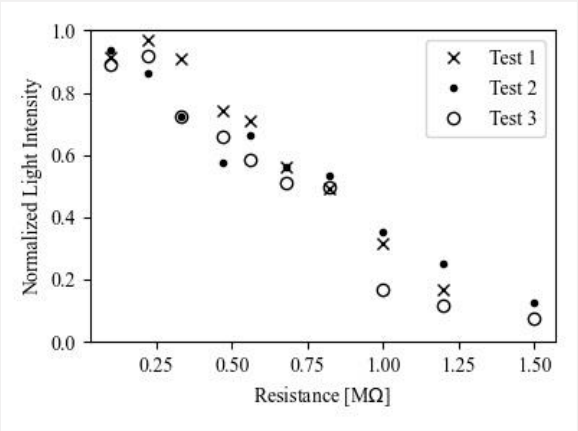

FIG. 35. Normalized light intensity for the 10x10 array with external capacitor. Three separate tests are shown to demonstrate consistency. (There was no 1.5MΩ for the first test).

6.3 Multiple Filament Control

The bias control method is applied to multiple pins to demonstrate the dimming of multiple adjacent pins, FIG. 36. For this case, a row of 10 pins out of the 10x10 array are connected in parallel. The ten pins are connected in series with a biasing 1.5 MΩ resistor attached to a 11 MΩ external capacitor impedance. The light intensity looking at the side view, with each filament overlayed, clearly shows a decrease in intensity and plasma diameter compared to the other rows of filaments. However, the light intensity is still present at these pin locations even though their resistance is 1.5MΩ which created the turn off condition found in FIG. 35.

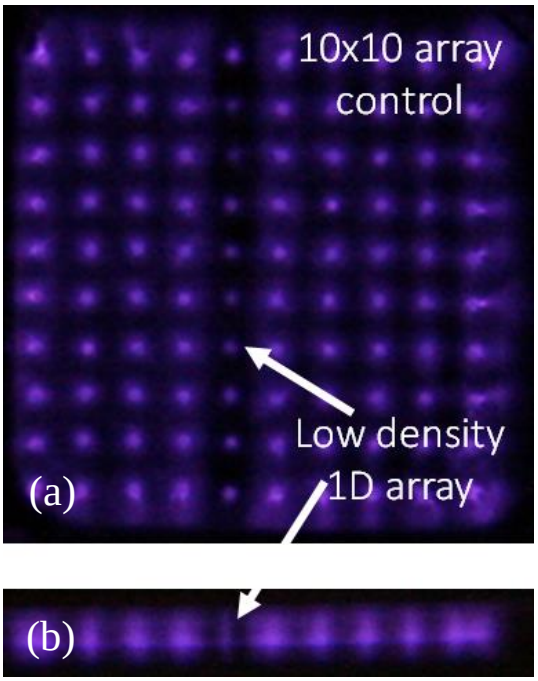

FIG. 36: Top view (a) and side view (b) of the plasma array with an entire column biased by a single 1.5MΩ resistor. Light intensity is decreased along the entire column, relative to the unbiased plasma filaments.

This lack of OFF state, is explained by the additional 9 pins which reduce the effectiveness of the biassing resistor by adding 9 more capacitive coupling paths to ground, outlined with green in FIG. 33. The added paths reduce the current through the biasing resistor and reduce the biasing voltage. To address this issue, the external capacitor must be increased (reducing its impedance) to allow more current through to the biasing resistor and increasing the bias voltage. To test this, the circuit model of FIG. 33, validated in FIG. 34, is modified to included extra pins. If each additional control pin also has its own separate external capacitor, then the pin voltages follow the trends found in FIG. 34 for a given biasing resistor and external capacitor. Each pin must have its own external capacitor and biasing resistor to maintain the necessary biasing voltage to turn-off the filament.

6.4 Digital Biasing Circuit

To control the full 10x10 array of 100 pins, the resistive mechanism must be digitally controlled. The simplest method would be to use digital resistors. However, the voltage values of FIG. 23 are prohibitive for commercially available digital resistors that have ratings which do not go above ~50V.

The solution is to replace the variable resistors with high voltage transistors that limit the current, similar to the way a resistor would. The preferred choice is a MOSFET that limits the current flow dependent upon the controlling voltage at the gate and has kilovolt ratings. Several considerations complicate the design of the control circuit, but the current solution is the diagram shown in FIG. 37.

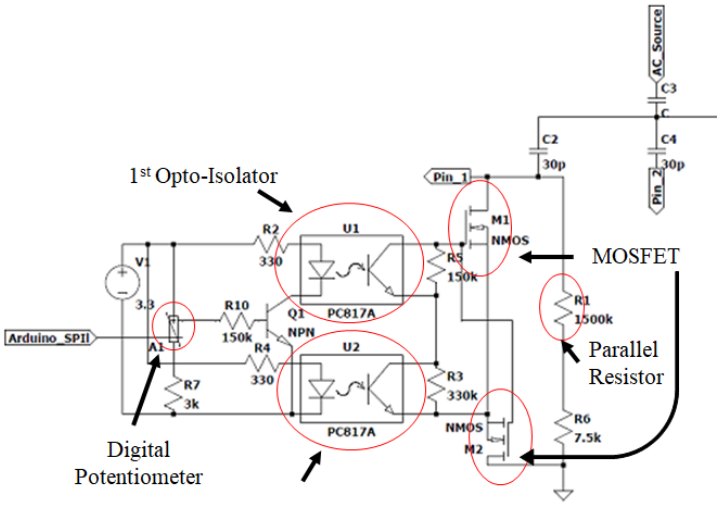

FIG. 37. Digital control circuit diagram for a single pin. Arduino digital, pin lead, and AC driving voltage are labelled as inputs. The circuit would be replicated and attached to Pin_2, Pin_3, … Pin_N. Red circles and callouts identify the primary components of the control circuit that allow a single digital input to bias the AC voltage on any number of pins up to 1kV.

<u>The complicating considerations:</u>

1) A MOSFET only operates in one direction since it is normally used as a DC switch. The solution is to place two MOSFETs in series but in opposite directions so that one will always be able to block the current. An internal diode allows the current to move past a MOSFET when it is placed in the reverse polarity. This meant that the inactive MOSFET does not interfere with the operation of the active MOSFET.

2) If the MOSFET were turned off, the pin would experience an infinite resistance which would drive the pin voltage to higher than desired values. To fix the upper resistive limit, a resistor with the desired upper resistance is placed in parallel with the MOSFETS. This has the added advantage of decreasing the sensitivity of the MOSFET to gate voltage changes.

3) During the negative AC polarity of the driving voltage, the MOSFET floats the input voltage (gate voltage) to the pin's biasing voltage. If multiple circuits are to be connected to one digital controller, these gate voltages must be isolated from each other and their digital input. This is accomplished with photovoltaic optical isolators (opto-isolator). The opto-isolators provide an isolated power supply and set the MOSFET gate voltage by driving a current through the photodiodes in the isolated digital circuit.

4) The MOSFET gates are sensitive to voltage changes but the opto-isolators have a 5% error input-output value. The required voltage range over which the gates change is 2.0V – 2.5V. To account for the sensitivity and error, the base voltage of 2.0V is set by the first opto-isolator and the second provides greater fidelity. The necessary current for the opto-isolator, 10mA, is larger than a digital potentiometer can handle. This control current is supplied by a transistor that is then controlled by a digital potentiometer with input from an Arduino Uno micro-controller.

5) Multiple pin control circuits must be independent while still utilizing the same circuit. For the digital input, the same signal is sent to all potentiometers while an ON signal is sent to the targeted potentiometer that tells it to listen to the digital signal. The ON signal is sent through a Multiplexer that manages which potentiometer receives the ON signal while the others are biased to an OFF state. In addition, the external capacitor must be shared by all pins to minimize the number of high voltage capacitors needed to drop the voltage from the driving 7.5kV to 0V at the pin. To ensure each pin still has a relatively independent biasing voltage, an additional 30pF capacitor is added to allow the pin to vary between ground and the common voltage to which all pins are connected. FIG. 37 shows the common voltage between C2 and C4 to which all pins are connected.

After accounting for these design considerations, a prototype circuit board was assembled, as shown in FIG. 38. Four replicated circuits are stacked along the circuit board.

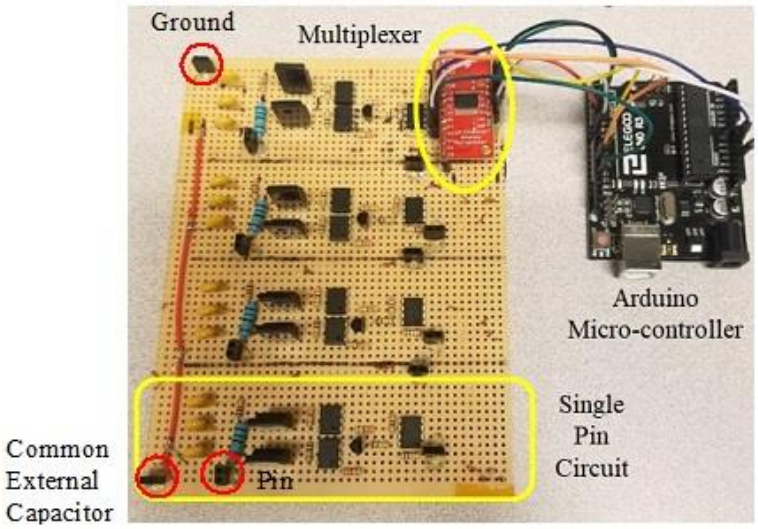

FIG. 38. Control circuit prototype. Four circuits of four pins, integrated with Arduino for digital input and multiplexer for selecting the pin to adjust. The three red circles represent the pin connections to ground, to the common connection for the pins and the external capacitor, and to the pin for the highlighted circuit.

All four circuits are varied over the 129 possible voltage settings while the resistance through the MOSFETs was measured. The results of this analysis are shown in FIG. 39. Although there is a shift along the digital input axis where the resistive curve occurs, this can be accounted for in the programming by storing a calibration curve for each circuit. The shift in this data is due to the inherent error of the opto-isolators output, which was determined to be 5%, after testing 10 different opto-isolators in the same circuit. The shift in the digital input is larger than 5% since the digital input only represents the 1V range for one opto-isolator output. There is a second opto-isolator that supplies a fixed output of 1.8V necessary for activating the MOSFET. The combined 10% error over 2.8V results in the 40 integer difference between the curves.

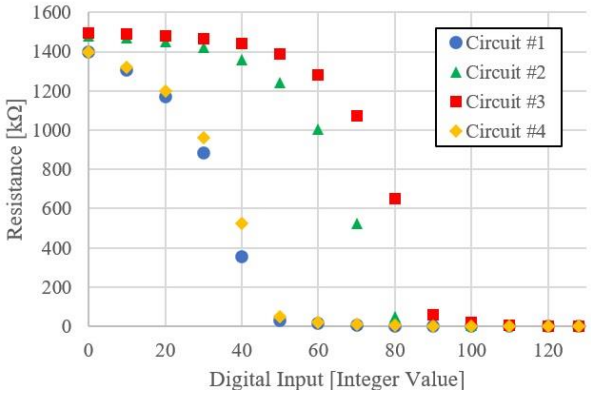

FIG. 39. Circuit resistance as a function of 128 possible integer digital inputs. The shift in the in curve is due to the manufacturing error of the two opto-isolators in the circuit.

As a demonstration of the circuit's performance, one of the circuits was used to turn the filament from an ON to OFF state, by changing the resistance of the MOSFET, as shown in FIG. 40

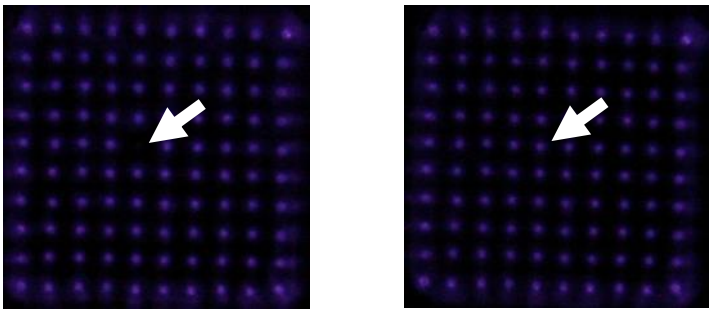

(a) (b)

FIG. 40. View of the 10 x 10 filament array with control circuit set at (a) 1.5MΩ and (b) 100Ω. Viewed through the ITO glass, along the length of the plasma filaments. The white arrow points to pin location that is attached to the controlling circuit.

6.5 Complicating Factors for Fully Integrated Digitally Controlled PPC

6.5.1 Hydrocarbon Build Up on Dielectric Surface

During the testing process, the light intensity of all the filaments would become less consistent and diffuse. An unknown material built up on the surface of the 0.1 mm glass, on the surface exposed to the plasma, as shown in FIG. 41. The material build up was caused by the plasma discharge since it occurred at the locations of the plasma filaments. This degree of deviation would occur after about 1.5

minutes of plasma discharge. The material build-up also prevented the biasing resistor from affecting the filament light intensity, eliminating the control mechanism.

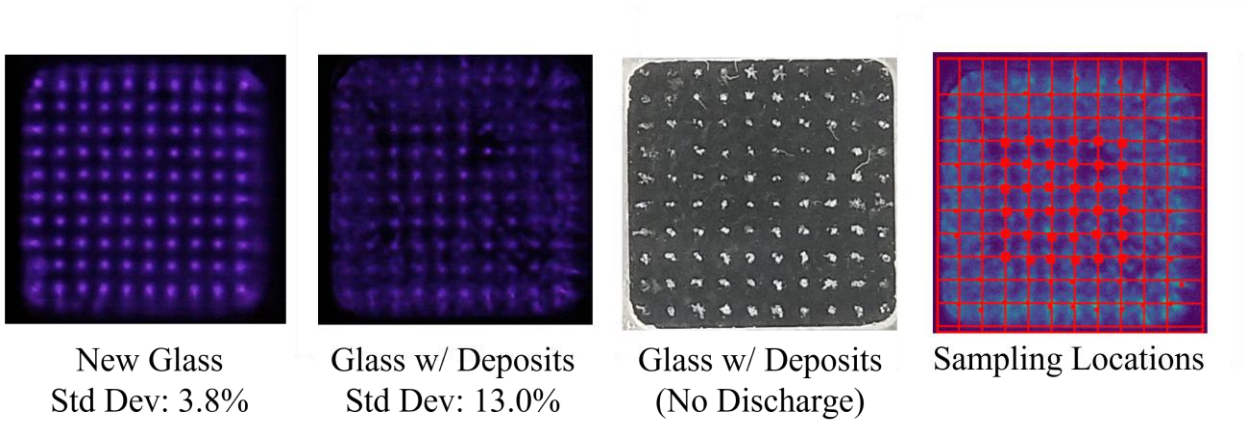

FIG. 41. Filament uniformity effect of material deposits on the surface of the 0.1 mm glass. The standard deviation of the light intensity from a 6x6 sampling array increases from 3.8% to 13.0% as material builds upon the surface after repeated testing.

After probing the impedance between control pins, the material build-up was found to create a measurable resistive path between control pins. The resistance on the surface of the glass exposed to the plasma was measured between pin locations, relative to a single pin location, and plotted as a heat map in FIG. 42. There is at least an 11 MΩ resistance between pin locations. Although, this is large, it is on the order of the coupling impedance in the circuit model of FIG. 33, adding another route for current to flow away from the pin location. The conductive surface prevents the surface charge from building up at the filament footprint, causing the diffuse plasma distribution observed in FIG. 41.

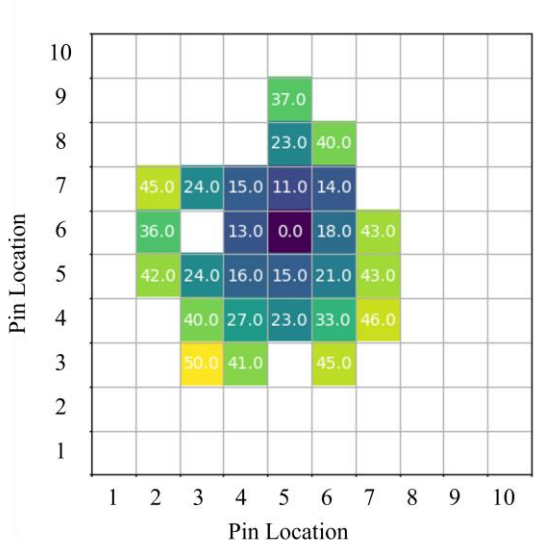

FIG. 42. Resistance (MΩ) on the plasma exposed surface of the 0.1 mm glass, between the pin located at (5,6) and the surrounding pin locations.

The surface of the 0.1 mm thick glass was analyzed with Secondary-Ion Mass Spectrometry (SIMS) to determine the material on the surface. A 0.4 x 0.4 mm^2 area above one of the pin locations was measured. The silica distribution, representing the clean glass area, is shown in FIG. 43. The distribution clearly shows that some non-silica material is coating the surface. A concentrated region of the unknown material, shown in FIG. 43 (left), was isolated and analyzed for the material content, revealing a high concentration of hydrocarbons.[125] (The SIMS data is given in Appendix D) Since the glass surface is located inside the discharge region and isolated from the surrounding electrodes by an acrylic frame, the most likely source of hydrocarbons is the acrylic frame. To correct for the loss of filament uniformity and filament control, the acrylic frame can be replaced by a ceramic frame such as MACOR.[126] The

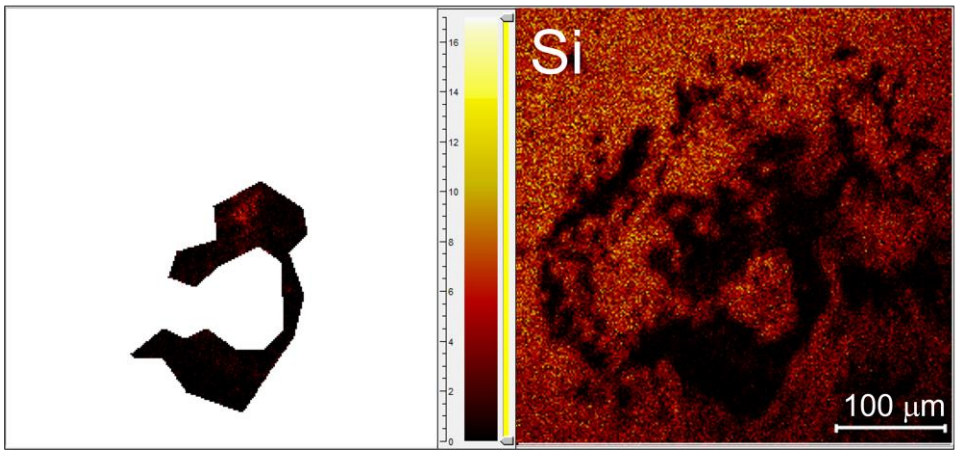

FIG. 43. SIMS measurement of the Silica distribution over a 0.1 mm thick glass plate with the unknown material build up shown in FIG. 41. (Right) The distribution area focuses on a 0.4 x 0.4 mm^2 square area above a single pin location. (Left) The selected area of the distribution analyzed as the "Region of Interest."

6.5.2 Arduino Disrupted by Electromagnetic Interference

During discharge testing with the Arduino, the setup shows signs of electromagnetic interference (EMI) that causes the control system to not work as desired. Three pieces of evidence suggest irregular operation due to the Arduino microcontroller during discharge testing:

1) The camera, attached to the Arduino, begins to operate its shutter at a rate that is different from its programming. The camera is attached to the Arduino to sync the photos with different voltage biases. The Arduino program is set to take a photo and change the voltage bias every two seconds. During discharge testing the camera begins to take photos more than one photo per second and at irregular times. The Arduino control of the camera operates correctly when the plasma is not discharging.

2) Photos of a controlled filament show it turning OFF and ON when the programmed value is set to a fixed-ON condition. The Arduino control is set for a resistive value of less than 1 kΩ which would allow all the current through the MOSFET and prevent any biasing voltage. However, as seen in FIG. 44 a sequence of photos with 1 second intervals, the controlled filament turns OFF, ON, and OFF again. There is no consistency. The circuit should default to an open circuit This contrast with the control of the filament when the Arduino is removed from the system.

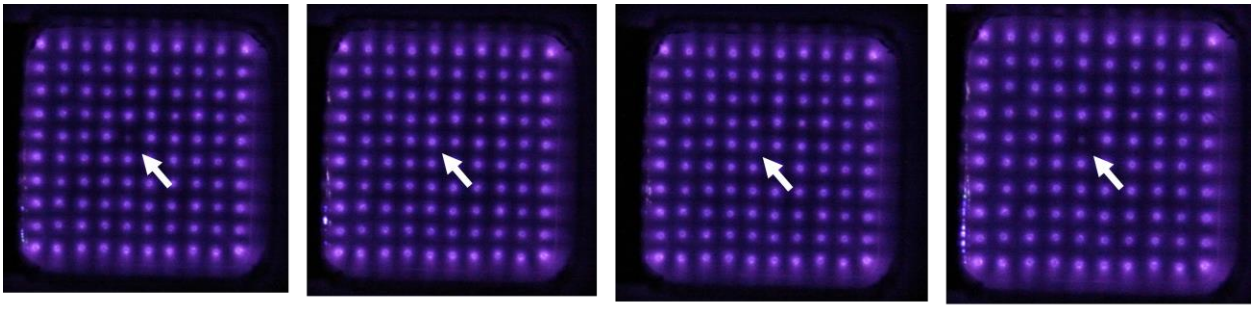

FIG. 44. Sequential photos sing the Arduino control circuit, with a 1 sec interval between photos. The Arduino circuit was set for a filament ON state (R < 1 kΩ).

3) Each control circuit operates as expected when the Arduino input is replaced by a fixed battery voltage. The Arduino is replaced by a 3.3 V regulated battery to power the MOSFET gate voltage. The digital potentiometers hold their set value without power, so they are first set by the Arduino and then the Arduino is removed from the circuit. Without the Arduino, the controlled filament is turned off by the circuit, as shown in FIG. 45. In this figure, all four of the constructed control circuits from FIG. 38 are tested to demonstrate their ability to turn OFF the filament. The wiring was changed to control the same pin location.

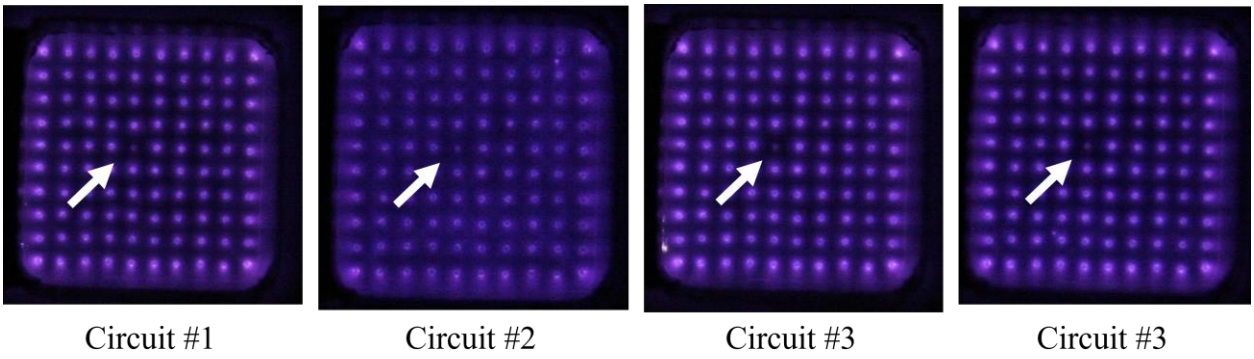

FIG. 45. Demonstration of all four separate control circuits operating with the Arduino detached from the system. The Arduino is only necessary to power the MOSFET gates and change the potentiometer values.

6.5.3 Capacitive Crosstalk Between Wires

The wires connecting the PCB of FIG. 31 and the control circuit of FIG. 37 have stray capacitance between them that interfere with the biasing voltage. When the wire leading from as control

pin touches any of the wires leading from the surrounding pins, the biasing voltage does not reduce the light intensity of that control pin. The thin insulation on the jumper wires only prevents a conductive current between the wires. The AC signal sees the small separation to another wire as a capacitive path to ground, like the stray path in FIG. 33. To successfully test a control pin, high voltage wire with an outer insulation diameter of 3 mm was used to isolate the wire. Shielding around the wire would not be an option since it too would form a path to ground. The ideal solution would be to have the control circuit and the control pin PCB directly connected through same board-to-board pin connector scheme. That way the biasing signal would have a fixed stray capacitance that could be accounted for in the control circuit.

7 Conclusion of PPC Work

The goal of this project has been to demonstrate a new control system for a 2D PPC formed from a DBD to increase the tunable frequency range of the bandgaps. The new control system uses individually controlled plasma columns to rearrange the PPC structure and change the frequency range by an order of magnitude. During this process, the effects of different controlling parameters have been clarified and the preferred parameters identified for controlling the average frequency (background dielectric) and bandwidth (plasma radius). The physical mechanism developed to implement the individual column control, uses a biasing resistance on individually addressable electrodes behind each filament to vary the light intensity of a single filament from 10% to 100% of the surrounding filaments' light intensity. The light intensity is correlated with electron density, providing control over the plasma permittivity of each filament. The control mechanism has been demonstrated for a single filament and expanded to a 10x10 array of individually addressable electrodes. A digitally controlled circuit demonstrated the necessary filament ON/OFF performance and the resistive capability to replicate the light intensity variation between the ON/OFF states. A circuit for integrating multiple circuits was constructed and tested. Digital integration problems have been identified with suggested solutions for a full digitally controlled PPC array.

8 Plasma Water Treatment

This work was performed as part of a collaborative project between the University of Southampton (UoS) and the University of Illinois Urbana-Champaign (UIUC) to develop a new surface DBD plasma water treatment system for laboratory decontamination.

8.1 Background

Water pollutants from different industries have been shown to be able to pass through current chlorine water treatment systems without a reduction in concentration.[127,128] Although the measured levels of pollutants are below allowable regulation limits, the build-up and long term effects of new or unregulated contaminants are a significant concern for public safety.[129,130] For many of these pollutants, such as herbicides, pesticide, pharmaceuticals, and microplastics, there is limited control over their entry into drinking water sources. An alternative to the conventional chlorine treatment method, therefore, is required to secure drinking water safety from these contaminants.

Advanced oxidation processes (AOPs) are one of alternatives for removing water pollutants, and ozone based AOPs have gained growing attention due to its high oxidizing power and excellent disinfecting capabilities. Ozone has twice the oxidation potential of chlorine and one of the highest overall oxidation potentials, making it a more effective reagent than chlorine and able to address these new contaminants.[131,132] Ozone and the free radical hydroxyl (OH-) it produces in water both decompose organic compounds and mineralize inorganic compounds.[133] The major advantages of ozone treatment are faster treatment time, more effective disinfectant, no harmful residuals, no chemical transportation and storage safety issues, and improved taste.[132] However, ozone is unstable, reducing to oxygen gas at a half-life rate ranging from seconds to a day, depending on the mass flow rate, humidity, and temperature.[134] For this reason it is manufactured at water treatment facilities by plasma discharge, which has become a more prevalent method of water treatment.[135] Chlorine treatment is generally accepted as being more economical than ozone treatment,[136]although this position has been disputed by the ozone water treatment community.[137] This has driven researchers towards improving the efficacy of the ozone treatment.

Along with ozone, the plasma discharge produces free-radical species during the ionization process. The high electric field of the discharge accelerates electrons which collide into the working gas to break the molecular bonds and create the unstable species. The energy input of the discharge is effectively used to raise the bond potential of the gas species which then breaks the bonds of the water contaminants.[138] In conventional ozone AOPs, most of the free radicals are neutralized during transport from the discharge source to the water surface. This creates a loss mechanism as the discharge energy is reabsorbed within the chemical bonds. The goal of plasma water treatment compared to conventional ozone water treatment is to move the plasma source adjacent to the water, so that the more reactive free radicals have time to diffuse into the water in significant quantities.

A variety of discharge methods and configuration have been studied for plasma-water treatment: arc discharge,[139–141] dielectric barrier discharge (DBD),[142,143,152–154,144–151] plasma jets,[155] and microwave plasma generation.[156,157] The goal of the plasma water treatment is to bring it as near as possible to the water. Some studies implemented varying mixing methods rather than just treating the water surface. Oxygen gas is the preferential feed gas[144] since it promotes the production of ozone by 2-4 times that of air.[132] Although low concentrations of nitrogen gas may be beneficial to ozone production, high concentrations of NOx recombines the ozone back to oxygen gas. All treatment methods followed an exponential time dependent degradation, indicative of a first order reaction rate.

In this study, we use methylene blue (MB) (3,7-bis (Dimethylamino)-phenothiazin-5-iumchloride) as an indicator of water pollutants removal efficiency because it is non-biodegradable and a common water pollutant found in most industrial wastewater.[158] MB has two distinct absorption peaks for spectroscopy[159] and a strong blue color at 1 mg / 100 ml for visual inspection. The agreement between absorption and concentration during discharge degradation was validated using tandem chromatography and spectroscopy measurements by Foster et al.[155] MB absorption is also used in this study as the degradation indicator.

The concentration of MB with ozone over time is an exponential curve. [139,140,149–157,141–148] This suggests a order reaction, Eq. 28,[160] with a decreasing reaction rate per time. The the reaction rate (ν) is dependent upon a reaction rate constant (k) and the compound concentration (C) of MB and ozone.

$$v = \frac{dC}{dt} = kC_{MB}C_{O_3} \qquad \text{Eq. 28}$$

As the reaction progresses, the rate decreases due to the decreased concentration of MB. The following implications of this equation can be considered when evaluating the parameter trends: 1) More MB in the reaction will produce a greater reaction rate, processing more MB with time. 2) More ozone must be added to maintain the reaction rate when the MB concentration is reduced. 3) To increase the amount of MB without changing the MB or treatment time, the quantity of ozone entering the water must be increased. So, the primary design goal of an ozone water treatment system should be to maximize the quantity of ozone entering the MB solution.

The ozone's mass transfer rate (N) into the water volume (V_L) is modeled by the Lewis-Whitman twin film model, Eq. 29.[161,162] The model assumes that at the air-water interface there are two thin films where the ozone concentration decreases across the two films as it moves from the higher concentration gas to the lower concentration solution. The product of the liquid transfer coefficient (k_a) and the area per unit of liquid volume (a) is the global mass transfer coefficient (k_a•a) which has a value of 0.3 – 1 [min^{-1}], depending upon the bubble velocity.[163] The global mass transfer coefficient is experimentally determined to be ~4, so that the area per unit of liquid volume primarily determines the global mass transfer coefficient. The saturation concentration (C_L^*), the dissolved concentration at equilibrium with the gas phase, is related to the gas concentration (C_G) by Eq. 30, where the temperature (T) is expressed in ^oC. An empirical model of the solubility ratio (m) as a function of the gas phase concentration is defined by Eq. 31, for a total pressure of 1 atm. The solubility ratio is also linearly increased with the total pressure. However, the dissolved ozone saturation decreases with temperature. So, to maximize the concentration within the water either the gas phase ozone concentration (C_G) or the area per unit liquid volume (a) must

be increased. From these two parameters, only the area per unit volume will improve the efficiency of the plasma treatment process since an increase in ozone production will require more power.

$$N = (k_a a)(C_L^* - C_L)V_L \quad \text{Eq. 29}$$

$$C_L^* = m \cdot C_G \quad \text{Eq. 30}$$

$$\text{m} = 2.00e^{0.549 \cdot C_g} \quad \text{Eq. 31}$$

The area per unit volume of liquid for a two phase vertical flow is dependent upon progressive flow regimes: bubble, slug, churn, annular, and mist, as depicted in FIG. 46.[164] In vertical flow, the regimes depend upon the respective volumetric flux of the two phases. So, by increasing the gas flow rate, the flow will start with bubbling and eventually develop into a mist. The area per unit volume of liquid will increase as the water volume within the flow field decreases, due to the squared-cubic ratio of area to volume. For the different flow regimes, the area per unit liquid volume increases in FIG. 46 moving from left to right. To maximize ozone mass transfer from gas to liquid phases, the maximum area per unit liquid volume ratio for a misting two-phased flow is ideal. The second-best regime is annular flow, where the gas and water phase share a surface along the direction of flow. The majority of the referenced ozone/plasma water treatment methods use bubbling, with the minimum area to liquid volume ratio.

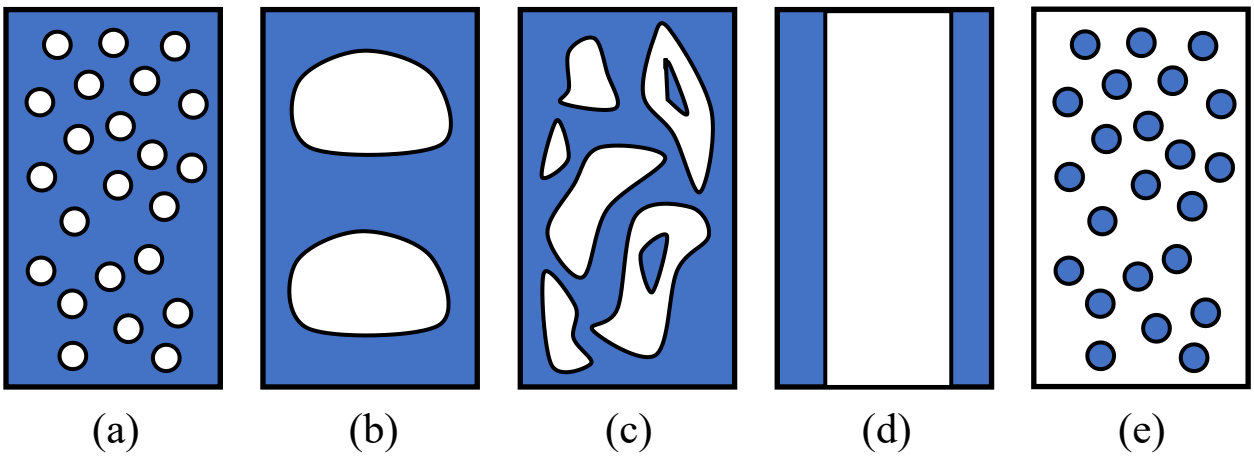

FIG. 46: Different types of two-phase flow regimes: (a) Bubble, (b) Slug, (c) Churn, (d) Annular, and (e) Mist. The ratio gas to liquid volumetric flow rate increases from left to right.

8.2 Material and Methods

8.2.1 Material and Sample Preparation

The oxidative capacity of the generated plasma microbubbles is quantified using methylene blue (MB). Methylene blue is commonly used as a general dye and used for biological staining. A MB solution will reduce its colour intensity and even turn colourless when exposed to increased oxygen levels. In this study the MB solution is prepared by dissolving MB powder (Scientific Laboratory Supplies Ltd. – CHE2582) in deionised water. The MB powder is weighed using an analytical weight balance (UoS: Kern, ABS 220 / UIUC: Sartorius, Quintix 125D-1S) with a resolution of (UoS: ±0.1 mg / UIUC: ±0.001 mg) and the deionised water is measured in a volumetric flask with the tolerance of (UoS: ±0.4 ml / UIUC: ±2.5 ml). The baseline MB solution of 1 mg / 100 ml is achieved by dissolving (UoS: 4 mg / UIUC: 5 mg) of MB into (UoS: 1 L / UIUC: 500 ml) of deionised water to generate stock solution, which is then further diluted down to the final MB solution of 1 mg / 100 ml (UoS: ±3% / UIUC: ±1%). A detailed procedure for the MB solution at UIUC is presented in **Error! Reference source not found.** E. Preparation of a high concentration stock solution results in lower error margin due to the larger relative error in the weight measurement of MB. Lower concentration are achieved by mixing the baseline solution with deionised water.

8.2.2 Absorption Spectroscopy

The efficiency of the plasma microbubble treatment procedure is analysed by measuring the absorbance of treated MB solutions using absorption spectroscopy. The absorbance is measured using a spectroscopy setup (Ocean Optics, HR4000) at UoS and a photometer (Hanna instrument, HI-83300) at UIUC. The ocean optics spectroscopy setup consist of halogen light source (Ocean Optics, DH-mini), cuvette holder and the spectrometer with a wavelength range from 200 to 1100 nm (Ocean Optics, HR4000). The MB solution sample is filled in a plastic cuvette and placed in the cuvette holder, where the absorbance is measured over the full wavelength range. The photometer setup relies on the same

principal, with an integrated light source at a fixed wavelength of 610 nm. The 610 nm wavelength is chosen for measurement because it corresponds to one of two strong and dominant MB peaks.

The absorbance measurements, A, can be converted to MB concentration, C, using the Beer-Lambert Law,[165] as:

$$C = \frac{A}{\varepsilon d} \qquad \text{Eq. 32}$$

where ε is the MB extinction coefficient at 610 nm with 37418 cm^{-1} M^{-1},[166] and d the cuvette diameters of 10 mm at UoS and 22 mm at UIUC. The extinction coefficient is obtained from a tabulated spectrum performed by Prahl using a HP spectrophotometer using a 1 cm quartz cuvette filled with a 10 μM solution of MB in Water.[166] This value agrees with published experimental and theoretical values reported by Fernandez-Perez and Gregorio Marban.[159]

Absorption measurements at different prepared MB concentrations were performed to define three sources of MB absorption measurement error: agreement between UoS and UIUC data, initial sample preparation, and repeatability. The data sets are presented in FIG. 47 with curve-fits applied to both UoS and UIUC data sets that are forced to pass through the origin. A 1:1 unit line represents the ideal agreement between the absorption and prepared concentrations. Although the vials and test setups between UoS and UIUC are different, the UIUC trendline is only 7.4% greater than the UoS trendline. The percent error from the 1:1 line for UoS and UIUC are 2.6% and 8.6%, respectively. The five UoS data sets and three UIUC data sets have standard deviations of less than 3% and 6%, respectively. Although additional error is introduced by the experimental setups, the error values demonstrate the confidence in the solution preparation and measurement consistency.

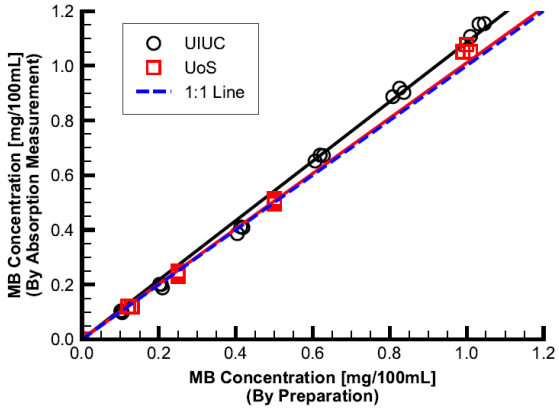

FIG. 47: Concentration by absorption vs Concentration by solution preparation.

Although the concentration calculation is necessary to validate the absorption measurement method, the remainder of this work reports the plasma processing capability in degradation efficiency, η, as a percent of the initial MB solution, defined by Eq. 33.[143,144,146,147] This approach is used to normalize the treated absorption, A_a, with the initial absorption, A_o, when evaluating the parameter variations.

$$\eta = \frac{A_o - A_a}{A_o} \cdot 100 \qquad \text{Eq. 33}$$

8.3 Porous Surface DBD Bubble Setup

The discharge approach used in this study is a surface DBD, unique from previous volume DBD configurations. (Surface DBD: Two electrodes off-set along a separating dielectric barrier create a plasma along the surface of the barrier from the surrounding gas. Volume DBD: A gas-gap separates two dielectric barrier covered electrodes, forming a plasma within the gas-gap.)[8] The benefit of the surface DBD is its reduced driving voltage and power requirement, due to the reduced discharge distance between the electrodes ~10 μm rather than ~1 mm), requiring a lower breakdown voltage based off the Paschen curve relationship.[167] The upper and lower electrodes are arranged in an overlapping hexagonal pattern with feed gas flowing through holes inside each hexagon, normal to the surface of the electrodes, as shown in FIG. 48. This pattern serves to distribute the plasma over a large cross-sectional area of the feed gas. A hydrophobic membrane, separating the water and discharge cell, minimizes the plasma-water

separation to bring the source of free-radicals within millimeters of the water surface without risking a short. The filter distributes bubbles over the membranes area to increase the water-gas surface area.

This method is constructed for a small-scale portable water treatment system to process laboratory waste, making the reduced power system requirements more attractive. This study analyzes the parameter space - treatment time, gas flow rate, contaminant concentration, plasma-to-filter distance, and treatment volume - to optimize for the maximum degradation. The degradation and efficiency performance is compared with other MB plasma treatment systems found in literature.

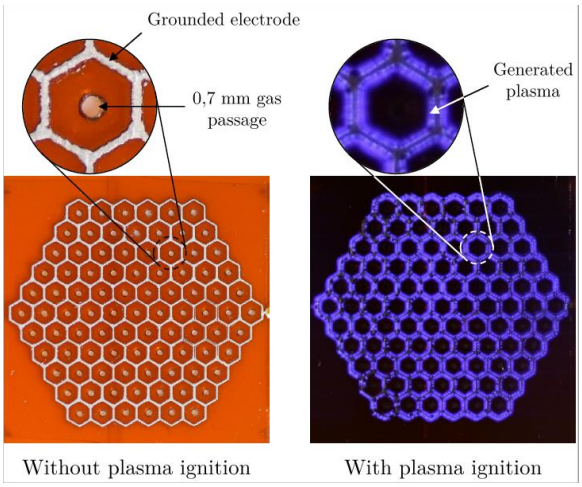

FIG. 48: Porous surface DBD plasma generator

8.3.1 Setup

The experimental setup for the plasma microbubble generation consists of the plasma bubble reactor, the high voltage power supply system and the air supply system, schematically depicted in FIG. 49. The plasma bubble reactor has a fully sealed air intake enclosure that bubbles into a solution container, which are separated and sealed by a sandwich design of a porous surface DBD plasma source and a hydrophobic PTFE membrane of pore size 0.2 μm (Sartorius Hydrophobic PTFE Membrane Filters Type 11807). Plasma is generated on the porous surface DBD plasma source in the region between plasma source and membrane. The inflowing air in the bottom enclosure forces reactive species generated in the plasma through the membrane and into contact with the water, via bubbles. FIG. 48 shows a

schematic of the porous surface DBD plasma generator. Both the high voltage and grounded electrode are printed on dielectric substrate (Kapton, 75 μm thick) using conductive ink (Conductor Flex-2 ink, Voltera). The printed electrodes are cured at 160 °C for 30 minutes to achieve full strength and conductivity. An orifice with a 0.7 mm diameter is drilled into the surface DBD plasma source to allow air to pass through normal to the surface.

The porous surface DBD plasma source is powered by a high voltage power supply constructed from the series arrangement of a sinusoidal waveform generator (AD9850 DDS Signal Generator), an audio power amplifier (Kemo M034N, 40 Watt), and two 1:100 turn ratio high voltage transformers (ET/UNI-05 from Express Transformers & Controls Ltd.). The amplitude of the function generator signal controls the high voltage signal output, which ranges up to 4.5 kV. The frequency of the signal remains constant for this study at 6 kHz. The electrical characteristics of the porous plasma sources are monitored using a high voltage probe (UoS: P6015A, Tektronix / UIUC: PVM-5, North Star) for the applied voltage and a Rogowski coil (UoS: Model 6585, Pearson Electronics / UIUC: Model 4100, Pearson Electronics) for the current. The air supply system consists of a mass flow controller (MC-series, Alicat Scientific) providing an air flow rate ranging from 0 to 12 slpm.

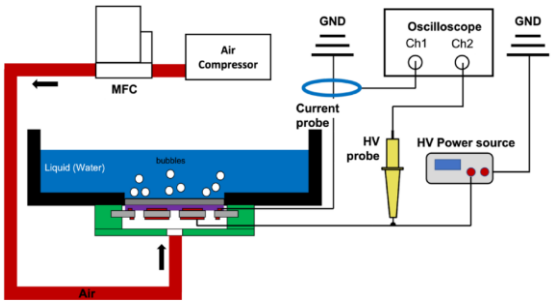

FIG. 49: Schematic of experimental test setup

8.3.2 Parameter Studies

The decontamination performance of the plasma microbubbles can be affected through various parameter: treatment time, air flow rate, distance between discharge electrode and water surface, initial MB concentration, and the treatment volume. The performance is evaluated in this study by measuring

the percent degradation after 5 minutes of treatment, except for the time study which only evaluated the percent degradation for each time step. Table 3 lists the chosen parameters and the respective variation of the values along with a note of which group (UoS and/or UICC) carried out the respective test. For each parameter a baseline value (highlighted in bold font) is chosen, and were the values held fixed when the respective parameter was not being tested. Through this study, the effect of the parameters on the degradation efficiency can help clarify the governing mechanics of the treatment process.

Table 3: Parameter values used for each parameter study. The bold values are the parameter values when that parameter is not being tested.

Parameters	Values	Group
Treatment time [min]	1, 3, **5**, 7.5, 10	UoS, UIUC
Air flow rate [slpm]	0, 0.5, 1, **2**, 2.5, 3.5	UoS
Distance [mm]	0.9, 1.7, 2.5, 3.4, **4.5** 1.9, 3.7, 6.5, 9.2, 12	UIUC
Concentration [mg / 100 ml]	0.1, 0.25, 0.5, 0.75, **1**	UoS
Treatment volume [ml]	15, **25**, 35, 40, 50	UIUC

8.3.2.1 Effect of Treatment Time

The degradation efficiency of a varying treatment time is analysed for times between 1 minute and 10 minutes. FIG. 50 shows the MB solution in vials after each treatment time, compared with the untreated and clean water samples. As can be seen, the color intensity of the MB samples reduced with increasing treatment time. For the maximum tested treatment time of 10 minutes, a strong reduction is achieved, with only faint coloration remaining. The degradation efficiency is quantified through absorption spectroscopy. FIG. 51 shows the degradation efficiency calculated from the measured absorbance for the MB samples of varying treatment time. As can be seen, the degradation efficiency increased significantly for small treatment times, reaching values of $\eta > 80\%$ within 3 minutes. With increasing treatment time, the degradation efficiency increases further, achieving 96% with a treatment time of 10 minutes. The achieved degradation efficiency of UoS and UICC fall within the same range,

where small discrepancy are likely related to the different absorption spectroscopy system. The change in time is clearly an exponential relationship as a function of time.

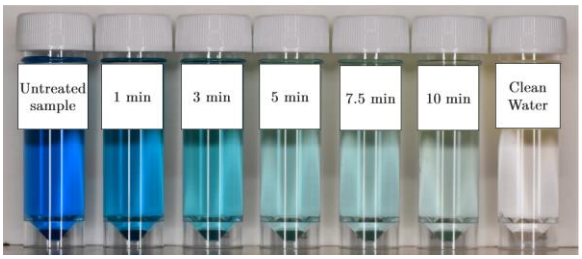

FIG. 50: Photos of test samples used for Treatment Time parameter study.

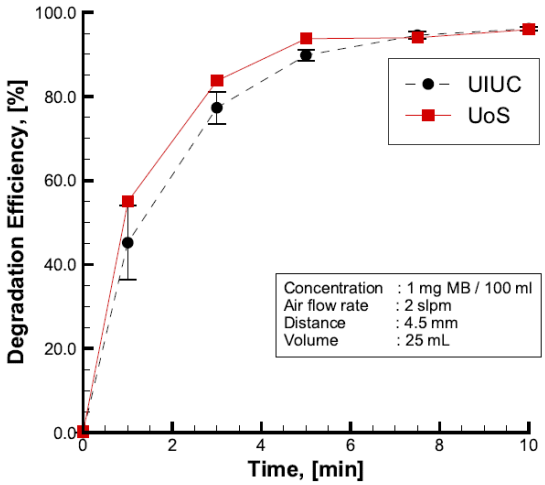

FIG. 51: Effect of treatment time on degradation efficiency

8.3.2.2 Effect of Air Flow Rate

FIG. 52 shows the MB samples treated with varying air flow rates, ranging from 0 slpm to 3.5 slpm. An air flow rate of 0 slpm results in no generation of microbubbles and no reduction in color intensity. Once the air flow rate is increased, a few microbubbles start generating and a reduction in color intensity is visible. With increasing air flow rate, the color intensity is further reduced. FIG. 53 shows the degradation efficiency for a varying air flow rate. As can be seen, the degradation efficiency remains low at 0 slpm and jumps to $\eta > 80\%$ when microbubbles are introduced at an air flow rate of 0.5 slpm. This demonstrates that the presence of microbubbles is necessary for an effective decontamination procedure. For higher air flow rates, the number and size of generated bubbles increases, resulting in a larger

absolute contact area between the plasma active species and the MB solution. The flow rate also carries additional ozone to the treated solution volume. Consequently, the degradation efficiency increases for larger air flow rates. When the air is flowing, the degradation efficiency achieves a positive linear trend with flow rate.

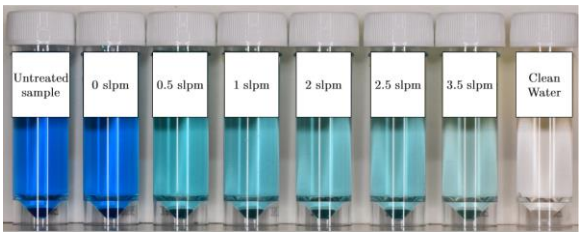

FIG. 52: Photos of test samples used for Flow Rate parameter study.

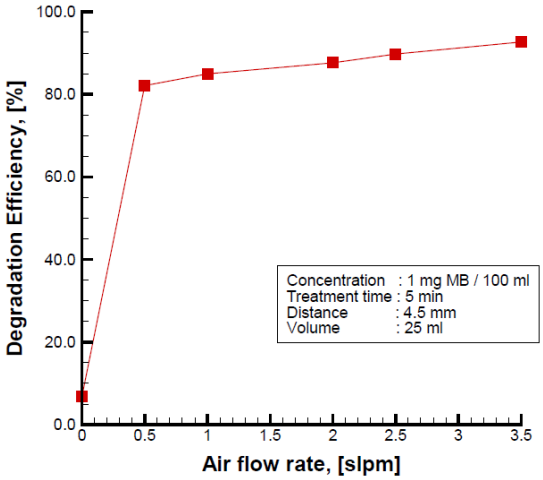

FIG. 53: Effect of air flow rate on degradation efficiency

8.3.2.3 Effect of Initial MB Concentration

FIG. 54 shows different MB samples with varying concentration ranging from 0.1 mg MB / 100 ml up to 1 mg MB / 100 ml before and after a 5 minutes treatment with plasma microbubbles. As can be seen, all different concentrating levels show a significant reduction in colour intensity after the treatment. FIG. 55 shows the obtained degradation efficiency for the samples of varying initial MB concentration. The degradation efficiency holds a constant value around 90%, making the degradation efficiency independent of the MB concentration.

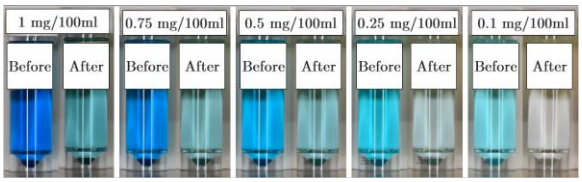

FIG. 54: Photos of test samples used during MB concentration parameter study.

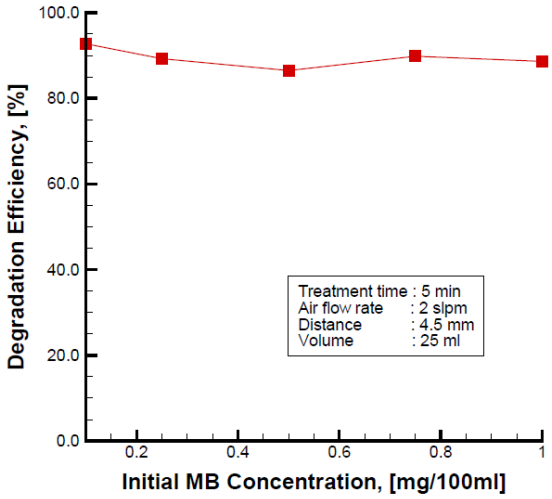

FIG. 55: Effect of initial MB concentration on degradation efficiency

8.3.2.4 Effect of Distance Between Electrode and Membrane

FIG. 56 shows the degradation efficiency for varying distances between the porous plasma source and the filter membrane. The two data sets are from variations using two different types of rubber gaskets with different thicknesses (0.95 mm and 1.8 mm). As can be seen, the degradation efficiency remained relatively constant with increasing distance, up to 1.1 cm. The added distance did not impact the recombination of active species before injection into the treatment solution. The ~5% reduced performance of the 1.8 mm rubber from the 0.95 mm rubber is suspected to be due to the less effective seal, allowing feed gas to inject in the water without passing through the plasma source. At small distances between electrode and membrane, the PTFE membrane can experience damage. A damaged membrane can results in a reduced performance due to a changed permeability of the membrane.

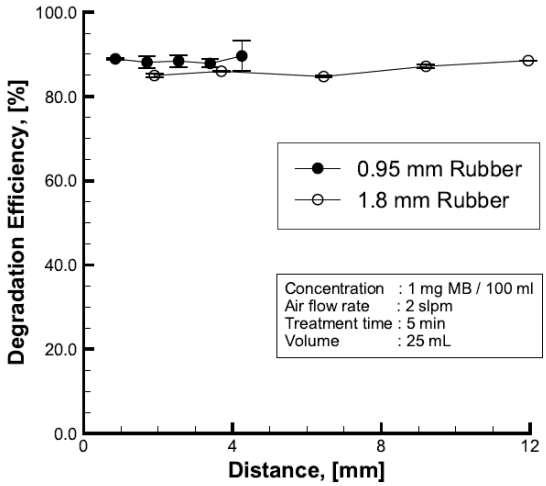

FIG. 56: Effect of distance between electrode and membrane on degradation efficiency

8.3.2.5 Effect of Treatment Volume

FIG. 57 shows the degradation efficiency for varying volumes of the sample solution. As can be seen, the degradation efficiency decreased with an increasing treatment volume. A linear trend gives a decreasing 4% MB degradation efficiency per 10 ml increase of treatment solution. The linear relationship suggests that the total treated MB quantity is directly dependent upon the water volume, which directly increases the quantity of MB. So although the degradation efficiency decreases by 14%, the total MB at that concentration increases by 333%. There is more MB being treated with increase water volume.

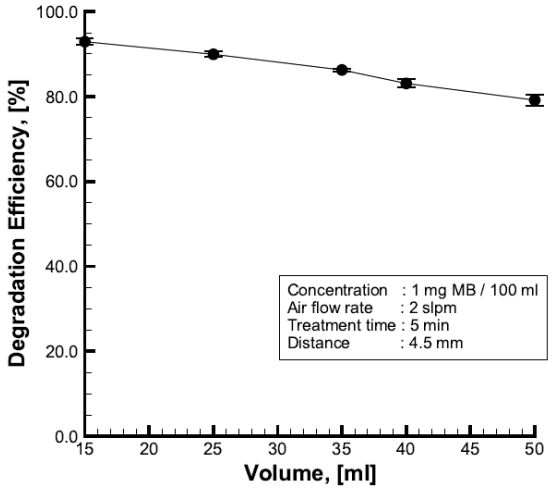

FIG. 57: Effect of treatment volume on degradation efficiency

8.3.2.6 Effect of Recycled Gas

A closed air loop tested if recycled ozone improved the reaction efficiency. Not all the ozone is absorbed by the water as it bubbles through the MB solution. This off gassed ozone represents waste in the system. By feeding the gas back through the system, the expected outcome is to increase the concentration of ozone in the feed gas. The diffusion rate of ozone into water is dependent upon the concentration of ozone in the feed gas, as discussed in Section 8.1. By increasing the ozone concentration, more ozone would diffuse into the water and increase the degradation efficiency at the 5 min mark. To test this idea, the bubbling chamber was sealed at the top with a tube attachment. A DC air pump fed the bubbling gas back into the discharge chamber. The flow control was place on this gas line leading from the pump to the discharge chamber to maintain the same flow rate of 2 slpm..

After discharging 25 mL, of 1 mg/ 100 mL MB concentration, for 5 min, the degradation efficiency was 44.4%. Compared with the 85% degradation efficiency from the previous tests, this represents a significant decrease. Recycling the feed gas is detrimental to the treatment process. The working rational for this result is that the ozone is used by the treatment process and trapped in the solution. As the oxygen is used up, its concentration is not replenished in the feed gas. The reduced concentration of oxygen produces less ozone in the feed gas, reducing the diffusion of ozone into the

water, and eventually all the oxygen (as well as ozone) will be used up within the feed gas. There may be an initial heightened concentration of ozone, but at the 5 min mark, this benefit has disappeared and the closed loop becomes a detriment to the degradation efficiency.

8.3.2.7 Effect of Solution Depth

Three different container cross-sections were investigated to determine the effect of MB solution depth for the standard 25 mL volume. The original container has a 4x4 cm^2 cross-sectional area, for a depth of 1.5 cm. A smaller cross-sectional area, formed from a tube with a diameter of 22 mm, has a depth of 6.5 cm. A larger cross-sectional area of 7x7 cm^2 has a depth of 0.5 cm. The tests used the standard 1 mg / 100 mL concentration of MB, a treatment time of 5 min, an air flow rate of 2 slmp, and a 4.2 mm distance between the electrode and filter.

The results, presented in Table 4, show a decrease in performance for both alternative container sizes. For the smaller tube container, the bubbles had farther to travel along the 6.5 cm depth. However, the collection of bubbles came together as a uniform surface that stretched across the entire cross-sectional area. This may have reduced the gas-liquid surface area as part of each bubbles volume was taken up by the wall of the tube. The reduced surface area would then have reduced the diffusion of ozone into the MB solution. This, however, must be balanced with the greater distance and so time that the bubbles exist within the MB solution along their extended path. The larger container only had bubbling in the center of the MB solution. This would reduce the mixing of the solution during treatment. The path was also a third of the original distance, reducing the time for ozone diffusion into the MB solution. It appears that there is an optimal container cross-sectional area that is near the size chosen for this setup.

Table 4: Degradation efficiencies for cross-sectional area

Setup Condition (Height / Area)	Degradation Efficiency [%]
0.5 cm / 7 x7 cm2	45
1.5 cm / 4 x 4 cm2	85
6.5 cm / 3.8 cm2	79

8.3.3 Discussion

The effects of the different parameters on degradation efficiency collectively suggest that the amount of ozone is the mechanism controlling the degradation rate. Both the electrode-filter distance and the MB concentration study have no noticeable impact on the degradation rate where as the water volume and the air flow rate have linear trends. These relationships suggest that the air-water volume ratio plays a significant role in the reaction rate of the treatment process and weighted towards a larger air-water volume ratio. The yield energies from other published works support this observation.

The lack of change to the degradation efficiency from the filter-electrode distance study, presented in FIG. 56, identifies the long-lived ozone rather than other short lived nitrogen and oxygen species as the dominant oxidative species created by the plasma generator. The transfer time of the reactive species between the porous plasma generator and the filter membrane, with a 1 mm separation, is approximately 21 ms. This estimate is based on the 2 slpm flow rate and the 30 mm diameter cross-sectional area of the feed gas orifice into the water. The oxygen species involved in the degradation process are either the relatively long lived ozone, with a half-life up to a day[168] in air, or the shorter lived atomic oxygen and NOx species that are 8 orders of magnitude below ozone after 1 μs of leaving the discharge, according to kinetic simulations by Riccardi and Barni.[15] This simulation was of an atmospheric DBD plasma with an electron density of 10^{21} m^{-3}, characteristic of filament DBD plasmas.[103] The transfer time between the plasma and water surface is too long to maintain a significant amount of plasma generated free-radicals, so ozone is the primary reagent for the degradation of MB.

The lack of change to the degradation efficiency by the MB concentration, presented in FIG. 55, makes it appear that the concentration does not affect the reaction rate. However, it is important to recall that the degradation efficiency is normalized by the varying initial concentration for each test. So although the initial concentration is decreasing, the final treated amount has also proportionately decreased. The trend identifies a first order exponential decay where the reaction rate is proportional to the quantity of reactants and maintains rate constant. The reaction rate is dependent upon the

concentration of the reactive species, both the MB and the ozone. An increase in MB will increase the reaction rate, degrading a larger amount of MB over the same amount of time.

The flow rate parameter, presented in FIG. 53, and the water volume parameter, presented in FIG. 57, exhibit opposing linear trends. Both of these parameters effectively change the ratio of air to water present in the reaction, over the total treatment time. The two trends are compared in FIG. 58 by converting their respective dependent variables to a volume ratio of the air to water. The flow rate of the feed gas is converted to volume of air per total reaction time. The time parameter trend, presented in FIG. 51 also has its dependent variable converted to the air-water volume ratio by analyzing the 2 slpm flow rate over the treatment time at each data point. Although the three trend lines have different power dependencies, their trends lie along a similar linear relationship between air-water volume ratios of 300 and 700. The consistency, when converted to the air-water volume ratio, suggests that the ratio of ozone to MB solution is the primary mechanism for increasing the degradation efficiency. The improved degradation efficiency can be explained by the effective increase in the amount of ozone, which increases the reaction rate without adding additional MB to be treated.

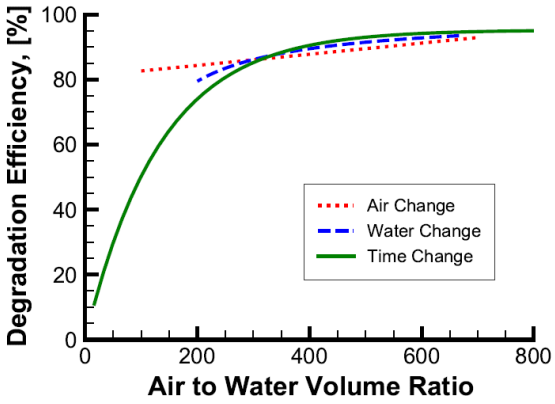

FIG. 58: Effect of treatment volume, time, and flow rate normalized to the volume ratio of air to water

The effectiveness of different plasma treatment systems is typically measured by the yield energy Y_{energy}, which is defined by the total MB mass treated per total treatment input energy as:[153]

$$Y_{energy} = \frac{\Delta C \cdot V}{P \cdot \Delta t} \qquad \text{Eq. 34}$$

where ΔC is the change in concentration, V the volume, P the power and Δt the treatment time. The yield energy of this work is 0.45 g/kW•hr at 25 ml of 1 mg / 100 ml methylene blue treated over 5 minutes for a 92% degradation and is shown in comparison with other works from literature in FIG. 59. Each value is associated with a respective reference number. Two configuration categories are also identified: 1) the proximity between the plasma discharge and the water surface (A: at a distance; B: at water surface; C: in bubbles) and 2) the mixing method of the MB solution during treatment (a: no mixing; b: Bubbles; c: Surface flow). These two categories affect the two previously discussed dependencies of the reaction: the presence of free radicals in the reaction, and the quantity of reactive species. The proximity affects the number of free radicals in the system, as the plasma adjacent to the water surface can introduce short lived species into the water. The mixing method affects the volume ratio of ozone to the reacted MB solution, as this determines the volume of ozone within the reaction chamber.

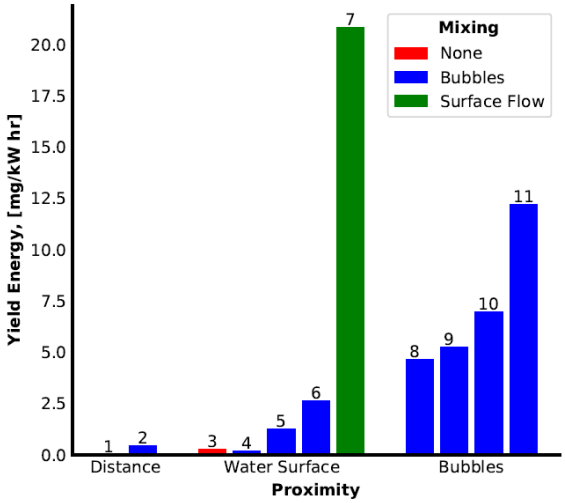

FIG. 59: Yield energies reported by other authors with different MB Plasma Water Treatment configurations. Proximity of plasma to water: at a distance, at water surface, in bubbles. Mixing method: no mixing, bubbles, or surface flow. Reference association: #1[156], #2 (This work), #3[148], #4[144], #5[155], #6[142], #7[145], #8[146], #9[147], #10[143], #11[157]

The dominant treatment methods are those that produce the plasma within bubbles, where the plasma has direct contact with the water surface. In close proximity to the surface, the short lived free-

radicals can directly enter the water and enhance the production of hydroxyl while reducing the energy waste from recombination, that normally occurs at a distance from the water. The one exception is #7[145], the example of surface flow mixing, where a laminar fountain of water is exposed to a volume discharge at the water surface. For this case, the total air-water volume ratio is closer to 50% compared to bubbled systems where the ozone takes up a much smaller volume of the total reaction volume. From FIG. 58, the increased air-water volume ratio increases the MB reaction rate. Increasing the reaction rate, decreases the treatment time, and reduces the total energy consumption.

The yield energy performance of this setup, using a bubbled surface DBD plasma system, is the fourth lowest out of the total reviewed examples in FIG. 59. One reason is the proximity distance of the plasma from the water surface. Although the distance between the plasma and the water can be as small as 1 mm, the performance enhancing free radicals of the plasma discharge degrade over this distance for a typical gas velocity. Instead, the advantage of this system is its lower discharge voltage (2 kV) due to the thin surface DBD. Although, the reduced power is not enough to compensate for the lack of direct water surface contact in the yield energy, it does reduces the power supply hardware requirements and size. The system is then more compact and portable than other plasma treatment methods, making it a viable laboratory decomposition device for contaminated solutions.

8.4 Misting Nozzle DBD

8.4.1 Setup

The discharge approach used in this study is a volume DBD, formed within a misting spray of MB. (Volume DBD: A gas-gap separates two dielectric barrier covered electrodes, forming a plasma within the gas-gap.)[8] The benefit of the misting spray is the increased surface area per unit volume of water to promote ozone diffusion into the water, as discussed in the Section 8.1. A single misting nozzle is tested by spraying into a tube. The nozzle is inserted into an acrylic tube to catch the spray and form the dielectric barrier, as shown in FIG. 60b. A loop of copper tape is fixed 4.8 mm downstream of the nozzle around the outside of the tube. The copper tape serves as the high voltage electrode while the brass nozzle

serves as the grounded electrode. The mist spreads out in a cone of approximately 40°, FIG. 60. The MB solution drains into a beaker where a pump (12V DC pump with a max flow rate of 70 ml/min) feeds the solution back into the nozzle. In this way, the entire MB solution is cycled through the discharge regime during the processing time.

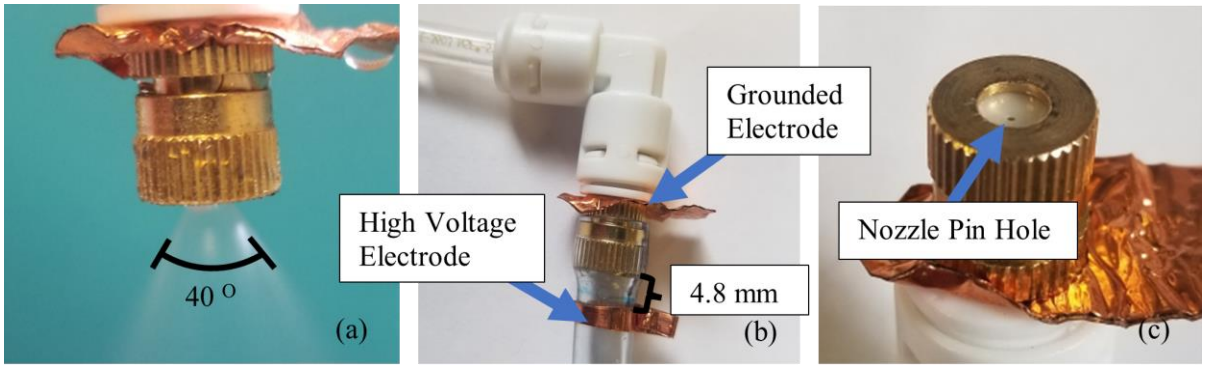

FIG. 60: Image of misting nozzle and DBD electrodes. (a) Active misting of nozzle with a 40° spread angle. (b) Single nozzle inserted into an acrylic tube for initial test. (c) Close up view of nozzle face and pin hole.

To examine the effect of increasing the treated water volume per unit time, a second test setup utilizes multiple nozzles to treat the MB solution. The brass misting nozzle again creates the grounded electrode, impinging on a glass (dielectric) surface with a copper tape backing to create the high voltage electrode, as depicted in FIG. 61. The mist has an approximate distance of 2 mm from the dielectric surface. The dielectric surface is 1.5 mm thick. The misting cone also serves as a partially conducting path for the current. The relative dielectric of deionized water is 80, proportionately decreasing the drop in the electric field relative to the same space filled by air. So, the misting cone significantly decreases the electric field drop between the nozzle and the dielectric surface. The decreased field drop allows for a lower discharge voltage of 13 kV than if the 2 mm gap separating the nozzle and glass surface were filled with air.

FIG. 61: 3D Printed volume for testing multiple nozzles to treat MB solution.

The discharge setup uses a 3D printed volume container to mount multiple nozzles that impinge upon a glass beaker placed inside the printed volume, as shown in FIG. 61, with the beaker removed from the printed volume. A strip of copper tape fixed to the inside of the glass beaker serves as the high voltage electrode. Alligator clips attach to extended strips of copper tape on the beaker strip and on each nozzle to connect the electrodes to the driving voltage. The 3D printed volume funnels the MB solution down to a tube to a pump that feeds the nozzles. Originally the setup was designed for six nozzles but the pump could only supply enough pressure for 3. The glass beaker is kept a uniform 2 mm from the edge of the face of the nozzles by uniform layers of Kapton tape around the top of the beaker. Cut-out section of the Kapton tape ring allow fresh air to replenish the oxygen for producing ozone in the reaction region.

A larger driving voltage supply is required for this volume discharge with a discharge gap in the millimeters vs. a surface discharge gap in the micrometers. The driving voltage signal is created by a Rigol DG-1022 Function Generator. The power for the discharge is supplied by a Crown Macro-Tech 1202 Audio Amplifier. A Corona Magnetics 5525–2 Transformer with a turn ratio of 1:357 increases the signal to the driving voltage.

8.4.2 Results

The single nozzle and tube set-up was meant to test how increasing the surface area to volume ratio would affect the efficiency of plasma water treatment. The discharge was observed to weakly occur around 8-10 kV. Of note was that the discharge did not initiate without the water flowing. The misting

appears to create a decreased discharge path, through the dielectric of the deionized solution. After 5 minutes of treatment at 10 kV, the solution only degraded by 6.3%. This is most likely due to the weak discharge as well as the time the solution is exposed to the ozone. In the bubbling treatment method, the MB solution is continuously treated in the treatment container. The bubbling ensures that liquid at the exterior of the contain is constantly cycled to the bubbling ozone region. In the spraying method, the solution is only treated during the time it is physically between the discharge electrodes. As the volume is pumped through the nozzle, the entire volume is treated in cycles. The total treatment time per volume is 12 s/mL with a volume of 3.8μm being treated at any one time.

Since the water is only treated while it was in the misting cone, the second set up with multiple nozzles was expected to decrease the treatment time. The final set-up ended up only utilizing 3 of the 6 attached nozzles, due to a nozzle clog and a limited pumping pressure. The discharge was operated at 13 kV. After 5 minutes of treatment, the solution degraded by 32%. The increased degradation is due to the increased voltage, impingement on a dielectric covered electrode normal to the flow, a reduced distance between the high voltage electrode and nozzle, and the number of nozzles. After 10 minutes of treatment, the solution degraded by 43%. This is still a significantly lower performance than the bubbled surface discharge setup, with an 85 % degradation after 5 min. However, in this case of the misting treatment, only 0.015% of the liquid is present within the treatment region whereas all of the MB solution is within the treatment region of the bubbling cup.

If the percentage of liquid present within the discharging nozzle region could be increase to a significant fraction of the total liquid volume, the processing time is expected to significantly decrease. This could be accomplished by utilizing more nozzles. Alternatively, the electrodes could be placed in such a way that it would extend the length of the ozone/misting region. This would increase the area-to-liquid volume ratio as well as the treatment time. If the length of the discharge was long enough, there would be no need to cycle the solution. The entire liquid volume would be continuously treated for the time it exists within the tank while maintaining the advantage of misting. One concept could have a

vertical coaxial volume with gas pumped upward at a two-phase velocity to create misting flow. The electrodes would be placed along the center and exterior of the coaxial volume. The electrodes would form a volume discharge along the entire length of the treatment volume. The liquid could then mist upwards until it condenses on the walls where larger droplets are pulled back down by gravity.

9 Conclusion of Plasma Water Treatment Work

We have developed a plasma microbubble generator for the decontamination of liquids. We have quantified the performance of the plasma microbubble generator for various design and operating parameters. The feasibility study has found the treatment time to be the dominant parameter to affect the degradation efficiency, where a degradation efficiency of over 90% was achieved after a treatment time of 5 minutes. A varying initial concentration of the MB solution found no influence on the degradation efficiency, characteristic of an exponential degradation. The varying distance between the plasma source and membrane found no influence on the degradation efficiency, suggesting that only the ozone and not the shorter lived free radicals survive long enough to enter the water. The varying solution volume found a linear decrease in degradation efficiency with increasing volume, but there was an overall increase to the treated MB mass, suggesting that the reaction rate increased with the increase MB in the system. The varying air flow rate found a linear increase in degradation efficiency with increased air flow, suggesting that the added ozone increased the reaction rate of degradation. The recycled feed gas showed a decrease in degradation efficiency, suggesting that the oxygen for producing ozone is depleted in a closed system. The varying MB solution depth found an optimum at the current solution depth of 1.5 cm and a significant decrease in performance at a shallower depth of 0.5 cm. The collection of degradation efficiency trends and review of literature yield energies suggest that a larger air-water volume ratio is the primary driving mechanism of performance, as it introduces a larger ratio of ozone to MB in the reaction, increasing the reaction rate of the system. The parameter study has demonstrated the performance of the plasma microbubble generator for the decontamination of liquids. It has shown how its operating parameters can be optimize to improve the MB degradation performance, and identified the total amount of reactant as the primary driving mechanism of the reaction rate.

A nozzle misting setup investigated the performance change from increasing the gas-liquid surface area-per-liquid volume. The intended effect was to increase the ozone diffusion into the MB solution. The performance of a single nozzle had a degradation efficiency of 6.3% compared with the

85% of the bubbling system, for the same treatment time. However, the small size of the discharge region within the misting jet meant that only 0.015% of the 25 mL MB solution was under treated at a time. By increasing the number of misting nozzles, the degradation efficiency increased to 43%. It is expected that a further increase of the number of misting nozzles would further increase the degradation efficiency, potentially beyond that of the bubbling system.

10 Future Works

So far what has been demonstrated for the PPC is digital control of individual plasma columns in a DBD PPC and a tuning method that provides expanded bandgap tuning in simulations. Further experimental advances should focus on fully implementing this method, validating the microwave performance of the physical PPC, measuring the plasma density to accurately predict the bandgap performance, and working towards high power microwave applications. Further simulation work can expand the PPC performance beyond bandgaps to include a negative index of refraction or estimate the microwave power at which the PPC configuration begins to be affected.

10.1 Fully Integrated PPC

To complete the digital integration of the PPC, the fixes from Section 6.5 need to be implemented. To address the conductive hydrocarbon build-up on the dielectric surface, the frame of the PPC must be changed to a ceramic, such as MACOR.[126] To address the electromagnetic interference that affects the microcontroller, the microcontroller must be shielded in a metal container. To address the capacitive cross talk between the wires leading from the control circuit to the pins, the wire insulation must either be increased to maintain the 3 mm pin separation, or the wires can be replaced by PCB traces between the pin electrodes and biasing control circuit. After the microcontroller has been successfully implemented, a computer interface would provide the desired active control capabilities.

10.2 Microwave Measurements

The plasma structure cannot truly be considered a PPC without demonstrating its capability to produce the characteristic bandgaps of a PPC. For this reason, microwave tests are required to validate the bandgap performance. In addition, there are several questions about the PPC that microwave tests would clarify: 1) Does the measured bandgap agree with the PWE predictions for a known plasma density distribution? 2) If not, can the error be explained by an error in the plasma density estimate? 3) Will the bandgap change as expected when the PPC is tuned? 4) Does a part of the tuning mechanism (pin array,

biased voltage, surrounding structure, etc.) interfere with the bandgap performance? 5) What is the time dependence on the bandgap due to the plasma's 3.2 kHz cycled DBD nature?

Previous researchers, discussed in Section 1.4, have made microwave measurements using vector network analyzers (VNA) to perform a frequency sweep and determine the frequencies that are blocked by the PPC. The microwaves are launched from a horn antenna, the frequency transmission on the opposite side is received by a mirrored horn antenna, and the output and input signal are measured by the VNA. Metal sheets with apertures the size of the PPC cross-section block microwaves from transmitting around the plasma structure. The range of reflected frequencies is the bandgap. Disadvantages to this approach are the availability of equipment in the hundred GHz range and the sensitivity of the equipment at these frequencies.

Since the PPC bandgap frequency can be lowered by reconfiguring the PPC, as discussed in Section 3, the 1 mm lattice constant PPC from this work can be evaluated at low GHz and high MHz frequencies by increasing the lattice constant and super radius. A signal produced and recorded by the VNA in the time-domain can determine the effect of the DBD cycle on the bandgap. If the reflection coefficient of an input signal changes over the period of the DBD cycle, then there is a temporal effect from the time dependent plasma.

An estimate for the plasma density can be made by the VNA measurements. The upper limit of the TE_0 bandgap, measured by the VNA frequency sweep, is roughly set by the area averaged plasma frequency ($\omega_{p\ avg}$). The normalized plasma distribution over this area can be approximated by the light distribution ($f(x,y)$) from a side view of the PPC, as shown in FIG. 62. The light intensity has been suggested to be proportionate with the electron density distribution.[111] The peak plasma density ($n_{e\ max}$) is then solved using Eq. 36. The term inside the integral defines the plasma frequency distribution.

$$\omega_{p\ avg} = \iint \sqrt{\frac{e^2 n_{e_{max}}}{\varepsilon_o m_e}\left(\frac{f(x,y)}{f(x,y)_{max}}\right)}\, dxdy \qquad \text{Eq. 35}$$

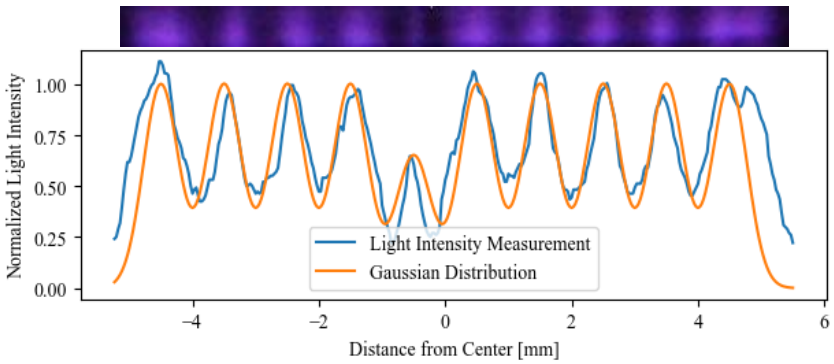

FIG. 62. Light intensity distribution along the midline of the DBD side view photo. The sum of adjacent Gaussian functions, centered at each filament location, are overlayed as the Gaussian Distribution of each plasma column. All pins along the fifth row from the left are biased by a 15MΩ resistor.

10.3 Non-Linear Effects at High Power Microwaves

In this work, the plasma permittivity is for a cold plasma with no magnetic field. This assumption holds for low power microwaves. However, for HPM applications, the large electric fields of the incident wave can enhance the applied electric field formed by the electrodes so that the plasma density is a function of both the applied field and wave field. At such large electromagnetic fields, non-linear effects should be expected. The plasma distribution can be a function of both the incident power and time as the plasma distribution evolves due to the incident wave.

To address the power dependence when there is no time dependency, the PPC can be characterized for different power levels at different frequencies. The bandgaps are then not only a function of frequency but also the incident power. By mapping this information, prior to operation, the necessary bandgap settings can be preprogrammed by the digital control system. This process is performed for common circuit components when measuring their non-linear X-parameters.

For non-linear effects that are time dependent, a feedback loop can be incorporated into the discharge control system. The input for the feedback would be the light intensity viewed through the conductive glass plate. As stated in Section 10.2, light intensity can be correlated to the electron density. The desired electron density distribution would then be manipulated by increasing or decreasing the applied electric field at the individual electrodes to compensate for the fields of the propagating wave.

To identify the incident microwave power level for which the PPC begins to experience a non-linear effect, a looped simulation between a plasma model and wave model can be implemented. The PWE method is combined with a simplified plasma model that includes ionization, recombination, and diffusion. An applied electric field, fed into the plasma model, defines the initial desired plasma distribution of the PPC. The PWE method is then used to calculate the electric field distribution of the incident wave. The sum of the incident wave and applied electric fields are fed back into the plasma model to update the plasma distribution. This cycle is repeated until it either diverges or reaches an equilibrium. Incident wave power levels that diverge identify are power levels at which the incident wave begins to impact the PPC configuration and must be accounted for by adjusting the applied electric field as described in the previous two paragraphs.

10.4 2D Plasma Metamaterial

Simulations of the complex structures discussed at the end of Section 3.3, could demonstrate a 2D plasma metamaterial with a tunable negative index of refraction. Electromagnetic radiation simulation software, such as ANSYS HFSS, can simulate the S-Parameters through a single periodic element. These S-Parameters can then be converted to a complex permittivity and permeability, as presented by Feng.[169] The goal should be to demonstrate an index of refraction with a value of negative one, along plane of periodic elements.

A 2D plasma metamaterial could be formed by a ring of plasma columns with rows of plasma columns on either side. The plasma frequency of the columns forming the ring would need to be slightly above the operating frequency to form plasmons around the columns so that the ring acts as a conductor with capacitive gaps between columns. The conductive and capacitive elements of the ring then form a resonant structure for a magnetic field applied perpendicular to the plane of the ring. A negative permeability would occur slightly above the resonant frequency. The rows of plasma columns change the permittivity of the structure, affecting the electric field oriented parallel to the 2D plane. The area average of the plasma permittivity from the ring columns and the side row columns determines the total average

permittivity. With a sufficiently large enough plasma frequency in the side row columns, the average permittivity is tuned negative at a frequency where the permeability is also negative. The combined parameters will produce a negative index of refraction. To act as a metamaterial and have these conditions take effect, the incident wavelength must be far larger (at least 5 times) than the unit cell containing an individual ring of columns.

10.5 Water Treatment

The misting nozzle treatment method showed a significant increase in degradation efficiency between one and three nozzles. The next step would be to experimentally determine a relationship between the number of nozzles and the yield energy. Increasing the number of nozzles is expected to decrease the necessary treatment time to achieve at least a 90% degradation efficiency, increasing the yield energy. The relationship between the number of nozzles and yield energy may approach a limit as the liquid outside the misting cone (pumping through the tubing or in the collection container) approaches zero. This limit would define the maximum yield energy of a fully misting system. The maximum yield energy from the misting treatment process could then be compared to the yield energies from other researchers.

Since these misting nozzles would be susceptible to clogging when treating wastewater, it is necessary to find a more robust method to suspend the liquid in a misting regime. The misting regime can be achieved by increasing the gas flow rate in a vertical pipe flow, as illustrated in FIG. 46. A pulsed gas flow in a vertical column would mist the liquid and allow gravity to pull the liquid back down to repeat the cycle. The problem of keeping the liquid in the loop while feeding high velocity gas would need to be solved. If the container is formed by a dielectric coaxial tube pipe, isolated center and external conductors could produce a discharge voltage across the misting volume. During the initial misting jet test of this work, discharge current spikes (indicative of plasma discharge) were observed at lower voltages when the jet was spraying than when the jet was off. This observation was assumed to be due to the reduced voltage drop across the water droplets which have a relative permittivity of 80. A centimeter gap between the

inner and outer dielectric may be possible for a driving voltage around 20 kV. The increased volume would be advantageous for misting as water droplets would be more likely to build up on the dielectric surface of a narrow gas gap.

11 Professional Contributions

Journal Publications:

M.C. Paliwoda and J. L. Rovey, "Multiple Parameter Space Bandgap Control of Reconfigurable Atmospheric Plasma Photonic Crystal," *Physics of Plasmas*, 27, 023516, (2020)

M.C. Paliwoda and J. L. Rovey, "Intensity Control of Individual DBD Plasma Filament II: Fundamental Physical Mechanism," *Physics of Plasmas*, 24, 053505 (2017)

M.C. Paliwoda and J. L. Rovey, "Intensity Control of Individual DBD Plasma Filament I: Experiment with a Needle Electrode," *Physics of Plasmas*, 24, 053504 (2017)

H. Jakob, M.C. Paliwoda, J.L Rovey, and M. Kim, "Surface DBD Plasma Microbubble Reactor for Degrading Methylene Blue," *Physica Scripta* (Under Review)

M.C. Paliwoda and J.L Rovey, "Expanded Tuning of 2D Plasma Photonic Crystal Bandgaps by Localized Plasma Control" (Ready for submitting to journal)

Presentations:

M.C. Paliwoda, "Digital Control of Multiple Plasma Columns in a 2D Plasma Photonic Crystal," Directed Energy Student Workshop, DEPS, Virtual, (March 2021)

M.C. Paliwoda, "Plasma Photonic Crystals and the Tunable Parameters Control of the Bandgaps," OSA Photonic Metamaterials Technical Group (September 2020) - **Invited Webinar**

M.C. Paliwoda, "Periodic Filamentary Plasma Reconfigurable Metamaterial," Directed Energy Student Workshop, DEPS, West Point, NY (March 2020)

M.C. Paliwoda and J. L. Rovey, "Direct Position Control of Dielectric Barrier Discharge Filaments," SciTech AIAA Conference, San Diego, CA (January 2016)

12 Bibliography

[1] U. Kogelschatz, IEEE Trans. Plasma Sci. **30**, 1400 (2002).
[2] U. Kogelschatz, Plasma Chem. Plasma Process. **23**, 1 (2003).
[3] V.I. Gibalov and G.J. Pietsch, Plasma Sources Sci. Technol. **21**, 024010 (2012).
[4] L.B. Loeb and J.M. Meek, J. Appl. Phys. **11**, 438 (1940).
[5] J.M. Meek, Phys. Rev. **57**, 722 (1940).
[6] L.B. Loeb and J.M. Meek, J. Appl. Phys. **11**, 459 (1940).
[7] A. Von Keudell and V. Schulz-Von Der Gathen, Plasma Sources Sci. Technol. **26**, (2017).
[8] R. Brandenburg, Plasma Sources Sci. Technol. **26**, (2017).
[9] R. Tschiersch, S. Nemschokmichal, M. Bogaczyk, and J. Meichsner, J. Phys. D. Appl. Phys. **50**, (2017).
[10] H.T. Chen, W.J. Padilla, J.M.O. Zide, A.C. Gossard, A.J. Taylor, and R.D. Averitt, Nature **444**, 597 (2006).
[11] Y. Hao, B. Zheng, and Y. Liu, Phys. Plasmas **21**, 19 (2014).
[12] J.R. Roth, J. Rahel, X. Dai, and D.M. Sherman, J. Phys. D. Appl. Phys. **38**, 555 (2005).
[13] I. Adamovich, S.D. Baalrud, A. Bogaerts, P.J. Bruggeman, M. Cappelli, V. Colombo, U. Czarnetzki, U. Ebert, J.G. Eden, P. Favia, D.B. Graves, S. Hamaguchi, G. Hieftje, M. Hori, I.D. Kaganovich, U. Kortshagen, M.J. Kushner, N.J. Mason, S. Mazouffre, S.M. Thagard, H.R. Metelmann, A. Mizuno, E. Moreau, A.B. Murphy, B.A. Niemira, G.S. Oehrlein, Z.L. Petrovic, L.C. Pitchford, Y.K. Pu, S. Rauf, O. Sakai, S. Samukawa, S. Starikovskaia, J. Tennyson, K. Terashima, M.M. Turner, M.C.M. Van De Sanden, and A. Vardelle, J. Phys. D. Appl. Phys. **50**, (2017).
[14] K. Sandra, R. Priyadarshini, B. Nikita, and A. Peter, J. Phys. D. Appl. Phys. **45**, 125202 (2012).
[15] C. Riccardi and R. Barni, Chem. Kinet. (2012).
[16] U. Inan, A. Inan, and R. Said, *Engineering Electromagnetics and Waves*, 2nd ed. (Pearson Education Limited, Edinburgh Gate, 2016).
[17] M.A. (Michael A.. Lieberman and A.J. Lichtenberg, *Principles of Plasma Discharges and Materials Processing* (Wiley-Interscience, Hoboken, 2005).
[18] Y. Itikawa, J. Phys. Chem. Ref. Data **35**, 31 (2006).
[19] H. Ryzko, Proc. Phys. Soc. **85**, 1283 (1965).
[20] J.D. Joannopoulos, S.G. Johnson, R.D. Meade, and J.N. Winn, *Photonic Crystals : Molding the Flow of Light*, Second (Princeton University Press, Princeton, N.J., 2008).
[21] H. Benisty and C. Weisbuch, *Photonic Crystals* (Elsevier Masson SAS, 2006).
[22] M.A. Butt, S.N. Khonina, and N.L. Kazanskiy, Opt. Laser Technol. **142**, 107265 (2021).
[23] L. Zhang and J.T. Ouyang, Phys. Plasmas **21**, 103514 (2014).
[24] A.R. Weily, K.P. Esselle, and B.C. Sanders, Phys. Rev. E - Stat. Nonlinear, Soft Matter Phys. **68**, 166091 (2003).
[25] Q. Zhao, K. Cui, X. Feng, F. Liu, W. Zhang, and Y. Huang, Appl. Opt. **52**, 6245 (2013).
[26] B. Temelkuran, M. Bayindir, E. Ozbay, R. Biswas, M.M. Sigalas, G. Tuttle, and K.M. Ho, J. Appl. Phys. **87**, 603 (2000).
[27] Y. Zhang, G. Lu, and D. Zeng, Prog. Electromagn. Res. M **61**, 43 (2017).
[28] S.A. Ramakrishna and T.M. Grzegorczyk, *Physics and Applications of Negative Refractive Index Materials* (SPIE Press, 2009).
[29] H. Hajian, E. Ozbay, and H. Caglayan, Appl. Phys. Lett. **109**, (2016).
[30] Y. Wang, Z. Duan, F. Wang, S. Li, Y. Nie, Y. Gong, and J. Feng, IEEE Trans. Electron Devices **63**, 3747 (2016).
[31] J.S. Hummelt, S.M. Lewis, M.A. Shapiro, and R.J. Temkin, IEEE Trans. Plasma Sci. **42**, 930 (2014).
[32] D. Wang, F. Qin, S. Xu, A. Yu, and Y. Wu, AIP Adv. **5**, 027102 (2015).
[33] L. Moscardi, G. Lanzani, G.M. Patern, and F. Scotognella, Appl. Sci. **11**, 2119 (2021).
[34] L. Nucara, F. Greco, and V. Mattoli, J. Mater. Chem. C **3**, 8449 (2015).

[35] O. Sakai and K. Tachibana, Plasma Sources Sci. Technol. **21**, 013001 (2012).
[36] M.Y. Naz, A. Ghaffar, N.U. Rehman, S.A. Shahid, and S. Shukrullah, Int. J. Eng. Technol. **12**, 53 (2012).
[37] J.B. Pendry, A.J. Holden, W.J. Stewart, and I. Youngs, Phys. Rev. Lett. **76**, 4773 (1996).
[38] O. Sakai, T. Sakaguchi, and K. Tachibana, J. Appl. Phys. **101**, 073304 (2007).
[39] D. Wang, F. Qin, S. Xu, A. Yu, and Y. Wu, AIP Adv. **5**, 027102 (2015).
[40] B. Wang and M.A. Cappelli, Appl. Phys. Lett. **107**, 171107 (2015).
[41] B. Wang and M.A. Cappelli, AIP Adv. **6**, 065015 (2016).
[42] O. Sakai, J. Maeda, T. Shimomura, and K. Urabe, Phys. Plasmas **20**, 073506 (2013).
[43] Y. Wen, S. Liu, H. Zhang, and L. Wang, J. Phys. D. Appl. Phys. **51**, 025108 (2018).
[44] J. Faith, S.P. Kuo, and J. Huang, Phys. Rev. E **55**, 1843 (1997).
[45] S.P. Kuo and J. Faith, Phys. Rev. E **56**, 2143 (1997).
[46] O. Sakai, T. Sakaguchi, and K. Tachibana, J. Appl. Phys. **101**, 073304 (2007).
[47] T. Sakaguchi, O. Sakai, and K. Tachibana, J. Appl. Phys. **101**, 073305 (2007).
[48] O. Sakai and K. Tachibana, IEEE Trans. Plasma Sci. **35**, 1267 (2007).
[49] Y. Wang, L. Dong, W. Liu, Y. He, and Y. Li, Phys. Plasmas **21**, 2012 (2014).
[50] L. Dong, B. Li, N. Lu, X. Li, and Z. Shen, Phys. Plasmas **19**, 17 (2012).
[51] W. Fan, X. Zhang, and L. Dong, Phys. Plasmas **17**, 113501 (2010).
[52] L. Dong, J. Shang, Y. He, Z. Bai, L. Liu, and W. Fan, Phys. Rev. E **85**, 066403 (2012).
[53] H. HOJO, N. UCHIDA, K. HATTORI, and A. MASE, Plasma Fusion Res. **1**, 021 (2006).
[54] E.H. Matlis, T.C. Corke, B. Neiswander, and A.J. Hoffman, J. Appl. Phys. **124**, 093104 (2018).
[55] H.J. Yang, S.-J.J. Park, and J.G. Eden, J. Phys. D. Appl. Phys. **50**, 43LT05 (2017).
[56] J. Faith, S.P. Kuo, J. Huang, J. Faith, S.P. Kuo, and J. Huang, Phys. Rev. E - Stat. Physics, Plasmas, Fluids, Relat. Interdiscip. Top. **55**, 1843 (1997).
[57] P.P. Sun, R. Zhang, W. Chen, P. V. Braun, and J. Gary Eden, Appl. Phys. Rev. **6**, 041406 (2019).
[58] B. Wang, J.A. Rodriguez, and M.A. Cappelli, Plasma Sources Sci. Technol. **28**, 02LT01 (2019).
[59] V. Kuzmiak and A.A. Maradudin, Phys. Rev. B **55**, 7427 (1997).
[60] H.F. Zhang, G.W. Ding, H.M. Li, and S. Bin Liu, Phys. Plasmas **22**, 022105 (2015).
[61] F. Righetti, B. Wang, and M.A. Cappelli, Phys. Plasmas **25**, (2018).
[62] H.F. Zhang, S. Bin Liu, and B.X. Li, Phys. Plasmas **23**, 012105 (2016).
[63] H.F. Zhang, G.W. Ding, H.M. Li, and S. Bin Liu, Phys. Plasmas **22**, 022105 (2015).
[64] H.F. Zhang, S. Bin Liu, and Y.C. Jiang, Phys. Plasmas **21**, 092104 (2014).
[65] J. Benford and J. Swegle, *High Power Microwaves* (Artech House, Boston, 1992).
[66] E. Schamiloglu, 2004 IEEE MTT-S Int. Microw. Symp. Dig. **2**, 1001 (2004).
[67] W.M. Manheimer, A.W. Fliflet, K. St. Germain, G.J. Linde, W.J. Cheung, V. Gregers-Hansen, B.G. Danly, and M.T. Ngo, Geophys. Res. Lett. **30**, 5 (2003).
[68] J. Benford, **36**, 569 (2008).
[69] P.E. Nielsen, *Effects of Directed Energy Weapon* (Center for Technology and National Security Policy, 1994).
[70] A. Feickert, (2018).
[71] N.S. Kushwaha and M.M. Sharma, 2008 Int. Conf. Recent Adv. Microw. Theory Appl. Microw. 2008 871 (2008).
[72]Air Force Res. Lab. (n.d.).
[73] S. Losey, Def. News (2022).
[74] C. Albon, Jt. Intermed. Force Capab. Off. US DOD Non-Lethal Weapons Progr. (n.d.).
[75]Boeing Co. (2011).
[76] J. McGonegal, *HIGH POWER MICROWAVE WEAPONS: DISRUPTIVE TECHNOLOGY FOR THE FUTURE* (Maxwell Air Force Base, AL, 2020).
[77] C.H. Liu, J.D. Neher, J.H. Booske, and N. Behdad, J. Appl. Phys. **116**, 143302 (2014).
[78] R. Seviour, Y.S. Tan, and A. Hopper, 2014 8th Int. Congr. Adv. Electromagn. Mater. Microwaves Opt.

METAMATERIALS 2014 142 (2014).
[79] C.H. Liu, J.D. Neher, J.H. Booske, and N. Behdad, IEEE Trans. Plasma Sci. **42**, 1255 (2014).
[80] S.H. Gold and G.S. Nusinovich, Rev. Sci. Instrum. **68**, 3945 (1997).
[81] D. Shiffler, J. Luginsland, D.M. French, and J. Watrous, IEEE Trans. Plasma Sci. **38**, 1462 (2010).
[82] T. Fu, Z.Q. Yang, and Z.B. Ouyang, J. Infrared, Millimeter, Terahertz Waves **37**, 1061 (2016).
[83] J. Zhang, B.J. Munroe, H. Xu, M.A. Shapiro, and R.J. Temkin, Phys. Rev. Accel. Beams **19**, 1 (2016).
[84] J.H. Booske, Phys. Plasmas **15**, (2008).
[85] J.S. Hummelt, High Power Microwave Generation Using an Active Metamaterial Powered by an Electron Beam, Massachusetts Institute of Technology, 2016.
[86] D.M. French, D. Shiffler, and K. Cartwright, Phys. Plasmas **20**, 083116 (2013).
[87] M.C. Paliwoda and J.L. Rovey, Phys. Plasmas **27**, 023516 (2020).
[88] T. Sakaguchi, O. Sakai, and K. Tachibana, J. Appl. Phys. **101**, 073305 (2007).
[89] L.-M. Qi and Z. Yang, Prog. Electromagn. Res. **91**, 319 (2009).
[90] H.F. Zhang, S. Liu, and X.-K. Kong, Prog. Electromagn. Res. **141**, 267 (2013).
[91] H. Zhang, S. Liu, and X. Kong, J. Electromagn. Waves Appl. **27**, 1776 (2013).
[92] H.-F. Zhang, S.-B. Liu, and X.-K. Kong, J. Electromagn. Waves Appl. **27**, 1276 (2013).
[93] H.-F. Zhang, S.-B. Liu, and Y.-C. Jiang, Phys. Plasmas **21**, 092104 (2014).
[94] H.-F.F. Zhang, S.-B. Bin Liu, X.-K.K. Kong, Chen-Chen, and B.-R.R. Bian, Opt. Commun. **288**, 82 (2013).
[95] H.-F. Zhang, S.-B. Liu, and B.-X. Li, Phys. Plasmas **23**, 012105 (2016).
[96] N.S.J. Braithwaite, Plasma Sources Sci. Technol. **9**, 517 (2000).
[97] X. Lu, S. Wu, J. Gou, and Y. Pan, Sci. Rep. **4**, (2014).
[98] G.G. Raju, *Gaseous Electronics : Theory and Practice* (Taylor & Francis, Boca Raton :, 2006).
[99] P. Bruggeman and R. Brandenburg, J. Phys. D. Appl. Phys. **46**, 464001 (2013).
[100] M.C. Paliwoda and J.L. Rovey, Phys. Plasmas **24**, 053504 (2017).
[101] M.C. Paliwoda and J.L. Rovey, Phys. Plasmas **24**, 053505 (2017).
[102] R. Maspero, S.J. Sweeney, and M. Florescu, J. Phys. Condens. Matter **29**, (2017).
[103] S. Keller, P. Rajasekaran, N. Bibinov, and P. Awakowicz, J. Phys. D. Appl. Phys. **45**, (2012).
[104] H.-F.F. Zhang, S.-B. Bin Liu, and Y.-C.C. Jiang, Phys. Plasmas **21**, 092104 (2014).
[105] A. Alù, A. Salandrino, and N. Engheta, Opt. Express **14**, 1557 (2006).
[106] J.B. Pendry, A.J. Holden, D.J. Robbins, and W.J. Stewart, IEEE Trans. Microw. Theory Tech. **47**, 2075 (1999).
[107] L.B. Loeb and J.M. Meek, J. Appl. Phys. **11**, 459 (1940).
[108] J.M. Meek and J.D. Craggs, *Electrical Breakdown of Gases* (Clarendon Press, Oxford, 1953).
[109] O. Emelyanov and M. Shemet, J. Electrostat. **81**, 71 (2016).
[110] O.A. Emelyanov and M. V. Shemet, J. Phys. D. Appl. Phys. **47**, 315201 (2014).
[111] S. Ma, J. Howard, and N. Thapar, Phys. Plasmas **18**, 083301 (2011).
[112] X. Wang, H. Luo, Z. Liang, T. Mao, and R. Ma, Plasma Sources Sci. Technol. **15**, 845 (2006).
[113] Q. Ye, Y. Wu, X. Li, T. Chen, and G. Shao, Plasma Sources Sci. Technol. **21**, 065008 (2012).
[114] B. Eliasson and U. Kogelschatz, IEEE Trans. Plasma Sci. **19**, 1063 (1991).
[115] R. Morrow and J.J. Lowke, J. Phys. D. Appl. Phys. **30**, 614 (1997).
[116] A.J. Davies, C.S. Davies, and C.J. Evans, Proc. Inst. Electr. Eng. **118**, 816 (1971).
[117] R. Morrow, Phys. Rev. A **32**, 1799 (1985).
[118] M.C. Paliwoda, J.L. Rovey, and M. Wainwright, in *54th AIAA Aerosp. Sci. Meet. AIAA SciTech Forum* (AIAA 2016-0197, San Diego, CA, 2016), p. AIAA 2016-0197.
[119] CST of America, (2015).
[120] H.A. Haus and J.R. Melcher, *Electromagnetic Fields and Energy* (Prentice Hall, Englewood Cliffs, NJ, 1989).
[121] D.L. Logan, *A First Course in the Finite Element Method*, 5th ed. (Cengage Learning, Stamford, CT, 2012).

[122] M. Kettlitz, H. Höft, T. Hoder, S. Reuter, K.-D.D. Weltmann, and R. Brandenburg, J. Phys. D. Appl. Phys. **45**, 245201 (2012).
[123] J.D. Jackson, *Classical Electrodynamics* (Wiley, New York, NY, 1999).
[124] L. Warne, R. Jorgenson, and S. Nicolaysen, *Ionization Coefficient Approach to Modeling Breakdown in Nonuniform Geometries* (Albuquerque, NM, 2003).
[125] V.S. Smentkowski and C.A. Moore, J. Vac. Sci. Technol. A Vacuum, Surfaces, Film. **31**, 06F105 (2013).
[126] Corning Inc., *Macor, Machinable Ceramic Glass* (2009).
[127] USGS, *Organic Compounds Assessed in Chattahoochee River Water Used for Public Supply near Atlanta, Georgia, 2004 – 05* (2011).
[128] M.J. Benotti, R.A. Trenholm, B.J. Vanderford, J.C. Holady, B.D. Stanford, and S.A. Snyder, Environ. Sci. Technol. **43**, 597 (2009).
[129] J. Flaws, P. Damdimopoulou, H.B. Patisaul, A. Gore, and L. Raetzman, *PLASTICS, EDCs & HEALTH A GUIDE FOR PUBLIC INTEREST ORGANIZATIONS AND POLICY-MAKERS ON ENDOCRINE DISRUPTING CHEMICALS & PLASTICS* (2020).
[130] A. Gonsioroski, V.E. Mourikes, and J.A. Flaws, Int. J. Mol. Sci. **21**, (2020).
[131] N. Takeuchi and K. Yasuoka, Jpn. J. Appl. Phys. **60**, (2021).
[132] US EPA, United States Environ. Prot. Agnecy 1 (1999).
[133] C. Wei, F. Zhang, Y. Hu, C. Feng, and H. Wu, Rev. Chem. Eng. **33**, 49 (2017).
[134] J.D. McClurkin, D.E. Maier, and K.E. Ileleji, J. Stored Prod. Res. **55**, 41 (2013).
[135] B.L. Loeb, C.M. Thompson, J. Drago, H. Takahara, and S. Baig, Ozone Sci. Eng. **34**, 64 (2012).
[136] A.J. Roy, J. / Am. Water Work. Assoc. **102**, 44 (2010).
[137] B. Mundy, B. Kuhnel, G. Hunter, R. Jarnis, D. Funk, S. Walker, N. Burns, J. Drago, W. Nezgod, J. Huang, K. Rakness, S. Jasim, R. Joost, R. Kim, J. Muri, J. Nattress, M. Oneby, A. Sosebee, C. Thompson, M. Walsh, and C. Schulz, Ozone Sci. Eng. **40**, 266 (2018).
[138] P.J. Bruggeman, M.J. Kushner, B.R. Locke, J.G.E. Gardeniers, W.G. Graham, D.B. Graves, R.C.H.M. Hofman-Caris, D. Maric, J.P. Reid, E. Ceriani, D. Fernandez Rivas, J.E. Foster, S.C. Garrick, Y. Gorbanev, S. Hamaguchi, F. Iza, H. Jablonowski, E. Klimova, J. Kolb, F. Krcma, P. Lukes, Z. MacHala, I. Marinov, D. Mariotti, S. Mededovic Thagard, D. Minakata, E.C. Neyts, J. Pawlat, Z.L. Petrovic, R. Pflieger, S. Reuter, D.C. Schram, S. Schröter, M. Shiraiwa, B. Tarabová, P.A. Tsai, J.R.R. Verlet, T. Von Woedtke, K.R. Wilson, K. Yasui, and G. Zvereva, Plasma Sources Sci. Technol. **25**, (2016).
[139] N. Parkansky, A. Vegerhof, B.A. Alterkop, O. Berkh, and R.L. Boxman, Plasma Chem. Plasma Process. **32**, 933 (2012).
[140] N. Parkansky, E.F. Simon, B.A. Alterkop, R.L. Boxman, and O. Berkh, Plasma Chem. Plasma Process. **33**, 907 (2013).
[141] L.O. Luís, B.M. Cadorin, C. Da S. Postiglione, I.G. De Souzaa, and N.A. Debacher, J. Braz. Chem. Soc. **22**, 1669 (2011).
[142] H. Lee, G. Yang, Y. Shin, K. Kim, and Y.C. Hong, IEEE Trans. Plasma Sci. **49**, 3268 (2021).
[143] L. Wu, Q. Xie, Y. Lv, Z. Zhang, Z. Wu, X. Liang, M. Lu, and Y. Nie, RSC Adv. **9**, 25967 (2019).
[144] B. Wang, B. Dong, M. Xu, C. Chi, and C. Wang, Chem. Eng. Sci. **168**, 90 (2017).
[145] M. Magureanu, D. Piroi, N.B. Mandache, and V. Parvulescu, J. Appl. Phys. **104**, (2008).
[146] L. Wu, Q. Xie, Y. Lv, Z. Wu, X. Liang, M. Lu, and Y. Nie, Water (Switzerland) **11**, (2019).
[147] P. Manoj Kumar Reddy, B. Rama Raju, J. Karuppiah, E. Linga Reddy, and C. Subrahmanyam, Chem. Eng. J. **217**, 41 (2013).
[148] F. Huang, L. Chen, H. Wang, and Z. Yan, Chem. Eng. J. **162**, 250 (2010).
[149] M. Magureanu, C. Bradu, D. Piroi, N.B. Mandache, and V. Parvulescu, Plasma Chem. Plasma Process. **33**, 51 (2013).
[150] Y. Jin, Y. Wu, J. Cao, and Y. Wu, J. Taiwan Inst. Chem. Eng. **45**, 589 (2014).
[151] Y.Y. Zhao, T. Wang, S.J. MacGregor, M.P. Wilson, M.J. Given, and I. V Timoshkin, Proc. 20th Int. Conf. Gas Discharges Their Appl. **3**, 566 (2014).

[152] M. Yamada, Wahyudiono, S. Machmudah, H. Kanda, and M. Goto, Plasma Chem. Plasma Process. **40**, 985 (2020).
[153] A. Krosuri, S. Wu, M.A. Bashir, and M. Walquist, J. Water Process Eng. **40**, 101926 (2021).
[154] T. Shirafuji and Y. Himeno, Jpn. J. Appl. Phys. **52**, (2013).
[155] J.E. Foster, G. Adamovsky, S.N. Gucker, and I.M. Blankson, IEEE Trans. Plasma Sci. **41**, 503 (2013).
[156] M.C. García, M. Mora, D. Esquivel, J.E. Foster, A. Rodero, C. Jiménez-Sanchidrián, and F.J. Romero-Salguero, Chemosphere **180**, 239 (2017).
[157] T. Ishijima, H. Sugiura, R. Saito, H. Toyoda, and H. Sugai, Plasma Sources Sci. Technol. **19**, 1 (2010).
[158] G. Muthuraman, T.T. Teng, C.P. Leh, and I. Norli, J. Hazard. Mater. **163**, 363 (2009).
[159] A. Fernandez-Perez and G. Marban, ACS Omega **5**, 29801 (2020).
[160] I. Glassman and R.A. Yetter, 773 (2008).
[161]Suez Water Technol. Solut. (n.d.).
[162] B.W.K. Lewis and W.G. Whitman, Ind. Eng. Chem. **16**, 1215 (1924).
[163] M. Roustan, R.Y. Wang, and D. Wolbert, Ozone Sci. Eng. **18**, 99 (1996).
[164] N.P. Cheremisinoff and R. Gupta, *Handbook of Fluids in Motion* (Ann Arbor Science, Ann Arbor Mich., 1983).
[165] D.W. Ball, F. Guid. to Spectrosc. (2006).
[166] S. Prahl, Oragon Med. Laser Cent. (1998).
[167] R. Massarczyk, P. Chu, C. Dugger, S.R. Elliott, K. Rielage, and W. Xu, JINST **12**, 06019 (2017).
[168] J.D. McClurkin and D.E. Maier, Julius-Kühn-Archiv 381 (2010).
[169] B.-K. Feng, EXTRACTING MATERIAL CONSTITUTIVE PARAMETERS FROM SCATTERING PARAMETERS, NAVAL POSTGRADUATE SCHOOL, MONTEREY, CALIFORNIA, 2006.

Appendix A: Derivation of Plasma Permittivity

The charge particle motion is described by the Lorentz Force, Eq. 36. This includes damping effects from the collision frequency (ν_c). This is considered for a plasma free of a magnetic field.

$$m_e \frac{\partial \mathrm{v}}{\partial t} = qE - \mathrm{v}m_e\nu_c + q\mathrm{v} \times B \quad \text{Eq. 36}$$

The cross product of the velocity (v) with the magnetic field strength (B) from an incident wave is far less than the force from the same incident wave's electric field (E), giving the following relationship: E >> v x B. In addition, the incident wave is assumed to be harmonic, so a Fourier transform is applied to the time derivative ($\frac{\partial}{\partial t} \rightarrow i\omega$).

$$i\omega m_e \mathrm{v} = qE - \mathrm{v}m_e\nu_c \quad \text{Eq. 37}$$

The equation is rearranged for the velocity.

$$im_e \mathrm{v}(\omega - j\nu_c) = qE \quad \text{Eq. 38}$$

Both the top and bottom of the term on the right are multiplied by *i*.

$$\mathrm{v} = \frac{-iqE}{m_e(\omega - i\nu_c)} \quad \text{Eq. 39}$$

The current density (J) is expressed as a function of the charge (q), electron density (n_e), and the velocity (v).

$$J = qn_e\mathrm{v} \quad \text{Eq. 40}$$

Substituting Eq. 39 into Eq. 40, the current is expressed in terms of the plasma physical properties and the electric field.

$$J = qn_e \frac{-iqE}{m_e(\omega - i\nu_c)} \quad \text{Eq. 41}$$

Wave interactions are described by Ampere's Law, with both a conductive (J) and displacement current ($\varepsilon_o \frac{\partial E}{\partial t}$).

$$\nabla \times B = \mu_o J + \mu_o \varepsilon_o \frac{\partial E}{\partial t} \quad \text{Eq. 42}$$

The time derivative is linearized using the Fourier transform of (-iω).

$$\nabla \times B = \mu_o J + i\omega\mu_o\varepsilon_o E \quad \text{Eq. 43}$$

When the conduction current is replaced by a factoring term of the displacement current, the term is defined as the relative permittivity (ε_r).

$$\nabla \times B = i\omega\varepsilon_r\varepsilon_o\mu_o E \quad \text{Eq. 44}$$

To define this term for the plasma, Eq. 41 is substituted into Eq. 42 to replace the displacement current.

$$\nabla \times B = \mu_o\, qn_e \frac{-iqE}{m_e\omega - i\nu_c} + i\omega\mu_o\varepsilon_o E \quad \text{Eq. 45}$$

The left term on the right side is multiplied on the top and bottom by the frequency (ω).

$$\nabla \times B = \mu_o\, qn_e \frac{-i\omega qE}{\omega(m_e\omega - i\nu_c)} + i\omega\mu_o\varepsilon_o E \quad \text{Eq. 46}$$

The electric field and common coefficients between the two terms on the right side are factored out

$$\nabla \times B = i\omega\varepsilon_o\mu_o E\left(1 - \frac{q^2 n_e}{m_e\varepsilon_o\omega(\omega - i\nu_c)}\right) \quad \text{Eq. 47}$$

The relative permittivity is then defined by:

$$\varepsilon_r = \left(1 - \frac{\frac{q^2 n_e}{m_e\varepsilon_o}}{\omega(\omega - i\nu_c)}\right) \quad \text{Eq. 48}$$

The plasma constants in the numerator are treated as the square of a frequency term defined as the plasma frequency, since they form a non-dimensional ratio with the two frequency terms in the denominator.

$$\omega_p = \frac{q^2 n_e}{m_e\varepsilon_o} \quad \text{Eq. 49}$$

$$\varepsilon_r = \left(1 - \frac{\omega_p^2}{\omega(\omega - i\nu_c)}\right) \quad \text{Eq. 50}$$

Appendix B: Plane Wave Expansion Method (PWE)

The governing equation is the Maxwellian Helmholtz wave equation in frequency space, Eq. 51. The effective dielectric ($\boldsymbol{\varepsilon_{eff}}$) either represents a plasma dielectric or the background dielectric. The plasma dielectric is dependent upon the propagating angular frequency ($\boldsymbol{\omega}$) as described by Eq. 52. Since there is an inhomogeneous dielectric distribution, the effective dielectric is also dependent upon the position vector ($\boldsymbol{x}$). The electric field (E) is dependent upon the incident frequency and the dielectric distribution as it must adapt to satisfy Eq. 51.

$$\nabla \times \big(\nabla \times E(\boldsymbol{x},\omega)\big) = \left(\frac{\omega}{c}\right)^2 \varepsilon_{eff}(\boldsymbol{x},\omega) E(\boldsymbol{x},\omega) \qquad \text{Eq. 51}$$

$$\varepsilon_{eff}(\omega) = 1 - \frac{\omega_{pe}^2}{\omega(\omega + j\nu_c)} \qquad \text{Eq. 52}$$

To simplify the equation and perform the double curl, Bloch's theorem is applied which states that the solution to a wave equation in a periodic structure, expressed as a periodic function Eq. 53, can be expressed as the summation of periodic plane waves, Eq. 54. These equations are Fourier series with respect to the Fourier space reciprocal lattice vector ($\boldsymbol{G}$). These functions are used in the same way as a Fourier series summation of angular frequencies to represent a periodic function of time. As the space analog to angular frequency ($\omega = 2\pi/T$), the reciprocal lattice vector is inversely proportional to space ($G = 2\pi/a$), where (a) is the lattice constant – the spatial periodicity – the same way the period (T) is the temporal periodicity. The expression also includes the wavevector ($\boldsymbol{k} = 2\pi/\lambda\, \hat{\boldsymbol{k}}$) that defines the direction and wavelength (λ). The product of the angular frequency and time that would normally have shown up in the exponent of Eq. 54, is dropped as it would cancel in Eq. 51. Similarly, the Fourier series expression of the periodic dielectric, Eq. 53, contains ($\boldsymbol{G'}$) which is the same set of values as ($\boldsymbol{G}$). The other terms are the Fourier series constant (A) and the reciprocal dielectric constant ($\hat{\varepsilon}$).

$$\varepsilon(\boldsymbol{x}) = \sum_{G'} \hat{\varepsilon}(\boldsymbol{G'}) e^{i(\boldsymbol{G'})*\boldsymbol{x}} \qquad \text{Eq. 53}$$

$$\boldsymbol{E}(\boldsymbol{x},\omega) = \sum_{G} A(\boldsymbol{k},\boldsymbol{G}) e^{i(\boldsymbol{k}+\boldsymbol{G})*\boldsymbol{x}} \quad \text{Eq. 54}$$

The reciprocal dielectric constant is related to the real space distribution of the dielectric by an inverse Fourier transform Eq. 55.

$$\hat{\varepsilon}(\boldsymbol{G}) = \frac{1}{S}\iint_{S} \varepsilon(\boldsymbol{x})\, \mathrm{e}^{-\mathrm{i}\mathbf{G}\cdot\mathbf{x}} dS \quad \text{Eq. 55}$$

As multiple vectors are needed in the Fourier series to make the approximation of Eq. 54 and Eq. 53, different harmonics of the previously defined reciprocal vector are used, ($G = n2\pi/a,\ n = \pm 0, 1, 2, \ldots$). Harmonics based on the lattice constant are used since this agrees with the Bloch Theorem and makes the resulting equation solvable. For computational purposes there is a maximum number of reciprocal vectors that increase the accuracy of the simulation with higher (n) values. For these simulations, $n = 3$. The last consideration in defining the reciprocal lattice vector is its direction. For a 2D square lattice structure, where the unit cell is a square, there is a x and y component of the reciprocal vector ($[G_x = n2\pi/a,\ G_y = m2\pi/a\ ],\ n = \pm 0, 1, 2, \ldots,\ m = \pm 0, 1, 2, \ldots$). Substituting Eq. 54 and Eq. 53 into Eq. 51 produces Eq. 56

$$(\boldsymbol{k}+\boldsymbol{G})^2 \sum_{G_l} A(\boldsymbol{k},\boldsymbol{G_l}) e^{i(\boldsymbol{k}+\boldsymbol{G_l})*\boldsymbol{x}} = \left(\frac{\omega}{c}\right)^2 \sum_{G_n} \hat{\varepsilon}(\boldsymbol{G_n}) e^{i(\boldsymbol{G_n})*\boldsymbol{x}} \sum_{G_m} A(\boldsymbol{k},\boldsymbol{G_m}) e^{i(\boldsymbol{k}+\boldsymbol{G_m})*\boldsymbol{x}} \quad \text{Eq. 56}$$

After rearranging terms with series multiplication and some simplification, Eq. 56 is expressed in matrix form, Eq. 57. Each row represents a of summation of (G_m) and each column represents a change in (G_l). These reciprocal vectors (G_m) and (G_l) are the same set of values. By substituting the expression $G_n = G_l - G_m$ into Eq. 56, the exponentials on the right were simplified and equal the exponential terms on the left. The same set of (G_m) and (G_l) values also allows the Fourier series constants (A) to be equal.

$$[\mathbf{1}]_{l\times\boldsymbol{m}}[\,\boldsymbol{k}+\boldsymbol{G_l}]_{l\times 1}\left[e^{i(\boldsymbol{k}+\boldsymbol{G_l})\cdot\boldsymbol{x}} A(\boldsymbol{k},\boldsymbol{G_l})\right]_{l\times 1} = \left(\frac{\omega}{c}\right)^2 [\hat{\boldsymbol{\varepsilon}}(\boldsymbol{G}_l - \boldsymbol{G}_m)]_{l\times\boldsymbol{m}}\left[e^{i(\boldsymbol{k}+\boldsymbol{G_l})\cdot\boldsymbol{x}} A(\boldsymbol{k},\boldsymbol{G_l})\right]_{l\times 1} \quad \text{Eq. 57}$$

If the dielectric distribution was independent of frequency, then Eq. 55 would be substituted into Eq. 57, and rearranged to produce a standard eigenvalue problem, Eq. 58, with the simplified form Eq. 59. The normalized frequency $(\omega/c)^2$ would be the eigenvalue and the set of periodic functions $e^{i(\boldsymbol{k}+\boldsymbol{G_l})\cdot\boldsymbol{x}}A(\boldsymbol{k},\boldsymbol{G_l})$ would be the eigenvectors. The sum of the eigenvectors then produces the electric field, as defined in Eq. 54.

$$[\hat{\boldsymbol{\varepsilon}}(\boldsymbol{G}_l-\boldsymbol{G}_m)]^{-1}_{l\times\boldsymbol{m}}[\,\boldsymbol{k}+\boldsymbol{G_l}]_{l\times 1}\left[e^{i(\boldsymbol{k}+\boldsymbol{G_l})\cdot\boldsymbol{x}}A(\boldsymbol{k},\boldsymbol{G_l})\right]_{l\times 1}=\left(\frac{\omega}{c}\right)^2\left[e^{i(\boldsymbol{k}+\boldsymbol{G_l})\cdot\boldsymbol{x}}A(\boldsymbol{k},\boldsymbol{G_l})\right]_{l\times 1} \quad \text{Eq. 58}$$

$$\mathbf{A}\boldsymbol{x}=\lambda\boldsymbol{x} \quad \text{Eq. 59}$$

It should be noted that the different periodic functions $e^{i(\boldsymbol{k}+\boldsymbol{G_l})\cdot\boldsymbol{x}}A(\boldsymbol{k},\boldsymbol{G_l})$, dependent upon the reciprocal vector (G_l), are orthogonal to one-another. One periodic function of a specific reciprocal vector value cannot be reproduced as a linear sum of the remaining reciprocal vectors with constant coefficients (c_l), as demonstrated in Eq. 60.

$$e^{i(\boldsymbol{k}+\boldsymbol{G_0})\cdot\boldsymbol{x}}\neq c_1e^{i(\boldsymbol{k}+\boldsymbol{G_1})\cdot\boldsymbol{x}}+c_2e^{i(\boldsymbol{k}+\boldsymbol{G_2})\cdot\boldsymbol{x}}+c_3e^{i(\boldsymbol{k}+\boldsymbol{G_3})\cdot\boldsymbol{x}}+\cdots \quad \text{Eq. 60}$$

This means that to satisfy Eq. 57, each row in the left matrix must equal each row in the right matrix. With this understanding, Eq. 57 is further simplified to Eq. 61.

$$[\mathbf{1}]_{l\times l}[\,\boldsymbol{k}+\boldsymbol{G_l}]_{l\times\mathbf{1}}-\left(\frac{\omega}{c}\right)^2[\hat{\boldsymbol{\varepsilon}}(\boldsymbol{G}_l-\boldsymbol{G}_m)]_{l\times\boldsymbol{m}}=[\mathbf{0}] \quad \text{Eq. 61}$$

Since this method is to be used with a plasma dielectric that is dependent upon the incident frequency (ω) Eq. 52, the frequency within $\hat{\boldsymbol{\varepsilon}}$ must be extracted. Multiplying Eq. 52 by the denominator $\omega(\omega^2+j\nu_c^2)$ and redistributing, produces an expanded polynomial as a function of (ω/c) for each matrix row, Eq. 62.

$$0=\left(\frac{\omega}{c}\right)^3\theta(G_l-G_m)-\left(\frac{\omega}{c}\right)^2\frac{i\nu_c}{c}\theta(G_l-G_m)-\left(\frac{\omega}{c}\right)\left(\frac{\eta(G_l-G_m)}{c^2}+\delta_{lm}(\boldsymbol{k}+\boldsymbol{G_l})^2\right)+\frac{i\nu_c}{c}\delta_{lm}(\boldsymbol{k}+\boldsymbol{G_l})^2 \quad \text{Eq. 62}$$

Each coefficient of the polynomial can be expressed as a matrix to combine the different (G_m) and (G_l) combinations, Eq. 63, where $\lambda=\frac{\omega}{c}$.

$$-\lambda^3 \boldsymbol{X}_3 + \lambda^2 \boldsymbol{X}_2 + \lambda \boldsymbol{X}_1 + \boldsymbol{X}_0 = \mathbf{0} \quad \text{Eq. 63}$$

The polynomial is then expressed as the determinate, Eq. 64, of two block matrices Eq. 65.

$$\det(\mathbf{Q} - \lambda \mathbf{V}) = 0 \quad \text{Eq. 64}$$

$$\mathbf{V} = \begin{bmatrix} \boldsymbol{I} & 0 & 0 \\ 0 & \boldsymbol{I} & 0 \\ 0 & 0 & \boldsymbol{X}_3 \end{bmatrix} \qquad \mathbf{Q} = \begin{bmatrix} 0 & \boldsymbol{I} & 0 \\ 0 & 0 & \boldsymbol{I} \\ \boldsymbol{X}_0 & \boldsymbol{X}_1 & \boldsymbol{X}_2 \end{bmatrix} \quad \text{Eq. 65}$$

The final condensed general problem is Eq. 66, which is a more general form of the eigenvalue problem. As previously mentioned, the resulting eigenvalues and eigenvectors are equivalent to the frequency and electric field.

$$\mathbf{Q}\boldsymbol{z} - \lambda \mathbf{V}\boldsymbol{z} = 0 \quad \text{Eq. 66}$$

The process for solving is as follows: 1) Provide a 2D plasma permittivity and background dielectric distribution over the unit cell as the dielectric distribution function $\varepsilon(\boldsymbol{x})$. 2) Provide a wavevector value with a magnitude from 0 to π/a (a: length of the unit cell). 3) Solve the eigenvalue problem. 4) The resulting set of frequencies represent solutions to the problem for the specified wavevector. 5) The locus of frequencies produced by the collection of Brillouin Zone wavevectors produces a band diagram, such as the one in FIG. 4.

Appendix C: Bandgap Polynomial Coefficients

Table 5. Coefficients of polynomial fits that define the TE1 and TE0 bandgap limits. (GHz) (Invariants: x0: radius, x1: background dielectric, x2: plasma frequency, x3: collision frequency, x4: lattice constant.)

Invariants	TE0 upper	TE1 lower	TE1 upper	Invariants	TE0 upper	TE1 lower	TE1 upper
1	-9.145E+1	7.992E+2	3.250E+2	x_1^3	-1.634E+0	-2.588E+0	-2.897E+0
x_0	4.491E+3	1.399E+2	3.323E+3	$x_1^2 x_2$	5.825E-1	1.440E-1	1.286E+0
x_1	-1.006E+2	-1.927E+2	-1.696E+2	$x_1^2 x_3$	3.047E-1	-5.081E-2	-3.116E-1
x_2	3.500E+2	1.325E+1	2.006E+2	$x_1^2 x_4$	-8.368E+0	-9.541E+0	-1.277E+1
x_3	-5.619E+2	7.277E+0	-5.995E+1	$x_1 x_2^2$	-3.668E+0	1.685E-1	9.518E-1
x_4	-5.138E+2	-9.341E+2	-9.516E+2	$x_1 x_2 x_3$	1.550E+1	4.445E-1	7.537E-1
x_0^2	-1.631E+4	5.741E+2	-6.927E+3	$x_1 x_2 x_4$	1.542E+1	4.489E+0	1.624E+1
$x_0 x_1$	6.353E+1	-8.931E+0	-1.083E+2	$x_1 x_3^2$	-4.664E+0	-2.235E-1	1.424E-1
$x_0 x_2$	-1.020E+3	7.812E+1	-3.576E+2	$x_1 x_3 x_4$	-1.042E+1	-3.176E+0	-7.283E+0
$x_0 x_3$	2.873E+3	-1.079E+2	1.634E+2	$x_1 x_4^2$	-4.076E+1	-4.532E+1	-6.765E+1
$x_0 x_4$	-1.446E+3	-6.138E+2	-1.637E+3	x_2^3	2.118E+1	-3.032E-1	7.690E-1
x_1^2	1.752E+1	3.171E+1	3.174E+1	$x_2^2 x_3$	-6.222E+1	7.937E-2	-1.689E+0
$x_1 x_2$	8.023E+0	-3.576E+0	-1.498E+1	$x_2^2 x_4$	-1.621E+0	-4.614E-1	-8.910E-1
$x_1 x_3$	-5.400E+1	7.794E-1	-1.976E+0	$x_2 x_3^2$	2.943E+1	1.156E-1	9.619E-1
$x_1 x_4$	5.434E+1	1.156E+2	1.211E+2	x2 x3 x4	2.621E+1	3.758E+0	9.495E+0
x_2^2	-1.242E+2	2.581E-1	-2.438E+1	$x_2 x_4^2$	5.628E+1	2.866E+1	1.112E+2
$x_2 x_3$	3.160E+2	-4.794E+0	1.733E+1	x_3^3	-2.285E+0	-2.794E-2	1.907E-1
$x_2 x_4$	-5.842E+1	-2.566E+1	-1.073E+2	$x_3^2 x_4$	-6.936E+0	-3.837E+0	-1.830E+0
x_3^2	-9.601E+1	1.096E+0	-5.183E+0	$x_3 x_4^2$	-1.634E+1	-1.783E+1	-5.789E+1
$x_3 x_4$	-9.414E+1	1.488E+1	2.521E+1	x_4^3	-2.877E+2	-2.727E+2	-4.880E+2
x_4^2	5.214E+2	6.359E+2	8.125E+2	x_0^4	-3.179E+4	1.850E+3	-1.630E+3
x_0^3	4.179E+4	3.268E+3	1.874E+4	$x_0^3 x_1$	5.568E+2	-1.932E+2	-1.576E+2
$x_0^2 x_1$	-8.513E+2	-1.491E+2	-3.735E+2	$x_0^3 x_2$	-2.617E+3	4.263E+2	-4.270E+2
$x_0^2 x_2$	3.336E+3	1.641E+2	2.044E+3	$x_0^3 x_3$	4.889E+3	6.053E+1	6.462E+2
$x_0^2 x_3$	-6.513E+3	-1.294E+2	-1.011E+3	$x_0^3 x_4$	8.762E+1	-4.463E+3	-9.138E+3
$x_0^2 x_4$	-4.425E+3	-2.343E+3	-6.512E+3	$x_0^2 x_1^2$	8.583E+0	1.419E+1	1.579E+1
$x_0 x_1^2$	1.836E+1	8.520E-1	1.896E+1	$x_0^2 x_1 x_2$	7.756E+1	-1.651E+1	1.854E+0
$x_0 x_1 x_2$	-1.003E+2	-8.996E+0	-5.056E+1	$x_0^2 x_1 x_3$	-1.577E+2	-7.032E+0	-4.277E+1
$x_0 x_1 x_3$	1.754E+2	7.606E+0	3.663E+1	$x_0^2 x_1 x_4$	9.179E+0	1.787E+2	2.502E+2
$x_0 x_1 x_4$	2.527E+2	7.930E+1	2.460E+2	$x_0^2 x_2^2$	-2.346E+2	3.433E+0	-1.334E+2
$x_0 x_2^2$	2.281E+2	-1.602E-2	7.759E+1	$x_0^2 x_2 x_3$	6.717E+2	-2.119E+1	1.592E+2
$x_0 x_2 x_3$	-7.786E+2	8.672E+0	-9.652E+1	$x_0^2 x_2 x_4$	1.669E+2	-3.096E+2	-3.426E+2
x0 x2 x4	-4.852E+2	-1.550E+2	-6.438E+2	x02 x32	-2.102E+2	5.327E+0	-2.900E+1

Table 5. Continued

Invariants	TE0 upper	TE1 lower	TE1 upper	Invariants	TE0 upper	TE1 lower	TE1 upper
x0 x32	2.425E+2	9.713E+0	1.589E+1	x02 x3 x4	-2.595E+2	5.758E+1	-1.724E+2
x0 x3 x4	5.088E+2	1.192E+2	3.900E+2	x02 x42	1.001E+3	2.226E+3	4.913E+3
x0 x42	1.653E+3	8.885E+2	2.577E+3	x0 x13	-7.722E-1	-3.057E-1	-1.005E+0
$x_0\,x_1^2\,x_2$	7.404E-1	7.567E-1	1.239E+0	$x_1^2\,x_3\,x_4$	-2.853E-2	3.538E-2	-3.689E-2
$x_0\,x_1^2\,x_3$	-1.360E-1	3.188E-3	4.933E-1	$x_1^2\,x_4^2$	1.598E+0	1.596E+0	2.583E+0
$x_0\,x_1^2\,x_4$	-6.914E+0	-5.264E+0	-1.070E+1	$x_1\,x_2^3$	2.861E-1	-1.187E-2	-3.339E-2
$x_0\,x_1\,x_2^2$	7.548E+0	3.208E-1	3.732E+0	$x_1\,x_2^2\,x_3$	-1.159E+0	-2.676E-2	-7.168E-2
$x_0\,x_1\,x_2\,x_3$	-2.105E+1	-1.402E+0	-7.407E+0	$x_1\,x_2^2\,x_4$	-8.752E-1	-7.240E-2	-7.230E-1
$x_0\,x_1\,x_2\,x_4$	-3.606E+0	6.845E+0	6.782E+0	$x_1\,x_2\,x_3^2$	5.570E-1	4.463E-2	5.745E-2
$x_0\,x_1\,x_3^2$	7.206E+0	7.590E-1	2.208E+0	$x_1\,x_2\,x_3\,x_4$	1.439E+0	1.563E-1	1.163E+0
$x_0\,x_1\,x_3\,x_4$	1.194E+1	1.311E+0	1.159E+1	$x_1\,x_2\,x_4^2$	-1.700E+0	-1.493E+0	-2.866E+0
$x_0\,x_1\,x_4^2$	-4.732E+1	-5.338E+1	-1.005E+2	$x_1\,x_3^3$	-5.051E-2	-1.545E-2	-2.930E-2
$x_0\,x_2^3$	-1.589E+1	-2.352E-1	-5.468E+0	$x_1\,x_3^2\,x_4$	-4.689E-1	-7.433E-2	-4.216E-1
$x_0\,x_2^2\,x_3$	5.964E+1	6.688E-1	1.095E+1	$x_1\,x_3\,x_4^2$	2.471E-1	5.162E-1	-2.216E-1
$x_0\,x_2^2\,x_4$	2.629E+1	4.318E-1	3.652E+1	$x_1\,x_4^3$	8.210E+0	9.971E+0	1.658E+1
$x_0\,x_2\,x_3^2$	-3.043E+1	-1.283E+0	-4.230E+0	x_2^4	-1.319E+0	2.694E-2	6.979E-2
$x_0\,x_2\,x_3\,x_4$	-5.363E+1	3.090E+0	-4.999E+1	$x_2^3\,x_3$	4.082E+0	1.812E-2	1.966E-2
$x_0\,x_2\,x_4^2$	6.095E+1	9.688E+1	1.732E+2	$x_2^3\,x_4$	3.315E-1	1.209E-1	4.875E-1
$x_0\,x_3^3$	2.736E+0	-5.602E-1	1.098E-1	$x_2^2\,x_3^2$	-2.285E+0	-8.875E-3	-7.346E-2
$x_0\,x_3^2\,x_4$	1.723E+1	-3.867E-1	1.341E+1	$x_2^2\,x_3\,x_4$	-1.973E+0	-3.740E-1	-1.485E+0
$x_0\,x_3\,x_4^2$	-4.542E+1	-4.589E+1	-2.681E+1	$x_2^2\,x_4^2$	-1.823E+0	-1.791E-1	-3.823E+0
$x_0\,x_4^3$	-4.161E+2	-5.039E+2	-1.222E+3	$x_2\,x_3^3$	2.314E-1	-2.531E-2	-6.264E-3
x_1^4	5.631E-2	8.389E-2	1.011E-1	$x_2\,x_3^2\,x_4$	1.010E+0	4.452E-1	7.966E-1
$x_1^3\,x_2$	-1.817E-2	-8.136E-3	-3.752E-2	$x_2\,x_3\,x_4^2$	1.411E+0	-1.226E+0	4.359E+0
$x_1^3\,x_3$	-1.138E-3	2.854E-3	1.693E-3	$x_2\,x_4^3$	-1.027E+1	-1.079E+1	-2.641E+1
$x_1^3\,x_4$	3.182E-1	3.486E-1	5.091E-1	x_3^4	2.275E-2	1.093E-2	-3.025E-3
$x_1^2\,x_2^2$	-6.565E-3	6.895E-4	-5.947E-2	$x_3^3\,x_4$	-1.918E-1	1.658E-1	-2.961E-2
$x_1^2\,x_2\,x_3$	-4.574E-2	-8.057E-3	6.345E-2	$x_3^2\,x_4^2$	-5.920E-1	-1.258E-1	-1.864E+0
$x_1^2\,x_2\,x_4$	-2.052E-1	-1.593E-1	-4.030E-1	$x_3\,x_4^3$	4.743E+0	7.708E+0	1.076E+1
$x_1^2\,x_3^2$	-3.144E-3	-4.572E-3	-3.144E-2	x_4^4	5.780E+1	6.377E+1	1.361E+2

Appendix D: SIMS Data

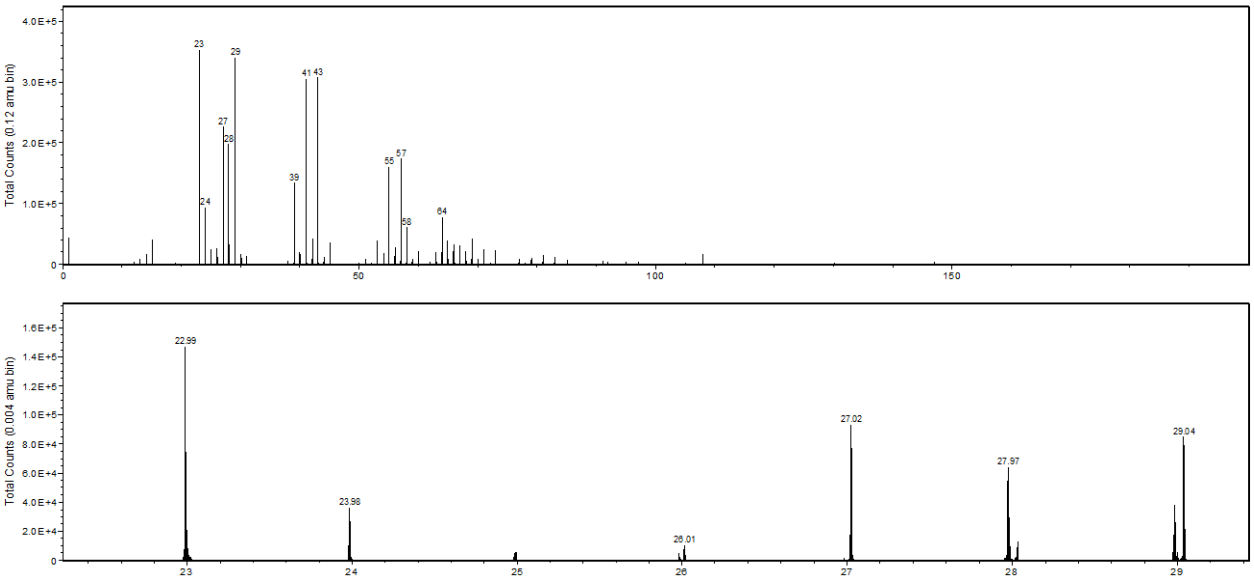

FIG. 63. SIMS results of whole image FIG. 43 (right). Total count per 0.25 amu bin.

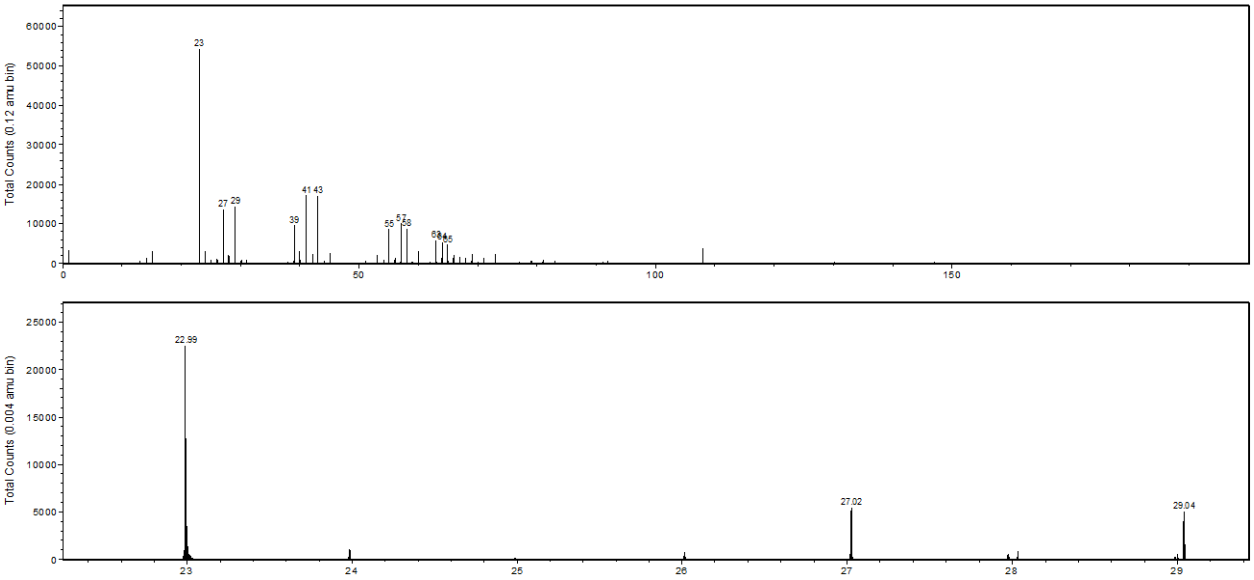

FIG. 64. SIMS results of region of interest FIG. 43 (left). Total count per 0.25 amu bin.

Appendix E: Methylene Blue Solution Preparation

The preparation procedure developed at UIUC, for the UIUC MB solution, to avoid sample error:

1) Place a small amount of MB in an aluminum weighing tray (approximately more than 5 mg).
2) Tare a SECOND aluminum weighing tray in on the Sartorius balance.
3) Use a clean metal scoop to place bits of MB into the tared weighing tray from the tray with MB.
4) Add the MB to the tared tray outside the balance so that the calibration is not disturbed.
5) Use a value of 5 ± 0.10 mg. Record this value for calculating the concentration.
6) Dispose of any unused MB. Do not replace in the container.
7) Weigh a 1000 mL beaker.
8) Using a 100 mL graduated cylinder (± 0.5 mL), measure out 100 mL of deionized water and place it in the 1000 mL beaker. (This will keep the MB grains from sticking to the bottom of the glass.)
9) Put 20 mL in to the 100 mL graduated cylinder.
10) Hold the sides of the weigh tray, tip the weigh tray over and slightly below the lip of the 1000 mL beaker to dump out the MB into the water, tap the back of the weigh tray.
11) Remove the weigh tray, bend the tray partially in half and cupping in one hand, wash the remainder of the MB out of the tray and into the 100 mL graduated cylinder with a squeeze bottle of deionized water until the deionized water does not turn blue.
12) Fill the remainder of the graduated cylinder with deionized water and pour into the 1000 mL beaker.
13) Fill and pour the 100 mL graduated cylinder into the 1000 mL beaker three more times. Each time pouring the water along the side of the beaker to remove flecks of MB from the side.
14) Re-weigh the 1000 mL beaker.
15) Use a glass stir rod to stir the solution AND break up clumps of MB by crushing them on the bottom of the beaker. (Clumps are easier to see in light and over a white background.)

16) Measure the solution by absorption to check that the solution is consistent with previous measurements and the expected absorption value.
17) Pour the solution into a glass bottle with a cap. (Evaporation of the water will change the concentration of the solution over the course of a day.)